Final Technical Report

3-D Deep Penetration Neutron Imaging of Thick Absorbing and Diffusive Objects Using Transport Theory

Prepared for the US DOE's NEER Program
(Nuclear Engineering Education Research Program)

August 1, 2011

Award Number: DE-FG07-07ID14767

Period of Performance: May 1, 2007 - April 30, 2011

Drs. Jean C. Ragusa and Wolfgang Bangerth

Departments of Nuclear Engineering and Mathematics
Texas A&M University

Contents

1 Introduction and Background

A current area of research interest in national security is to effectively and efficiently determine the contents of the many shipping containers that enter ports in the United States. This interest comes as a result of the 9/11 Commission Act passed by Congress in 2007 that requires 100% of inbound cargo to be scanned by 2012[1]. It appears that this requirement will be achieved by 2012, but as of February of 2009 eighty percent of the 11.5 million inbound cargo containers were being scanned[2]. The systems used today in all major U.S. ports to determine the presence of radioactive material within cargo containers are Radiation Portal Monitors (RPM). These devices generally exist in the form of a gate or series of gates that the containers can be driven through and scanned. The monitors are effective for determining the presence of radiation, but offer little more information about the particular source. This simple pass-fail system leads to many false alarms as many everyday items emit radiation including smoke detectors due to the Americium-241 source contained inside, bananas, milk, cocoa powder and lean beef due to the trace amounts of Potassium- 40[3], and fire brick and kitty litter due to their high clay content which often contains traces of uranium and thorium. In addition, if an illuminating source is imposed on the boundary of the container, the contents of the container may become activated. These materials include steel, aluminum and many agricultural products[3]. Current portal monitors also have not proven to be that effective at identifying natural or highly enriched uranium (HEU). In fact, the best available Advanced Spectroscopic Portal Monitors (ASP) are only capable of identifying bare HEU 70-88% of the time and masked HEU and depleted uranium (DU) only 53 percent of the time[4]. Therefore, a better algorithm that uses more information collected from better detectors about the specific material distribution within the container is desired.

The work reported here explores the inverse problem of optical tomography applied to heterogeneous domains. The neutral particle transport equation was used as the forward model for how neutral particles stream through and interact within these heterogeneous domains. A constrained optimization technique that uses Newtons method served as the basis of the inverse problem.

Optical tomography aims at reconstructing the material properties (here, the inside of the cargo) using (a) illuminating sources and (b) detector readings. However, accurate simulations for radiation transport require that the particle (gamma and/or neutron) energy be appropriate discretize in the multigroup approximation. This, in turns, yields optical tomography problems where the number of unknowns grows (1) about quadratically with respect to the number of energy groups, G, (notably to reconstruct the scattering matrix) and (2) linearly with respect to the number of unknown material regions. As pointed out in [5], a promising approach could rely on algorithms to appropriately select a material type (a single value) per material zone rather than G^2 values. This approach, though promising, still requires further investigation: (a) when switching from cross-section values unknowns (continuous real unknowns) to material type indices (discrete integer unknowns), integer programming tech-

niques are needed since derivative information is no longer available; and (b) the issue of selecting the initial material zoning remains. The work reported here proposes an approach to solve the latter item, whereby a material zoning is proposed using one-group or few-groups transport approximations.

The capabilities and limitations of the presented method were explored; they are briefly summarized next and later described in fuller details in the Appendices. The major factors that influenced the ability of the optimization method to reconstruct the cross sections of these domains included the locations of the sources used to illuminate the domains, the number of separate experiments used in the reconstruction, the locations where measurements were collected, the optical thickness of the domain, the amount of signal noise and signal bias applied to the measurements and the initial guess for the cross section distribution. All of these factors were explored for problems with and without scattering. Increasing the number of source and measurement locations and experiments generally was more successful at reconstructing optically thicker domains while producing less error in the image. The maximum optical thickness that could be reconstructed with this method was ten mean free paths for pure absorber and two mean free paths for scattering problems. Applying signal noise and signal bias to the measured fluxes produced more error in the produced image. Generally, Newtons method was more successful at reconstructing domains from an initial guess for the cross sections that was greater in magnitude than their true values than from an initial guess that was lower in magnitude.

2 PDE-constrained optimization

2.1 Misfit

The optimization problem aims at reducing the misfit between measured values and computed values. In our case, the measured values (detector readings) are measured on the boundary of the object to be analyzed. Not knowing exactly the cross-sections of that object leads to computed values that may be different that the measured ones. This misfit functional is the objective function to be minimized. It is the difference in the measured values of the outgoing angular flux solution ($\tilde{\psi}$) and values of the computed angular flux for a given set of cross sections (ψ).

We use non-invasive measurements, that is we only know the measured outgoing angular flux. The misfit represents the error between the computed outgoing angular flux and the measured ones

$$\frac{1}{2}\sum_{g\in\mathfrak{G}}\int_{\partial V^m} d^2r \int_{\vec{\Omega}\cdot\vec{n}>0} d\Omega|\vec{\Omega}\cdot\vec{n}|\left(\psi_g(\vec{r},\vec{\Omega})-\tilde{\psi}_g(\vec{r},\vec{\Omega})\right)^2 \tag{1}$$

with g the energy group index, $\mathfrak{G}$ the set of energy groups we use (we may pick a single energy group of interest, or the entire spectrum, or a subset of the spectrum), ∂V^m is the cargo boundary (∂V) where we measure ($\partial V^m \subset \partial V$),

$\vec{n}$ the outward normal unit vector, ψ_g is the computed angular flux in group g, $\tilde{\psi}_g$ is the measured angular flux in group g. In matrix notation

$$\mathbf{\Delta} = \frac{1}{2}(\mathbf{\Psi} - \tilde{\mathbf{\Psi}})^T \mathbf{M_{meas}} (\mathbf{\Psi} - \tilde{\mathbf{\Psi}}) \tag{2}$$

where M_{meas} is the measurement operator on the boundary.

2.2 Constraint

The above misfit is to be minimized provided that the compute angular flux satisfies the transport equation (the constraint).

The transport of radiation through the cargo container is governing by the linear Boltzmann equation, given below in operator notation

$$\mathcal{L}\psi = \mathcal{H}\psi + Q \text{ for } (\vec{r}, \vec{\Omega}, E) \in V \times S \times [E_{min}, E_{max}] \tag{3}$$

$$\psi = \psi^{inc} \text{ for } (\vec{r}, E) \in \partial V^- \times [E_{min}, E_{max}] \tag{4}$$

with $\psi = \psi(\vec{r}, \vec{\Omega}, E)$, $\partial V^- = \left\{ \vec{r} \in \partial V, \text{ such that } \vec{\Omega} \cdot \vec{n}(\vec{r}) < 0 \right\}$, Q is the volumetric source of particles (HEU). ψ^{inc} is the illuminating source (from a neutron of x-ray generator, for instance). After space/angle/energy discretization, this problem can be seen as (matrix notation)

$$\mathbf{A\Psi} = \mathbf{q}. \tag{5}$$

2.3 Lagrangian

The above PDE-constrained optimization problem is classically handled through a Lagrangian formulation. The Lagrangian $\mathbf{L}$ is defined as

$$\mathbf{L} = \mathbf{\Delta} + \mathbf{\Psi}^\dagger(\mathbf{A\Psi} - \mathbf{q}) \tag{6}$$

where $\mathbf{\Psi}^\dagger$ is the adjoint angular flux (or the Lagrange multiplier).

2.4 Optimality conditions or KKT conditions

The minimum of the Lagrangian is given by the optimality conditions

$$\begin{bmatrix} \mathbf{M_{meas}}(\mathbf{\Psi} - \tilde{\mathbf{\Psi}}) \\ \mathbf{A\Psi} - \mathbf{q} \\ {}^t\mathbf{\Psi}^\dagger \partial_{\mathbf{\Sigma}} \mathbf{A\Psi} \end{bmatrix} \tag{7}$$

where ^{t} denotes the transpose operation. This system of equation is nonlinear. A derivative-free (Neader-Mead) method and a Newton approach were used to solve this system of nonlinear equations.

2.5 Hessian system

The Newton solves require second derivatives of the Lagrangian, that is the formation of the Hessian matrix $\mathbf{H}$:

$$\mathbf{H} = \begin{bmatrix} \mathbf{M_{meas}} & \mathbf{A}^\dagger & \partial_{\mathbf{\Sigma}} \mathbf{A} \mathbf{\Psi}^\dagger \\ \mathbf{A} & 0 & \partial_{\mathbf{\Sigma}} \mathbf{A} \mathbf{\Psi} \\ {}^t\Psi^\dagger \partial_{\mathbf{\Sigma}} \mathbf{A} & {}^t\Psi \partial_{\mathbf{\Sigma}} \mathbf{A} & 0 \end{bmatrix} \tag{8}$$

and the Hessian system to be solved is

$$\begin{bmatrix} \mathbf{M_{meas}} & \mathbf{A}^\dagger & \partial_{\mathbf{\Sigma}} \mathbf{A} \mathbf{\Psi}^\dagger \\ \mathbf{A} & 0 & \partial_{\mathbf{\Sigma}} \mathbf{A} \mathbf{\Psi} \\ {}^t\Psi^\dagger \partial_{\mathbf{\Sigma}} \mathbf{A} & {}^t\Psi \partial_{\mathbf{\Sigma}} \mathbf{A} & 0 \end{bmatrix} \begin{bmatrix} \delta\mathbf{\Psi} \\ \delta\mathbf{\Psi}^\dagger \\ \delta\mathbf{\Sigma} \end{bmatrix} = - \begin{bmatrix} \mathbf{M_{meas}}(\mathbf{\Psi} - \tilde{\mathbf{\Psi}}) \\ \mathbf{A}\mathbf{\Psi} - \mathbf{q} \\ {}^t\mathbf{\Psi}^\dagger \partial_{\mathbf{\Sigma}} \mathbf{A} \mathbf{\Psi} \end{bmatrix} \tag{9}$$

In the Newton update equation,

$$\begin{bmatrix} \delta\mathbf{\Psi} \\ \delta\mathbf{\Psi}^\dagger \\ \delta\mathbf{\Sigma} \end{bmatrix}^{\ell+1} = \begin{bmatrix} \mathbf{\Psi} \\ \mathbf{\Psi}^\dagger \\ \mathbf{\Sigma} \end{bmatrix}^{\ell} + \alpha^\ell \begin{bmatrix} \delta\mathbf{\Psi} \\ \delta\mathbf{\Psi}^\dagger \\ \delta\mathbf{\Sigma} \end{bmatrix} \tag{10}$$

a damping parameter α^ℓ is applied based on a linear search technique (Wolfe condition). Also, the above Hessian system is not solved as is, but a Schur complement technique is employed to reduce the system to solely the material unknowns $\mathbf{\Sigma}$. Finally, several experiments can be used at once to estimate the same set of material unknowns ("replace" $\mathbf{\Delta}$ with $\sum_e \mathbf{\Delta}_e$). The two appendices provide a wealth of details regarding the developed methods.

3 Academic Achievements

3.1 Theses and Journal Articles

Two Master of Science theses (appended to this report) benefited from the support of this grant. Three journal articles

1. Yaqi Wang, Wolfgang Bangerth, Jean Ragusa "Three-dimensional h-adaptivity for the multigroup neutron diffusion equations", in Progress in Nuclear Energy, vol. 51 (2009), pp. 543-555.

2. Bruno Turcksin, Jean C. Ragusa, Wolfgang Bangerth, "Goal-oriented h-adaptivity for the multigroup SPN equations", in Nuclear Science and Engineering, vol. 165 (2010), pp. 305-319.

3. Moritz Allmaras, Wolfgang Bangerth "Reconstructions in ultrasound modulated optical tomography", in accepted for publication in Journal of Inverse and Ill-posed Problems, 2011.

In addition, an ongoing PhD dissertation has been partially funded by this grant.

3.2 Inverse Problem Seminars

To bring students and other participants in this project up to speed with some of the techniques used in inverse problems in diffusive imaging in general, and for this project in particular, PIs ran a working seminar for the first two years of this project. During the first semester, co-PI Bangerth presented the general framework used for deterministic inverse problems, i.e.,

1. their formulation as a least squares problem,
2. addition of the state equation as a constraint involving partial derivatives,
3. optimality conditions,
4. their discretization using finite element methods and adaptive meshes
5. efficient solution of the nonlinear system using Newton's method
6. efficient solution of the linear Newton steps, for example using the Schur complement method
7. a posteriori error estimation

This led the foundation for understanding how to approach inverse problems in general. We also specifically addressed how to apply these methods to a simple model problem involving an ODE and only two parameters, and to the problem at the heart of this project.

During the following semesters, we built on this understanding of inverse problem by considering an entirely different viewpoint: Bayesian, or statistical inversion of data. In particular, as a group, we read the books "Inverse Problem Theory" by A. Tarantola that presents the philosophical framework for Bayesian inversion, and "Statistical and Computational Inverse Problems" by J. Kaipio and E. Somersalo that derives a more concise mathematical formulation and in particular shows how to apply it in practice to a number of imaging problems, including to Electrical Impedance Tomography, a biomedical imaging method close to the topic of this project. We continued to jointly read literature on these topics through selected journal articles that were presented by one member and discussed as a group.

Participation in this working seminar included graduate students involved in this project as well as other graduate students and postdocs of the PIs who were not paid by this project but work on related topics, and interested faculty besides the two PIs. In addition to the general education of students and postdocs in these areas, one tangible outcome is a paper PI Bangerth wrote with his students on the statistical inversion of data for a model problem: identifying gravity and air friction coefficients for a body falling in air by measuring the distance it has fallen using the individual frames of a video, using data we obtained from an actual experiment. This expository paper, whose authors consist of 1 faculty, 2 postdocs and 5 graduate students, is currently under review by SIAM Review.

4 References

[1] J. Baker McNeill, "100 percent cargo container scanning: A global disaster," Research report, Kathryn and Shelby Cullom Davis Institute for International Studies, 2008.

[2] Jorina Fontelera, "Homeland Security to Miss Cargo Scanning Deadline," ThomasNet News, March 4, 2009.

[3] Dennis Slaughter, Mark Accatino, Adam Bernstein James Candy, Arden Dougan, James Hall, Alex Loshak, Doug Manatt, Alan Meyer, Bert Pohl, Stanley Prussin, Rosemary Walling, and David Weirup. Detection of Special Nuclear Material in Cargo Containers Using Neutron Interrogation. Rep. no. UCRLID- 155315. Livermore: University of California, Lawrence Livermore National Laboratory, 2003.

[4] United States. Government Accountability Office. Natural Resources and Environment. Combating Nuclear Smuggling: DHSs Cost-benefit Analysis to Support the Purchase of New Radiation Detection Portal Monitors Was Not Based on Available Performance Data and Did Not Fully Evaluate All the Monitors Costs and Benefits. By Gene Aloise. Washington, DC: Government Accountability Office, 2006.

[5] Zeyun Wu, "Advances in inverse transport methods and applications to neutron tomography," Ph.D. dissertation, Texas A&M University, College Station, Texas, December 2010.

A Appendix 1

APPLICATION OF A CONSTRAINED OPTIMIZATION TECHNIQUE TO THE IMAGING OF HETEROGENEOUS OBJECTS USING DIFFUSION THEORY

A Thesis

by

MATTHEW RYAN STERNAT

Submitted to the Office of Graduate Studies of
Texas A&M University
in partial fulfillment of the requirements for the degree of

MASTER OF SCIENCE

December 2009

Major Subject: Nuclear Engineering

APPLICATION OF A CONSTRAINED OPTIMIZATION TECHNIQUE TO THE IMAGING OF HETEROGENEOUS OBJECTS USING DIFFUSION THEORY

A Thesis

by

MATTHEW RYAN STERNAT

Submitted to the Office of Graduate Studies of
Texas A&M University
in partial fulfillment of the requirements for the degree of

MASTER OF SCIENCE

Approved by:

Chair of Committee,	Jean C. Ragusa
Committee Members,	Wolfgang Bangerth
	William S. Charlton
Head of Department,	Raymond Juzaitis

December 2009

Major Subject: Nuclear Engineering

ABSTRACT

Application of a Constrained Optimization Technique to the Imaging of Heterogeneous Objects Using Diffusion Theory. (December 2009)

Matthew Ryan Sternat, B.S., Texas A&M University

Chair of Advisory Committee: Dr. Jean C. Ragusa

The problem of inferring or reconstructing the material properties (cross sections) of a domain through noninvasive techniques, methods using only input and output at the domain boundary, is attempted using the governing laws of neutron diffusion theory as an optimization constraint. A standard Lagrangian was formed consisting of the objective function and the constraints to satisfy, which was minimized through optimization using a line search method. The chosen line search method was Newton's method with the Armijo algorithm applied for step length control. A Gaussian elimination procedure was applied to form the Schur complement of the system, which resulted in greater computational efficiency.

In the one energy group and multi-group models, the limits of parameter reconstruction with respect to maximum reconstruction depth, resolution, and number of experiments were established. The maximum reconstruction depth for one-group absorption cross section or multi-group removal cross section were only approximately 6-7 characteristic lengths deep. After this reconstruction depth limit, features in the center of a domain begin to diminish independent of the number of experiments. When a small domain was considered and size held constant, the maximum reconstruction resolution for one group absorption or multi-group removal cross section is approximately one fourth of a characteristic length. When finer resolution then this is considered, there is simply not enough information to recover that many region's cross sections independent of number of experiments or flux to cross-section mesh

refinement.

When reconstructing fission cross sections, the one group case is identical to absorption so only the multi-group is considered, then the problem at hand becomes more ill-posed. A corresponding change in fission cross section from a change in boundary flux is much greater then change in removal cross section pushing convergence criteria to its limits. Due to a more ill-posed problem, the maximum reconstruction depth for multi-group fission cross sections is 5 characteristic lengths, which is significantly shorter than the removal limit.

To better simulate actual detector readings, random signal noise and biased noise were added to the synthetic measured solutions produced by the forward models. The magnitude of this noise and biased noise is modified and a dependency of the maximum magnitude of this noise versus the size of a domain was established. As expected, the results showed that as a domain becomes larger its reconstruction ability is lowered which worsens upon the addition of noise and biased noise.

To my father and mother, Louis Sternat Jr. and Patricia Sternat

ACKNOWLEDGMENTS

I would like to acknowledge my father and mother, Louis Sternat Jr. and Patricia Sternat, for their guidance, love and support through this journey. They always allowed me to pursue my passion for science. I would also like to acknowledge the rest of my family and friends for allowing me to become the person I am today.

I further acknowledge Dr. Jean C. Ragusa for his advice, advisory, and allowing me to work on this project and Dr. Wolfgang Bangerth for help with optimization methods and techniques.

TABLE OF CONTENTS

CHAPTER Page

CHAPTER Page

LIST OF TABLES

LIST OF FIGURES

FIGURE Page

FIGURE Page

FIGURE Page

CHAPTER I

INTRODUCTION

A. Objective

In the field of nuclear and global security, smuggling of special nuclear materials by transportation in containers on boats poses strong threat. To prevent this possible smuggling pathway, a detection system must be implemented that will have the ability to detect high enriched uranium (HEU) where current detection systems cannot. Due to self-shielding and long half-lives, uranium can be hard to detect through conventional methods, especially in large scale systems such as cargo containers. There are approximately 30,000 ships docking at the United States per year currently and efficient detection methods must be implemented. As of the 9/11 Commission Act of 2007, foreign seaports must scan 100 percent of the cargo entering the United States by 2012.[1]

A possible method of detection would be an active neutron imaging technique which would involve incident beams of neutrons upon the cargo container and neutron detectors surrounding the container. Using these detector readings and a constrained optimization technique, reconstructions of the material properties inside a container could be performed to determine the contents. We propose to address this parameter identification by posing it as an optimal control problem where a cost function is to be minimized. This cost function is defined as the difference between the boundary detector measurements and the boundary neutron fluxes computed from the inferred material properties inside the cargo. While many sets of material parameters may

---

The journal model is *Nuclear Science and Engineering*.

have the ability to reconstruct the outer detector readings, constraints upon these must be applied to limit the number of solutions. The valid constraint used in this work will involve the governing conservation law of neutron physics in the container, thereby limiting the solution of material parameters to a realistic or physical case.

This is an optimal control problem because the difference between the computed iterative solution at the boundary and the neutron detector readings must be minimized while satisfying the neutron transport equation or an approximation of it. The equations derived from the optimization process are nonlinear, naturally requiring a descent method to solve them. This problem is ill-posed because small changes in the material properties can often lead to large changes in the neutron fluxes at the boundaries. Application of iterative methods cannot guarantee convergence for any realistic initial guess due to the ill-posedness of this nonlinear problem.

B. Imaging

Active neutral particle imaging techniques involve illuminating a domain with beams of particles of known intensity and taking measurements around the domain of the boundary outflow in an orientation shown in Figure I-1. Active neutral particle imagining is performed to reconstruct information of the inside of the domain. The location, energy, and angle of incidence of the incoming particles can be varied and more information can be gathered. With multiple experiments of incoming beams around the domain, the material properties reconstruction satisfying all experiments at once can yield improved reconstruction.

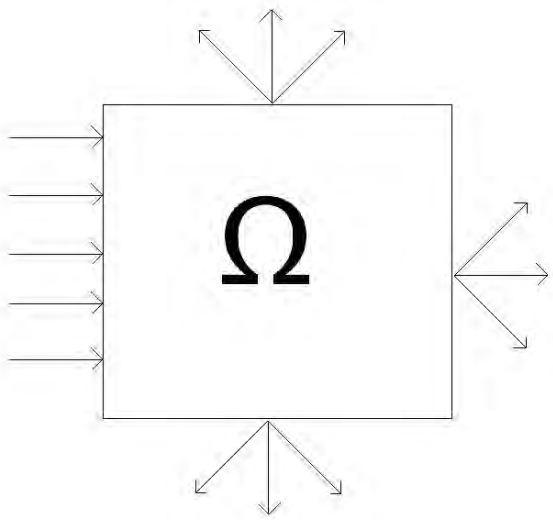

Fig. I-1. Example of incoming and outgoing particle currents

An example of this is optical tomography,[2] where a nonlinear system containing nonlinear combinations of the parameters intended to be reconstructed and the state variables is formed by the equations that define how light is transmitted and scattered through an object and often have no analytical solution.[3] By observing the light exiting the tissues, a reconstruction of the absorption and scattering coefficients inside the sample is performed.[3] These problems are solved iteratively using forward models to solve for the outgoing currents based on an initial guess on the interaction coefficients directly, and nonlinear optimization techniques to update the interaction coefficients[4].[5] This algorithm process is repeated until the iterative solution converges with the observed light exiting the tissues. This is very similar to the problem of special nuclear material (SNM) smuggling, but instead of biological matter, containers that can be up to many optical thicknesses deep are to be imaged using neutrons.

Another example of neutral particle imaging is in large ports for object detection. There are systems that use photons that operate in the 6-9 MeV range to image large

cargo containers. Most of currently implemented cargo imaging uses either x-rays or gamma rays. The x-ray systems are commonly used to ensure containers are empty without opening them or to determine contents of smaller containers where gamma rays are not needed. These types of systems are capable of producing images of large containers and trucks with spatial resolution of 9mm for the gamma systems and 2mm for x-ray systems.[6] While these types of systems can produce an image of the internal contents of a container, they cannot by themselves determine if fissile material is present. This is where a multigroup neutron imaging system would have the greatest impact. If a system were able to reconstruct fission cross sections to determine whether fissile material were present accurately, greater detection probability of smuggled HEU could be achieved.

Neutron imaging varies from gamma or x-ray imaging in the way they interact with matter quite differently then x-rays do, having a high interaction probability with hydrogen and much lower attenuation in heavier elements such as lead. While x-ray interaction probability is directly proportional to the atomic number of the material, neutron interaction is isotope-dependent causing both radiography mechanisms to excel in different media types.[7] Common examples of neutron radiography include nuclear fuel surveys, multi-phase flow imaging, and explosive device imaging. In the case at hand, HEU could easily be shielded from x-rays causing methods involving x-rays or radiation emitted from the material itself to be ineffective. Neutron interaction probabilities are energy-dependent, where neutrons of typical source energy have high scattering interaction probability in many materials, limiting the ability of larger scale imaging.

C. Optimization and Inverse Problem Solving

The majority of inverse problems or imaging techniques involve an optimization process in which a function is minimized or maximized by iterating the functions variables, often subject to constraints. The most commonly used methods to solve problems of any type involve iterative algorithms. In the optimization process, the optimum of a given function is obtained by solving the optimality conditions using an optimization algorithm. There is no universal optimization algorithm but instead a collection of algorithms in which each is valid for specific problem types.[8]

An example of application of inverse transport is the determination of interface locations in a multilayer domain of unknown dimensions. In this specific example, source gamma-rays were passed through a domain and observed at boundaries, then the location of the interfaces is solved for using optimization methods.[9] This is similar to the problem at hand except that instead of the material properties being known and the interface locations reconstructed, the material properties are unknown but reconstructed and assumed piecewise constant over a mesh.

D. Thesis Overview

The next chapter provides an in depth look at optimization methods from a mathematical standpoint. This chapter provides a complete step by step approach to optimization problems including specific methods.

Chapter III contains the development and implementation of the presented optimization methods to the inverse problem using diffusion theory.

Chapter IV presents the results of reconstructions of various domains. Many tests were performed in order to have an understanding of the workable space with respect to domain size, mesh size, number of experiments, and measurement location.

CHAPTER II

OPTIMIZATION METHODS

The goal of an optimization problem is to find the combination of parameters that optimize a given quantity subject to some restrictions or constraints.[10] The parameters that may be changed in the process of optimization are called control or decision variables while the restrictions on parameters are known as constraints.[10] Mathematically speaking, optimization is the minimization or maximization of an objective function defined by a problem statement and is subject to constraints on its variables. Often a vector x is formed that consists of the unknowns or parameters, f if the objective function, a scalar function of x, that we want to maximize or minimize, and a series of constraint functions, c_i, which are scalar functions of x that define constraints the unknown vector x must satisfy. Using this notation, the optimization problem can be written as shown in Equation 2.1.

$$\min_{x \in R^n} f(x) \text{ subject to } \begin{array}{l} c_i(x) = 0, \ i \in \xi \\ c_i(x) \geq 0, \ i \in \mathcal{I} \end{array} \tag{2.1}$$

where c_i can be an equality or inequality constraint and ξ and $\mathcal{I}$ are the sets of equality and inequality constraints.

This chapter provides an overview of optimization methods in general, starting with section A on optimization problem classifications.Section B provides the optimality conditions. The section of these optimality conditions is then detailed in section C using steepest descent and Newton's method. This chapter will then cover convergence criteria D, step-length control E and conclude with the Schur complement method employed to reduce the system's dimensions F.

A. Optimization Classifications

In deterministic optimization methods, first and second derivatives of the objective function, $f(x)$, need to be computed. These problems are classified by the type of their control variables and nature of their objective functions which are usually linear, quadratic, or fully nonlinear.[10] In certain cases, this function can be discontinuous and may contain integers and binary variables; these problems can only be optimized using discrete optimization methods for which derivatives are not defined. Other classes of problems, where the components of the given function are allowed to be real numbers can be optimized continuously. These continuous functions are normally easier to solve because they are often smooth and twice differentiable.[8]

When a problem is considered, it is classified by the nature of its objective function where some problems have constraints upon their variables and some do not. Problems that involve constrained variables are optimized using constrained optimization. Sometimes these constraints play a important role in determining the solution and an example of a constrained objective function can be seen in Figure II-1.

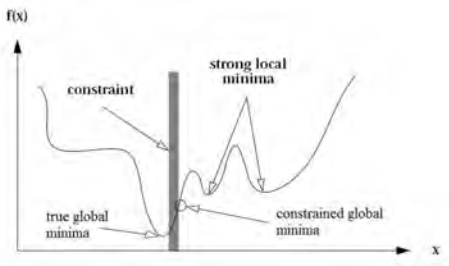

Fig. II-1. Example of a constrained objective function

For instance, in a budgetary problem, if the global solution lies outside the limits due to budgetary constraints, a local solution that lies within these constraints will be the best solution.[8] Whereas in fully unconstrained optimization, there are no limits

on any of the variables and the global minimum is the true function minimum as shown in Figure II-2.

Fig. II-2. Example of an unconstrained objective function

Sometimes, even if there are minor constraints on a problems variables, if they do not interfere with the optimization algorithms, unconstrained optimization can be applied.[8]

B. Optimality Conditions

To find the minimum of $f(x)$, conditions are applied to find where $\nabla f = 0$. When constraints are upon $f(x)$, for example $c(x) = 0$, then a Lagrangian functional is introduced such as in Equation 2.2.

$$\min_{x \in R^n} f(x) \text{ subject to } c(x) = 0 \Leftrightarrow \mathcal{L}(x, \lambda) = \nabla f + \lambda \nabla c(x) \tag{2.2}$$

where λ is a Lagrange multiplier. A saddle point in $\mathcal{L}$ is found where $\nabla \mathcal{L} = 0$, which is

$$\frac{\partial \mathcal{L}}{\partial x} = 0 = \nabla f + \lambda \nabla c \tag{2.3}$$

$$\frac{\partial \mathcal{L}}{\partial \lambda} = 0 = c(x) \tag{2.4}$$

where the first equation implies that $\nabla f \propto \nabla c$ and in the second equation the con-

straint arises $c(x) = 0$. These derivatives of the Lagrangian form a set of Karush-Kuhn-Tucker conditions or optimality conditions to be satisfied. Figure II-3 shows a simple iso-contour plot of $f(x)$ with a $c(x) = 0$ line solution.

Fig. II-3. Iso-contour plot showing an objective function and a constraint

C. Line Search Methods

In a line search method, algorithms choose a direction p_k and search along this direction from the current iterate for a new iterate that is closer to the optimality conditions.[8] There are various methods that can be used to determine a line search direction along with many algorithms to determine how far in that direction to go.[8] The goal of this optimization problem is the minimization of $f(x)$ while satisfying any given conditions. At this minimum $\partial_j \mathcal{L}(x) = 0$ where j is any field variable in $\mathcal{L}(x)$. Just as in any iterative method, an initial guess is made and at this iterate $\nabla \mathcal{L}(x^k) \neq 0$. We will now describe two such techniques: the steepest descent and Newton's descent and then provide an example of a step-length control algorithm.

1. Steepest Descent

An obvious direction is the steepest descent. The steepest descent direction follows the opposite direction of the gradient, or the direction perpendicular to the iso-contours. For example in a simple two dimensional optimization scheme, this would be very

similar to a ball in a valley rolling to the bottom. This can be seen in Figure II-4, where X^* is the global minimum. The gradient of f is perpendicular to the iso-contour of $\mathcal{L}$.

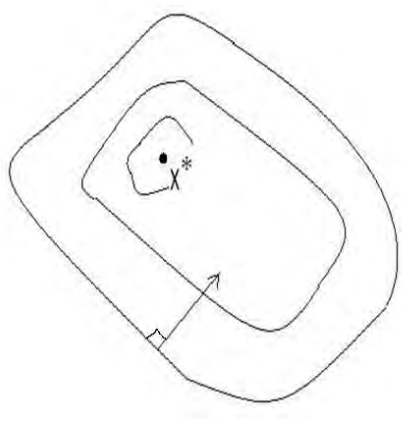

Fig. II-4. Steepest descent direction

In this steepest descent method, the descent direction is $p_k = -\nabla\mathcal{L}_k$ as shown in Equation 2.5.

$$x_{k+1} = x_k + \alpha p_k = x_k - \alpha\nabla\mathcal{L}_k \tag{2.5}$$

The steepest descent algorithm consists of the following:

1. Initialization: set k=0, set convergence criteria ϵ, choose x_k.
2. If $\|\nabla\mathcal{L}_k\| < \epsilon$ then exit, otherwise continue.
3. Compute $p_k = -\nabla\mathcal{L}_k$
4. Determine step length α_k (see Section 2.4).
5. Compute new update according to Eq. 2.5.
6. $k \leftarrow k + 1$ and go to 2.

This method requires only first derivatives, tends to get stuck in local minima, and is slowly converging while it iteratively takes steps in the gradient direction to a new solution with lower optimality condition. The steepest descent direction is updated at every step indexed by k and its progress is slow as some regions of indefinite curvature are encountered especially near a solution.[10] The convergence rate of this method is much slower than other higher order methods.

2. Newton's Method

A significantly more efficient higher order method can be derived from where the steepest descent method left off. Newton's method is comprised of second derivatives and is a curve of best fit method. This uses a line search direction other then the steepest descent, and is derived from the second order Taylor series approximation of $f(x_k + p)$ and is shown in Equation 2.6.

$$\mathcal{L}(x_k + p) \approx \mathcal{L}_k + p^T \nabla \mathcal{L}_k + \frac{1}{2} p^T \nabla^2 \mathcal{L}_k p = m_k(p) \tag{2.6}$$

An example of such direction can be shown in Figure II-5.

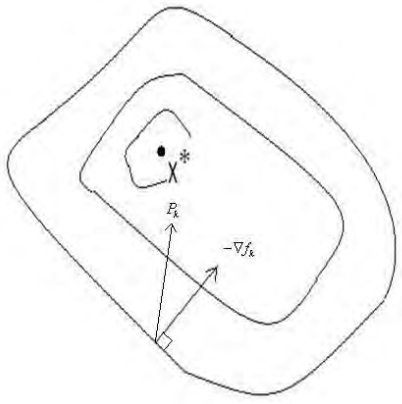

Fig. II-5. Newton's method vs. steepest descent direction

Using this second-order Taylor series approximation, the vector p that minimizes $m_k(p)$ is obtained by setting the derivative of $m_k(p)$ to zero leaving Equation 2.7.

$$\nabla \mathcal{L}_k + \nabla^2 \mathcal{L}_k p_k = 0 \tag{2.7}$$

where $\nabla^2 f_k = H$, the Hessian matrix. Then solving for p_k yields

$$p_k = -(\nabla^2 \mathcal{L}_k)^{-1} \nabla \mathcal{L}_k = -H^{-1} \nabla \mathcal{L}_k \tag{2.8}$$

$$x_{k+1} = x_k + \alpha p_k = x_k - \alpha H^{-1} \nabla \mathcal{L}_k \tag{2.9}$$

This Newtonian search direction tries to quadratically approximate a curve at iterate x_k and goes to the minimum of the quadratic fit. For a simple quadratic system, the minimum of $f(x)$ could be met after one step. Due to the nonlinearity and complexity of most systems, Newton's method often is applied where steepest descent methods will not converge.

The steepest descent and Newton's method are both of the form:

$$x_{k+1} = x_k + \alpha p_k = x_k - \alpha B^{-1} \nabla f_k, \tag{2.10}$$

with $B = I$, for steepest descent and $B = H^{-1}$, for Newton's method.

D. Convergence Criteria

The nonlinear system in Equation 2.4 will converge when the optimality conditions are satisfactory close to their solution. Some very nonlinear systems with random noise and bias will be very difficult to drive the optimality conditions close to the true solution. At the optimum, the optimality conditions will be met but when constraints are present the solution that is closest to the optimality conditions while

satisfying the constraints will be the global solution. For example, if the true global solution was unreachable due to constraints then the convergence criteria of the optimality conditions will not be achievable and the closest solution to these optimality conditions will be the solution.

E. Step-Length Selection Control and Algorithms

Now that a line search direction has been determined, how far to travel in that direction is established next. When the objective function is not smooth, a full Newtonian direction step may not lead to a reduction in optimality condition. Simple algorithms can be used to attempt to ensure the optimality conditions are lowered. Starting with the general *sufficient decrease* condition:

$$\mathcal{L}(x_k + \alpha p_k) - \mathcal{L}(x_k) < \alpha\lambda\nabla\mathcal{L}(x_k)^T p_k \tag{2.11}$$

where the descent direction derived from Newton's Method:

$$p_k = -H^{-1}\nabla\mathcal{L}(x) \tag{2.12}$$

where $\lambda \in (0, 1)$ is an algorithmic parameter typically around 10^{-4}. Beginning with $\alpha = 1$ repeatedly reduce α using any strategy that satisfies the general *sufficient decrease* condition.

$$\alpha_+ \in [\beta_{low}\alpha_c, \beta_{high}\alpha_c] \tag{2.13}$$

where $0 < \beta_{low} < \beta_{high} < 1$. The choice of $\beta = \beta_{low} = \beta_{high}$ is a simple rule in the Armijo algorithm shown below.[8]

1. Initialization: set α=1 and $\lambda \in (0, 1)$, set convergence criteria ϵ, choose x_k.

2. If $\mathcal{L}(x_k + \alpha p_k) - \mathcal{L}(x_k) < \alpha\lambda\nabla\mathcal{L}(x_k)^T p_k$, $x_{k+1} = x_k + \alpha p_k$. If not, continue.

3. Reduce α, return to step 2.

In an exact line search, the special case where λ leads to the exact minimum of $\mathcal{L}(x_c + \alpha p_k)$, is not only more expensive computationally but can often degrade the performance of the algorithm in general.

F. Schur Complement Method

The Schur Complement Method is a process of system simplification for a system involving a Karush-Kuhn-Tucker (KKT) type matrix.[8] It is a method that involves eliminating variables in a system to simplify and often obtain a linear system of one variable. One example of such matrix system can be shown in Equation 2.14.

$$\begin{bmatrix} G & A^T \\ A & 0 \end{bmatrix} \begin{bmatrix} p \\ \lambda \end{bmatrix} = \begin{bmatrix} g \\ h \end{bmatrix} \text{ where: } \dim(p) >> \dim(\lambda) \tag{2.14}$$

This KKT matrix has blocks of entries equal to zero and can easily simplified by simple algebra. A typical KKT matrix may have more rows of blocks, as many multivariate problems have multiple optimality conditions, but can be simplified in the same manner. After assuming G is positive definite, p is solved for in the first equation in 2.14 in terms of λ then substituted in the second equation leaving a system of λ alone as shown in Equation 2.15.

$$\lambda = A^{-T}(g - GA^{-1}h) \tag{2.15}$$

This smaller system is solved for λ and then the other vector variable p can be directly solved for as shown in Equation 2.16.

$$Gp = A^T\lambda - g \tag{2.16}$$

This method involves a matrix inversion of G and A^T which often results in signif-

icantly lower condition number than inverting the full original system matrix. This method of system simplification can be applied to reduce system runtime and improve computational efficiency.

CHAPTER III

INVERSE DIFFUSION MODELS

Neutron imaging is type of non-invasive inverse problem involving incoming and outgoing neutron beams where measurements are made only on the boundary of a domain. The neutron transport equation defines how neutrons behave in matter through various interaction types and can be used in inverse problems. An approximation to the transport model is diffusion theory, which introduces some simplicity for handling the angular dependence of the neutron population. In this thesis, we use the diffusion approximation to model the distribution of particles.

In inverse theory, many problems are ill-conditioned or are ill-posed, where a small variation in the input data causes a large change in the results.[11] In inverse diffusion methods, the flux solution to be solved for depends on unknown internal parameters of the domain. Generally, an initial guess is set for the domain parameters, then the flux is solved and the domain parameters are updated using optimization methods.

This chapter begins with an introduction to neutron diffusion theory and the application of a finite element method to solve neutron diffusion problems. The implementation of the previous chapters optimization methods applied to inverse diffusion models are described next, first deriving optimality conditions and then employing Newton's method to solve them. The optimum control problem is formulated for multiple experiments in the context of the multigroup diffusion approximation.

A. Neutron Diffusion Theory

The neutron diffusion equation is derived from the Boltzmann transport equation by integrating over all directions and using the diffusion theory expression for the neutron current derived from Fick's Law.[12] The one-group neutron diffusion equation, shown in Equation 3.1 and 3.2, is a phase-space dependent equation that relates the neutron scalar flux phase-space distribution across a domain to its nuclear properties.[12]

$$-\nabla \cdot D(\vec{r})\nabla\Phi + (\Sigma_a(\vec{r}) - \nu\Sigma_f(\vec{r}))\Phi = Q(\vec{r}) \text{ in } \Omega \tag{3.1}$$

$$\frac{\Phi}{4} + \frac{D(\vec{r})}{2}\partial_n\Phi = J^{inc}(\vec{r}) \text{ in } \partial\Omega \tag{3.2}$$

B. Finite Element Diffusion Solver

The forward diffusion models used in this problem are solved numerically using finite element methods. The finite element method is a numerical technique for finding approximate solutions of partial differential equations. This method differs from finite difference in such that finite difference methods approximate PDE equations while finite element methods approximate their solutions. Both of these methods discretize the domain into a mesh and the finite element method used in this work approximates the PDE's solution as a piecewise bi-linear function across each mesh cell.

In the finite element setting, the diffusion equation becomes:

$$\left[A_D + A_\Sigma + \frac{1}{2}M_{\partial\Omega}\right]\Phi = A\Phi = F \tag{3.3}$$

with:

1.

$$A_D(i,j) = \int_\Omega \nabla b_i \cdot \nabla b_j \tag{3.4}$$

If D is constant, it can be factored out and

$$A_D = D \times S \tag{3.5}$$

$$\text{with } S(i,j) = \int_\Omega D \nabla b_i \cdot \nabla b_j. \tag{3.6}$$

S is known as the stiffness matrix

2.

$$A_\Sigma(i,j) = \int_\Omega \Sigma b_i b_j \tag{3.7}$$

If Σ is constant, it can be factored out and

$$A_\Sigma = \Sigma \times M \tag{3.8}$$

$$\text{with } M(i,j) = \int_\Omega b_i b_j. \tag{3.9}$$

M is known as the mass matrix.

3.

$$M_{\partial\Omega}(i,j) = \int_{\partial\Omega} b_i b_j \tag{3.10}$$

4.

$$F(i) = \int_\Omega Q b_i + 2 \int_{\partial\Omega} J^{inc} b_i \tag{3.11}$$

5. Now, Φ is to be understood as a vector containing the flux values Φ_i at the nodes.

1. Finite Element Meshes

There are a variety of element meshes that can be implemented with finite element method. The most common of these are triangular and rectangular elements. After the domain has been broken elements, a set of piecewise polynomials are used for approximation. This must result in a function that is continuous with an integrable or continuous first or second derivative on the entire region. Polynomials of linear type in x and y in Equation 3.12 are often used with triangular elements and polynomials of bilinear type, shown in Equation 3.13 are used with rectangular elements.

$$\Phi(x, y) = a + bx + cy \tag{3.12}$$

$$\Phi(x, y) = a + bx + cy + dxy. \tag{3.13}$$

The two dimensional domain is broken up into finite element meshes. This consists of a fine mesh to be used in the flux solver and a coarse mesh that will be the regions where the cross section (taken to be piece-wise constant) are reconstructed. The difference between these two meshes is a refinement which is variable in each dimension of the domain. This refinement is necessary due to the ill-posed problem and lack of information required to solve this inverse diffusion problem. An example of these meshes and refinement is shown in Figure III-1.

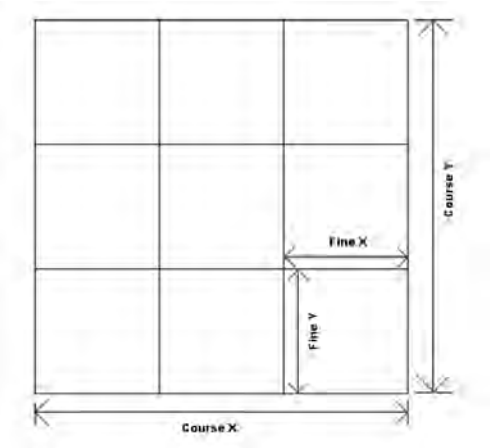

Fig. III-1. Example of the finite element meshes for the diffusion problem

2. Finite Element Methods

An attractive feature of the finite element method is its ability to handle complicated geometries with relative ease. This enables much more complicated domains and geometries to be solved where the finite difference method in its basic form is restricted to handle rectangular shapes and simple variations of. One reason for this is the finite element method's relative easy with which the boundary conditions are handled.[13] A lot of problems have boundary conditions involving derivatives and irregularly shaped boundaries which are difficult to handle using finite difference techniques.[13] The finite difference method handles these boundary conditions by approximating the derivative using a difference quotient at the grid points where irregular shaping of the boundary makes the grid point locations difficult.[13] The finite element method handles the boundary conditions in a functional's integral that is being minimized, which is independent of the particular boundary conditions of the problem itself.[13]

C. Optimization Functional

1. Misfit: To Minimize

When an iterative solution is considered, a function called the misfit is introduced which represents the iterative solutions's (Φ) distance from the measured solution (z) at the boundary. In the case at hand, a synthetic measured solution is used by evaluating the forward model with the true material parameters. While iterating to satisfy the optimality conditions, this misfit represents the distance of Φ from z at the boundary and should converge to zero as the solution is approached. In the case of the problem, the misfit will be defined by Equation 3.14.

$$\text{misfit} = \frac{1}{2}\int_{\partial\Omega'} \left[\Phi - z\right]^2, \tag{3.14}$$

where $\partial\Omega'$ represents the portion of $\partial\Omega$ where measurements are made. In the finite element setting:

$$\text{misfit} = \frac{1}{2}\left[\Phi - z\right]^T M_{meas}\left[\Phi - z\right], \tag{3.15}$$

where

$$M_{meas}(i,j) = \int_{\partial\Omega'} b_i b_j. \tag{3.16}$$

If the entire boundary is used to measure data, then $M_{meas} = M_{\partial\Omega}$. This misfit is directly used in the Lagrangian.

2. Lagrangian Functional

In constraint optimization problems, a $\mathcal{L}$ functional is formed and minimized consisting of two parts, one being the misfit representing distance from the true solution at the boundary and the other being constraints, here the diffusion equation acts as the governing equation, or in other words, $\mathcal{L} = \text{misfit} + \text{constraint}$. The optimality

conditions are derived from first derivatives of this Lagrangian with respect to each field variable and will be minimized in an iterative manner. The field variables are: Φ, λ, and Σ where Φ is the neutron flux, λ is the Lagrange multiplier or adjoint flux, and Σ is the set of piecewise continuous cross sections for the domain.

Constraints must be applied as several solution sets may satisfy the misfit conditions and application of constraints helps in selecting these solutions. The governing physics of the domain act as a constraint in the problem at hand and may help select a solution that physically realistic. Application of the neutron diffusion equation here will be the constraint of choice, but additional constraints may be implemented involving physical limits: $3\Sigma_a < \frac{1}{D}$, $\Sigma_a > 0$, $\Sigma_f < \Sigma_a$ and ensuring a domain remains subcritical ($k_{eff} < 1$). Most all problems objective functions are smooth enough to where the additional constraints are not needed. The goal of this optimization problem is to find the saddle point in a Lagrangian functional $\mathcal{L}$. If only Σ is to be determined, then

$$\mathcal{L}(\Phi, \lambda, \Sigma) = \frac{1}{2}\left[\Phi - z\right]^T M_{meas}\left[\Phi - z\right] + \lambda^T \left\{ \left[A_D + A_\Sigma + \frac{1}{2} M_{\partial\Omega} \right] \Phi - F \right\}. \quad (3.17)$$

The KKT optimality conditions arise as the derivatives of the Lagrangian with respect to each field variable and must be satisfied as the solution is approached. When $\mathcal{L}$ is the optimum, each of these optimality conditions will be satisfied.

$$\frac{\partial \mathcal{L}}{\partial \Phi} = M_{meas}\left[\Phi - z\right] + \left[A_D + A_\Sigma + \frac{1}{2} M_{\partial\Omega} \right]^T \lambda = 0, \quad (3.18)$$

$$\frac{\partial \mathcal{L}}{\partial \lambda} = \left[A_D + A_\Sigma + \frac{1}{2} M_{\partial\Omega} \right] \Phi - F = 0, \quad (3.19)$$

$$\frac{\partial \mathcal{L}}{\partial \Sigma} = \lambda^T \partial_\Sigma A \Phi = 0. \quad (3.20)$$

There are several features embedded in the presented optimality conditions, such as in Eq. 3.19 the constraint to the optimization problem arises as the diffusion residual must approach zero. In Eq. 3.18 the adjoint diffusion term arises with the misfit as a forcing term which too must approach zero as the method nears the solution. The Lagrange multiplier, λ, has a clear meaning as the adjoint flux. Equations 3.18-3.20 form a nonlinear system of equations to be satisfied. These KKT optimality conditions form a nonlinear system of equations, therefore Newton's method is employed.

D. Hessian System

Upon implementing Newton's method of optimization, the Hessian matrix must be formed. This Hessian matrix is the Jacobian matrix of the KKT optimality conditions which is composed of second derivatives of $\mathcal{L}$. The derivatives of the optimality condition are taken with respect to each field variable and put together to form a matrix.

$$\frac{\partial^2 \mathcal{L}}{\partial \Phi^2} = M_{meas} \tag{3.21}$$

$$\frac{\partial^2 \mathcal{L}}{\partial \lambda^2} = 0 \tag{3.22}$$

$$\frac{\partial^2 \mathcal{L}}{\partial \Sigma^2} = 0 \tag{3.23}$$

$$\frac{\partial^2 \mathcal{L}}{\partial \Sigma \partial \Phi} = \partial_\Sigma A^T \Phi \tag{3.24}$$

$$\frac{\partial^2 \mathcal{L}}{\partial \Sigma \partial \lambda} = \partial_\Sigma A \Phi \tag{3.25}$$

$$\frac{\partial^2 \mathcal{L}}{\partial \lambda \partial \Phi} = \left[A_D + A_\Sigma + \frac{1}{2} M_{\partial\Omega} \right] \tag{3.26}$$

Note that $M^T = M$ and $\left[A_D + A_\Sigma + \frac{1}{2} M_{\partial\Omega} \right]^T = \left[A_D + A_\Sigma + \frac{1}{2} M_{\partial\Omega} \right]$ in the case of one-group diffusion approximation. To simplify the system, the notation

$\left[A_D + A_\Sigma + \frac{1}{2}M_{\partial\Omega}\right] = A$ will be used, yielding the Hessian system below in Equation 3.27.

$$\begin{bmatrix} M_{meas} & A^T & \partial_\Sigma A\lambda \\ A & 0 & \partial_\Sigma A\Phi \\ \lambda^T\partial_\Sigma A & \Phi^T\partial_\Sigma A & 0 \end{bmatrix} \begin{bmatrix} \delta\Phi \\ \delta\lambda \\ \delta\Sigma \end{bmatrix} = - \begin{bmatrix} M_{meas}\left[\Phi - z\right] + A^T\lambda \\ A\Phi - F \\ \lambda^T\partial_\Sigma A\Phi \end{bmatrix} \tag{3.27}$$

where $\delta\Phi$, $\delta\lambda$, and $\delta\Sigma$ are updates and give the Newton iterate:

$$H\delta x^k = -F(x^k) \tag{3.28}$$

$$x^{k+1} = \delta x^k + x^k. \tag{3.29}$$

E. Implementation of Schur Complement

This Hessian system can be simplified to reduce run time by a Gauss elimination of $\delta\Phi$ and $\delta\lambda$ to arrive at a system with only $\delta\Sigma$. The main matrix that is inverted in the Schur complement solution has a lower condition number then the straight forward Hessian system.

The second row of the above Hessian system is solved first for $\delta\Phi$ in terms of $\delta\Sigma$ and constants.

$$A\delta\Phi + \partial_\Sigma A\Phi\delta\Sigma = -A\Phi + F \tag{3.30}$$

$$\delta\Phi = A^{-1}\left(-A\Phi + F - \partial_\Sigma A\Phi\delta\Sigma\right) \tag{3.31}$$

The first row of the above Hessian system is solved for $\delta\lambda$ in terms of $\delta\Phi$ and $\delta\Sigma$.

$$M_{meas}\delta\Phi + A^T\delta\Sigma + \partial_\Sigma A\lambda\delta\Sigma = -M_{meas}\left[\Phi - z\right] - A^T\lambda \tag{3.32}$$

$$\delta\lambda = A^{-T}\left(-M_{meas}\left[\Phi - z\right] - A^T\lambda - M_{meas}\delta\Phi - \partial_\Sigma A\lambda\delta\Sigma\right) \tag{3.33}$$

$$\delta\lambda = A^{-T}\begin{pmatrix} -M_{meas}\left[\Phi - z\right] - A^T\lambda - M_{meas}\cdot \\ \left[A^{-1}\left(-A\Phi + F - \partial_\Sigma A\Phi\delta\Sigma\right)\right] - \partial_\Sigma A\lambda\delta\Sigma \end{pmatrix} \tag{3.34}$$

These solutions for $\delta\Phi$ and $\delta\lambda$ can be plugged back into the third row of the above Hessian system to solve for $\delta\Sigma$. Starting with the third row from Equation 3.27:

$$\lambda^T M\delta\Phi + \Phi^T M\delta\lambda = -\lambda^T M\Phi \tag{3.35}$$

then filling $\partial\Phi$ and $\partial\lambda$ solutions:

$$\begin{aligned} \Phi^T\partial_\Sigma A\left(A^{-T}\begin{pmatrix} -M_{meas}\left[\Phi - z\right] - A^T\lambda - M_{meas}\cdot \\ \left[A^{-1}\left(-A\Phi + F - \partial_\Sigma A\Phi\delta\Sigma\right)\right] - \partial_\Sigma A\lambda\delta\Sigma \end{pmatrix}\right) + \\ \lambda^T\partial_\Sigma A\left(A^{-1}\left(-A\Phi + F - \partial_\Sigma A\Phi\delta\Sigma\right)\right) = -\lambda^T\partial_\Sigma A\Phi \end{aligned} \tag{3.36}$$

then grouping terms with and without $\delta\Sigma$:

$$\begin{aligned} &\left[-\lambda^T\partial_\Sigma AA^{-1}\left(\partial_\Sigma A\Phi\right) + \Phi^T\partial_\Sigma A\left[A^{-T}\left(-M_{meas}A^{-1}\left(-\partial_\Sigma A\Phi\right) + \partial_\Sigma A\lambda\right)\right]\right]\left[\delta\Sigma\right] \\ &= \begin{array}{c} -\lambda^T\partial_\Sigma A\Phi - \lambda^T\partial_\Sigma AA^{-1}\left(-A\Phi + F\right) - \Phi^T\partial_\Sigma AA^{-1}\cdot \\ \left(-M_{meas}\left[\Phi - z\right] - A^T\lambda - M_{meas}A^{-1}\left(-A\Phi + F\right)\right) \end{array} \end{aligned} \tag{3.37}$$

The operator created on the left hand side of Eq. 3.37 is the Schur complement for the system and will be called S. The right hand side will be called U for simple notation.

$$S = -\lambda^T\partial_\Sigma AA^{-1}\left(M\Phi\right) + \Phi^T\partial_\Sigma A\left[A^{-T}\left(-M_{meas}A^{-1}\left(-\partial_\Sigma A\Phi\right) + \partial_\Sigma A\lambda\right)\right] \tag{3.38}$$

$$\delta\Sigma = S^{-1}U \tag{3.39}$$

This method for the one group case creates a system for $\delta\Sigma$ only which is significantly smaller in size then the original system shortening iteration runtime.

F. Extension to Multiple Experiments

To also enable greater reconstruction abilities, multiple experiments can be performed over a domain, each experiment involving different source locations. Every experiment has a unique flux and adjoint solution to reconstruct the same cross sections to better the likelihood of success. The most logical choices are to break the boundary into halves, quarters, eighths, and sixteenths. The optimality conditions and misfit will be reduced for each of these experiment's flux solutions while optimizing the same set of parameters for the domain. This will provide much more data and enable greater reconstruction ability then a single experiment. Many runs will be done with this code to test the limits of reconstruction with respect to various elements of the domain such as mesh size, number of experiments, variable refinement, and domain size.

1. Optimality Conditions

The Lagrangian with multiple experiments will be a simple summation over the Lagrangian for each experiment. This Lagrangian for a total of I experiments is:

$$\mathcal{L}(\Phi, \lambda, \Sigma) = \sum_{i=1}^{I} \frac{1}{2} \left[\Phi_i - z_i\right]^T M_{meas} \left[\Phi_i - z_i\right] + \sum_{i=1}^{I} \lambda_i^T \left[A_i\Phi_i - F_i\right] \tag{3.40}$$

Similar to the single experiment case, the optimality conditions to be satisfied are derived from the first derivatives with respect to Φ_i and λ_i for each experiment

and the same Σ as before.

$$\frac{\partial \mathcal{L}}{\partial \Phi_i} = M_{meas}\left[\Phi_i - z_i\right] + A_i^T \lambda_i \ \forall i \tag{3.41}$$

$$\frac{\partial \mathcal{L}}{\partial \lambda_i} = A_i \Phi_i - F_i \ \forall i \tag{3.42}$$

$$\frac{\partial \mathcal{L}}{\partial \Sigma} = \sum_{i=1}^{I} \lambda_i^T \partial_\Sigma A \Phi_i \tag{3.43}$$

This creates more conditions for the system to be satisfied enabling greater reconstruction ability.

2. Hessian System

The Hessian system for multiple experiments is similar to the single experiment case. The corresponding second derivatives for the Hessian system were derived for each experiment forming a new Hessian matrix.

$$\frac{\partial^2 \mathcal{L}}{\partial \Phi_i^2} = M_{meas,i} \tag{3.44}$$

$$\frac{\partial^2 \mathcal{L}}{\partial \lambda_i^2} = 0 \tag{3.45}$$

$$\frac{\partial^2 \mathcal{L}}{\partial \Sigma^2} = 0 \tag{3.46}$$

$$\frac{\partial^2 \mathcal{L}}{\partial \Sigma \partial \Phi_i} = \partial_\Sigma A^T \lambda_i \tag{3.47}$$

$$\frac{\partial^2 \mathcal{L}}{\partial \Sigma \partial \lambda_i} = \partial_\Sigma A \Phi_i \tag{3.48}$$

$$\frac{\partial^2 \mathcal{L}}{\partial \lambda \partial \Phi} = \sum_{i=1}^{I} A_D + A_\Sigma + \frac{1}{2} M_{\partial\Omega} \tag{3.49}$$

where $M_{meas,i}$ is the mass matrix corresponding to experiment i's measurement location. This multiple experiment Hessian system has identical equations for Φ and λ but with an equation for each experiment. These experiments all operate over the same

set of cross sections, therefore the final equation has terms from every experiment.

$$\begin{bmatrix} M_{meas,1} & 0 & A_1^T & 0 & \cdots & \partial_\Sigma A\lambda_1 \\ 0 & M_{meas,2} & 0 & A_2^T & \cdots & \partial_\Sigma A\lambda_2 \\ A_1 & 0 & \ddots & 0 & \cdots & \partial_\Sigma A\Phi_1 \\ 0 & A_2 & 0 & 0 & \cdots & \partial_\Sigma A\Phi_2 \\ \vdots & \vdots & \vdots & \vdots & \ddots & \vdots \\ \lambda_1^T\partial_\Sigma A & \lambda_2^T\partial_\Sigma A & \Phi_1^T\partial_\Sigma A & \Phi_2^T\partial_\Sigma A & \cdots & 0 \end{bmatrix} \begin{bmatrix} \delta\Phi_1 \\ \delta\Phi_2 \\ \delta\lambda_1 \\ \delta\lambda_1 \\ \vdots \\ \delta\Sigma \end{bmatrix} = \begin{bmatrix} M_{meas,1}\left[\Phi_1 - z_1\right] + A_1^T\lambda_1 \\ M_{meas,2}\left[\Phi_2 - z_2\right] + A_2^T\lambda_2 \\ A_1\Phi_1 - F_1 \\ A_2\Phi_2 - F_2 \\ \vdots \\ \sum_{i=1}^{I} \lambda_i\partial_\Sigma A\Phi_i \end{bmatrix} \tag{3.50}$$

3. Schur Complement Modification

Every time another experiment is considered, another flux and adjoint correpsonding to that experiment will provide additional matrix equations in the Schur Complement. This final equation for $\delta\Sigma$ can be simplified and expressed as:

$$\delta\Sigma = \left[\sum_{i=1}^{I} S_i\right]^{-1} \cdot \left[\sum_{i=1}^{I} U_i\right] \tag{3.51}$$

where S_i is the Schur complement and U_i is the corresponding right hand side from Equations 3.37-3.39.

G. Multigroup Analysis

The final modifications to the code account for multiple energy groups of neutrons. This multi-group code will allow reconstruction of multigroup cross sections. This model includes reconstruction of fission cross sections, fission spectrum, group removal cross section, and intergroup scattering cross sections. The optimality conditions are again derived including first derivatives and the Hessian involving the second derivatives taken with respect to each of the new variables. It is supposed that this

model would enable greater acquisitions of realistic data that can be used to detect materials inside these multiple optical thickness thick objects.

Multigroup diffusion theory has more meaningful application to the problem at hand. The incident neutron beams can be classified due to their energy and with material constants for uranium, or other fissile material, such as χ_g, the fission cross sections for each group can be reconstructed to determine if fissile material is present in the cargo container. One example of a test case would be if the incident neutrons were only in the slow energy groups, but neutrons in fast energy groups were detected. Due to the nature that neutrons only have a reasonable probability to upscatter in the thermal Maxwellian range, those neutrons must have been born in the domain. That would be a greater chance of determination of SNM.

1. Multigroup Diffusion Theory

In neutron diffusion theory, neutrons can be classified by their energy and broken into groups. Due to scattering and fission, neutrons are able to be redistributed in energy based on the magnitude of their cross sections and fission spectrum, χ_g. In neutron diffusion theory equations of each group of neutrons can be formed with scattering terms that represent timerate densities of group to group scattering events.

$$-\nabla \cdot D_g \nabla \Phi_g + \Sigma_{r,g}\Phi = \chi_g \sum_{g'=1}^{G} \nu\Sigma_{f,g'}\Phi_{g'} + \sum_{g'=1, g\neq g'}^{G} \Sigma_{s,g'\to g}\Phi_{g'} \tag{3.52}$$

Where $\Sigma_{r,g} = \Sigma_{a,g} + \sum_{g'=1, g\neq g'}^{G} \Sigma_{s,g\to g'}\Phi_g$ or removal from the group g due to absorption and outscatter. An example, the 2 group diffusion operator is given below:

$$A = \begin{bmatrix} -\nabla \cdot D_1 \nabla + \Sigma_{r,1} - \chi_1 \nu\Sigma_{f,1} & -\Sigma_{s,2\to 1} - \chi_1 \nu\Sigma_{f,2} \\ -\Sigma_{s,1\to 2} - \chi_2 \nu\Sigma_{f,1} & -\nabla \cdot D_2 \nabla + \Sigma_{r,2} - \chi_2 \nu\Sigma_{f,2} \end{bmatrix} \tag{3.53}$$

Everything remains unchanged for the optimization problem, except there are more parameters (Φ_g, λ_g, and Σ_g) for multiple energy groups creating the same $A\Phi = F$ system. The diffusion operator is no longer symmetric, $A^T \neq A$, because of scattering and fission.

2. Cross-Section Data for Various Materials

To gain a greater understanding of the reconstruction length-scale with respect to different materials, macroscopic cross sections for various materials are computed at fission spectrum average and 14 MeV energies. Using these cross sections, diffusion coefficients and diffusion lengths can be compared for different materials that may be present in a container. The macroscopic cross sections for various materials can be seen in Tables III-I - III-II[14].[15]

The steel composition used consisted of: 65.8% iron, 20.5% aluminum, 13.6% chromium, and 0.03% carbon. If fissile material were present, it may be shielded with a strong absorbing material such as borated polyethylene. Enriched boron is assumed in these computations at 90% B-10 and assuming uranium enriched to 80% U-235. The thermal, fission spectrum average, and 14.0 MeV macroscopic cross sections are computed and shown in Tables III-III - III-V[14].[15]

Table III-I. Cross-section data for various materials at 14.0 MeV

Material	Composition	Density [g/cc]	Σ_t [cm^{-1}]	Σ_s [cm^{-1}]	Σ_a [cm^{-1}]	D [cm]	L [cm]
Wood	CH_2O	0.5	0.0431	0.0403	0.0027	7.7299	52.6855
Fresh Wood	$(CH_2O)_{0.85} + (H_2O)_{0.15}$	0.575	0.0516	0.0482	0.0033	6.4505	43.5922
Plastic	C_2H_3Cl	1.39	0.0898	0.0766	0.0132	3.7094	16.7477
Steel	(see text)	7.85	0.2246	0.1618	0.0628	1.4834	4.8588
Aluminum	Al	2.7	0.1036	0.0742	0.0294	3.2159	10.4564

Table III-II. Cross-section data for various materials at fission spectrum average

Material	Composition	Density [g/cc]	Σ_t [cm^{-1}]	Σ_s [cm^{-1}]	Σ_a [cm^{-1}]	D [cm]	L [cm]
Wood	CH_2O	0.5	0.0821	0.0821	1.404E-05	4.0576	537.4704
Fresh Wood	$(CH_2O)_{0.85} + (H_2O)_{0.15}$	0.575	0.0990	0.0990	1.1939E-05	3.3659	530.9608
Plastic	C_2H_3Cl	1.39	0.1973	0.1973	3.7514E-05	1.6890	212.1866
Steel	(see below)	7.85	0.2643	0.2627	0.0015	1.2610	28.2883
Aluminum	Al	2.7	0.1963	0.19283	0.0035	1.6972	21.8490

Table III-III. Cross-section data for HEU in borated polyethylene at 14.0 MeV

Material	Composition	Density [g/cc]	Σ_t [cm^{-1}]	Σ_a [cm^{-1}]	Σ_f [cm^{-1}]	D [cm]	L [cm]
Polyethylene	CH_2	0.94	0.1085	0.0029	0.0	3.0715	32.3299
Borated Polyethylene	$(CH_2)_{0.95} + (B)_{0.05}$	0.978	0.1119	0.0042	0.0	2.9774	26.3211
HEU	U	19.0	0.3679	0.1318	0.0503	0.9058	2.6206
50/50 B.Poly./HEU	-	10.014	0.2399	0.0680	0.0251	1.3891	4.5165
90/10 B.Poly./HEU	-	2.785	0.1375	0.0170	0.0050	2.4232	11.9190

Table III-IV. Cross-section data for HEU in borated polyethylene at fission spectrum average

Material	Composition	Density [g/cc]	Σ_t [cm^{-1}]	Σ_a [cm^{-1}]	Σ_f [cm^{-1}]	D [cm]	L [cm]
Polyethylene	CH_2	0.94	0.2974	0.0060	0.0	1.1206	13.6610
Borated Polyethylene	$(CH_2)_{0.95} + (B)_{0.05}$	0.978	0.2984	0.0028	0.0	1.1169	19.8869
HEU	U	19.0	0.3843	0.1979	0.0448	0.8673	2.0933
50/50 B.Poly./HEU	-	10.014	0.3413	0.1003	0.0224	0.9764	3.1190
90/10 B.Poly./HEU	-	2.7852	0.3070	0.0223	0.0044	1.0856	6.9722

Table III-V. Cross-section data for HEU in borated polyethylene at thermal energy

Material	Composition	Density [g/cc]	Σ_t [cm^{-1}]	Σ_a [cm^{-1}]	Σ_f [cm^{-1}]	D [cm]	L [cm]
Polyethylene	CH_2	0.94	1.8719	0.0324	0.0	0.1780	2.3416
Borated Polyethylene	$(CH_2)_{0.95} + (B)_{0.05}$	0.978	22.7187	20.9564	0.0	0.0146	0.0264
HEU	U	19.0	24.1287	23.5404	20.0570	0.0138	0.0242
50/50 B.Poly./HEU	-	10.014	23.4237	22.2484	10.0285	0.01423	0.0252
90/10 B.Poly./HEU	-	2.7852	22.8597	21.2148	2.0057	0.0145	0.0262

CHAPTER IV

RESULTS

Several examples are presented to demonstrate the reconstruction limits with respect to different problem variables. The first example shows the importance of source and measurement location for imaging problems (Section A. The second example is a simple reconstruction of a homogeneous domain comparing convergence between the steepest descent and Newton's methods. Reconstructions with position dependence are presented next in (Section C), while the examples 4-5 (D) provides two cases displaying the effects on reconstruction resolution while increasing the number of experiments to demonstrate maximum reconstruction resolution. The example 6 shows the effects on reconstruction ability when the domain size is increased, which is tested using 8 and 32 experiments, to show the maximum reconstruction depth into a domain. Examples 7-11 include the addition of signal noise and signal bias to the synthetic measured solutions to better simulate actual detectors and the effect on reconstruction ability. Multigroup models are then shown, in examples 12-18, including various combinations of reconstructing multiple parameters (Σ_a and $\nu\Sigma_f$) in different energy groups.

There are three basic geometries that are used in the presented reconstruction examples. The first is a homogeneous domain which is used for basic reconstruction testing and misfit plotting in multigroup. The second consists of bars of various materials side by side. This simulates a piecewise constant one dimensional problem spread over a second dimension. The third is a centered strong absorber hidden in the center of a homogeneous domain, which is the typical material hidden inside another material example and is ideal for testing as the center of a domain typically has the

most error in reconstruction.

A. Example 1: Misfit Plots

Consider a domain divided into two side-by-side homogeneous regions for which the cross section in each is to be reconstructed. An example of a such region is shown in Figure IV-1. This is a case of a two-parameter problem and a misfit surface plot can be graphed where the x-axis represents the inferred cross-section value in region 1, the y-axis represents the inferred cross-section value in region 2, and the z-axis represents the misfit as a function of the cross sections in the two regions. This graph will help understand the influence of the incoming source illumination on the ability to reconstruct one or both of the cross sections in this domain.

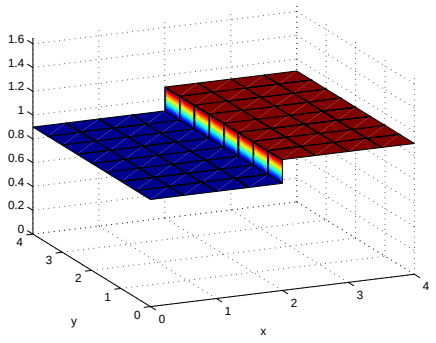

Region	D	Σ_a	$\nu\Sigma_f$
1	0.25	0.9	0.0
2	0.25	1.1	0.0

Fig. IV-1. Two-region domain of Example 1

The ability to reconstruct an internal parameter strongly depends on the illuminating source and measurement location. In this example measurements are taken on all sides and the source location is moved, similar results arise when the reverse case is considered. Two misfit surface plots were constructed using only one incident beam of neutrons on the side of one of the regions as shown in Figure IV-2 (cases a.) and b.)).

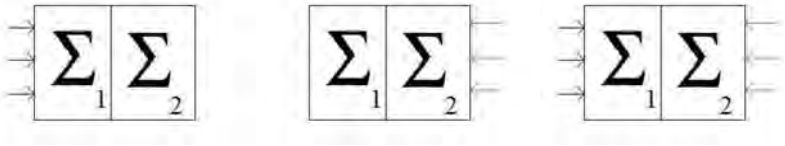

(a) Case a.) left incidence (b) Case b.) right incidence (c) Case c.) both beams present

Fig. IV-2. Ex. 1: Various cases of beam incidence

It can be noted in Figure IV-3, an elongated valley is produced for the misfit in the direction of the cross section whose side was not upon incident neutrons. This means that the cross section in this region can vary greatly while the misfit remains unchanged, illustrating the ill-posedness of the inverse problem.

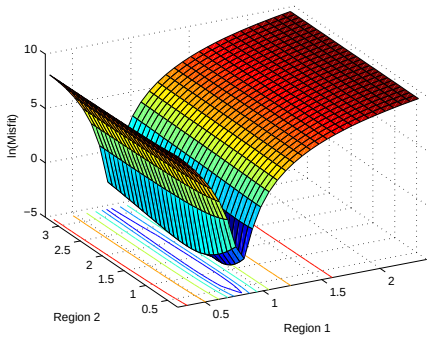

Fig. IV-3. Ex. 1: Misfit plot for case a.)

If the only incident neutron beam was moved to the side of the other region, an elongated valley is produced in the direction of the opposite cross section again as shown in Figure IV-4. Similarly in this case, the cross section in the rgion with no incoming neutron flux can vary greatly with respect to the other without significantly changing the true flux solution at the measurement points.

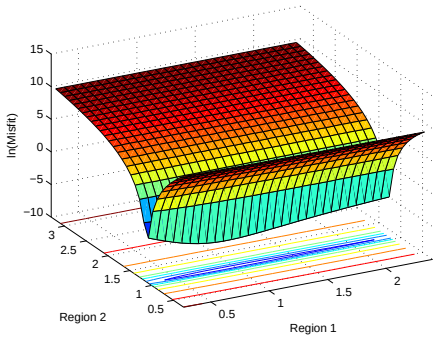

Fig. IV-4. Ex. 1: Misfit plot for case b.)

When both beams are on, one from each region side (case c.), a much smoother cone shape surface is produced as shown in Figure IV-5. It will be significantly easier to determine the cross section for both regions in this setting.

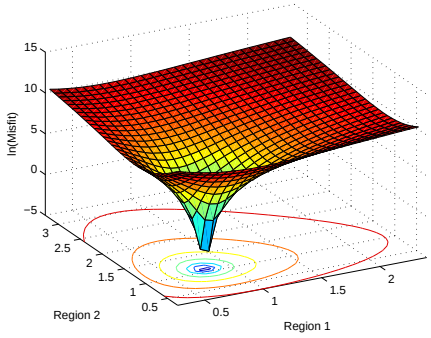

Fig. IV-5. Ex. 1: Misfit plot for case c.)

Having described and analyzed a 2-parameter case, the next models will include a fully position-dependent cross section. The information acquired here can be applied to the next model but cannot be shown visually. The model will have to find the minimum misfit of a multi-dimensional function so the incoming beams and measurements play a critical role in determining a solution and the ability to find this solution.

B. Example 2: Comparison of Convergence Between Steepest Descent Method and Newton's Method for a Homogeneous Problem

To show the decrease in misfit and Lagrangian as a function of iteration count, the optimization problem is run where these are stored for an example using a homogeneous domain consisting of: $D = 1$, $\Sigma_a = 0.3$ and $\nu\Sigma_f = 0$. This domain is of size 6 cm $\times$ 6 cm. These are simply stored then plotted after convergence, for this simple homogeneous problem starting relatively close ($\Sigma_a = 0.2$) to the true solution the misfit and Lagrangian are shown in Figure IV-6.

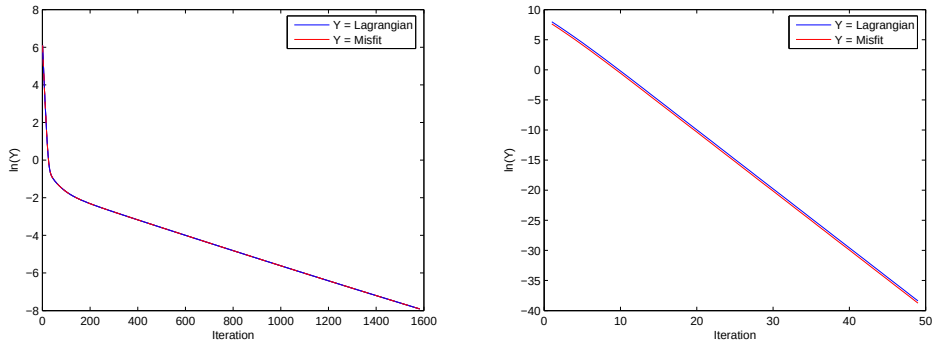

(a) Steepest Descent (b) Newton

Fig. IV-6. Ex. 2: Convergence of misfit and Lagrangian for steepest descent and Newton's methods

As expected, these are both reduced and the reduction as a function of iteration count is exponential. Table IV-I shows a comparison of convergence statistics for this homogeneous domain. As expected, Newton's method outperforms the steepest descent method.

Table IV-I. Ex. 2: Convergence comparison between two line search methods

Method	Steepest Descent	Newton's
Time [s]	424.9	49.5
Iterations	1583	50
Order of $\mathcal{L}$	10^{-4}	10^{-17}

To better show convergence using Newton's method, a one-group problem consisting of a homogeneous domain is considered that contains two strong absorbers present inside and the cross section plotted at several steps during convergence. The initial guess for the domains cross section is a constant $\Sigma_a = 0.2$ where the true cross sections are $\Sigma_a = 0.3$ for the surrounding domain and $\Sigma_a = 0.5$ for the strong absorbers. An example of this problems convergence is shown in Figure IV-7 where each step represents approximately 10 iterations.

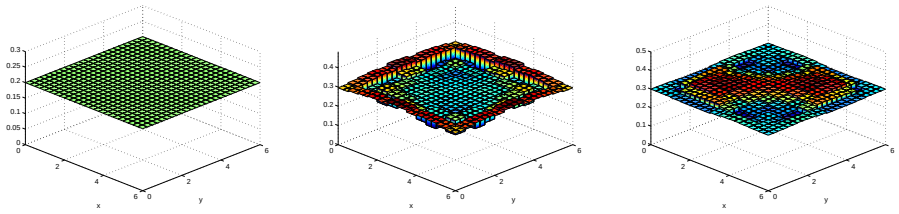

(a) Initial Guess (b) Step 2 (c) Step 3

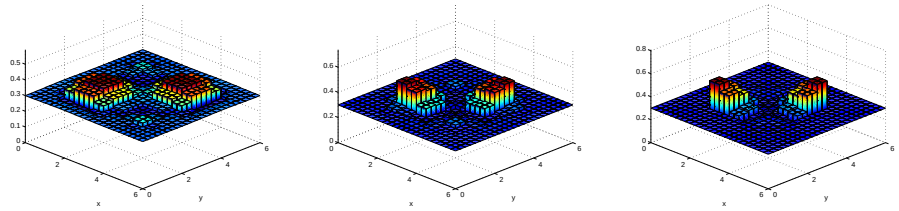

(d) Step 4 (e) Step 5 (f) Step 6

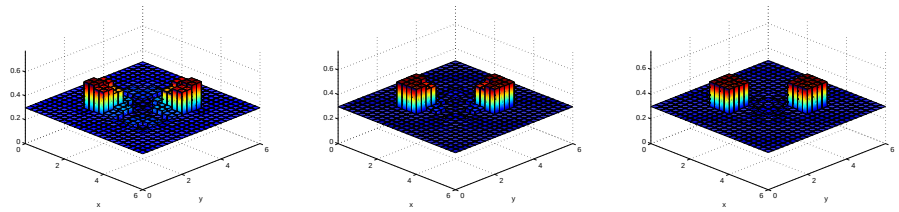

(g) Step 7 (h) Step 8 (i) Converged

Fig. IV-7. Example 2: Convergence of dual strong absorbers in a homogenous domain

C. Example 3: Multiple Region Single Experiment Results

To reconstruct internal features of more complex domains, reconstructions are performed using using a mesh. The number of regions is determined using a coarse mesh based on the finer mesh used for the flux solver. This flux mesh (fine) consists of a variable refinement but a mesh of 2×2 finer than the material (coarse) mesh is often used. This enabled many various domains of varying cross section to be reconstructed at a user defined resolution.

The domain tested in this case was an 8×8 diffusion length domain consisting

of four vertical stripes of different materials which properties shown in Table IV-II. The true cross section of this domain is shown in Figure IV-8.

Table IV-II. Ex. 3: Cross-section data

Region	D	Σ_a	Σ_f
1	0.25	0.9	0.0
2	0.25	1.0	0.0
3	0.25	1.1	0.0
4	0.25	0.9	0.0

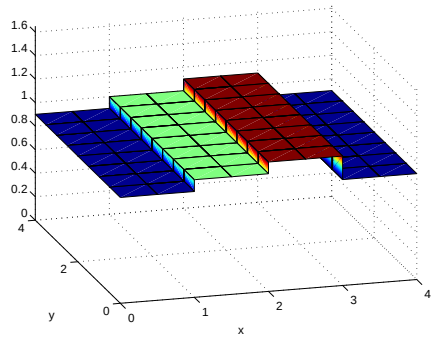

Fig. IV-8. Ex. 3: True cross section with position dependence

The coarse mesh here was setup as 8 by 8 in x and y directions respectively creating 64 regions with cross sections to be reconstructed. There was a refinement of 2 in both directions for the flux solver. This model converged after 8 Newton iterations with a misfit of 3.616e-15 and the optimality conditions were driven down to 1.06285e-11 in 1.47 seconds. The reconstructed flux and cross section can be shown in Figure IV-9.

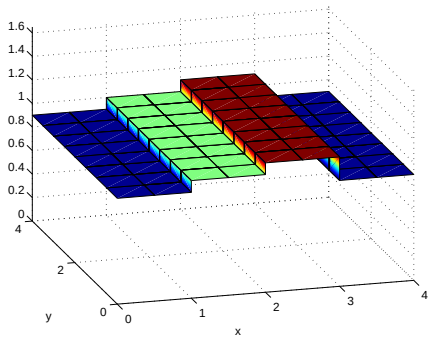

Fig. IV-9. Ex. 3: Reconstructed cross section with position dependence

To graphically show the precision of the reconstruction the difference between the true solution and reconstruction was taken and shown in Figure IV-10.

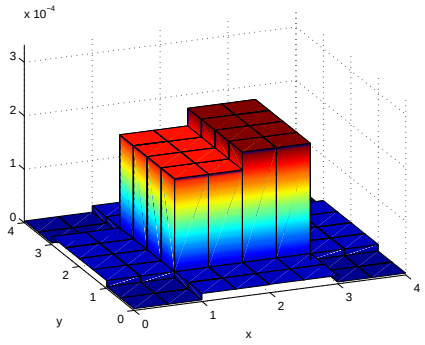

Fig. IV-10. Ex. 3: Error in cross section reconstruction with position dependence

This reconstructed solution agreed with the measured solution well as the error was on the order of 10^{-4}.

D. Multiple Experiment Results

When the incoming currents were split across the domain creating separate experiments, each with separate flux and adjoint solutions, the same set of cross sections for

the domain are reconstructed. This created more constraints on the data resulting in greater reconstruction ability.

1. Example 4: Reconstruction Resolution Testing with Increasing Number of Experiments on a 4 cm × 4 cm Domain

The first example case shows the correlation between reconstruction resolution and the number of experiments on a domain consisting of a strong centered absorber. This domain consisted of $\Sigma_a = 1.3$, $\nu\Sigma_f = 0$ and $D = 0.3$ in the center region and $\Sigma_a = 0.9$, $\nu\Sigma_f = 0$ and $D = 0.3$ in the outer region. Three cases are considered for this example all of the same domain and mesh size, the first consisting of one experiment having a beam on a single side of the domain. The second case still consists of a single experiment but a beam on all four sides of the domain. The third case consists of eight experiments, each covering one half of each side. Measurements are made on all four sides every time. These cases reconstructions are shown in Figure IV-11 and corresponding errors in Figure IV-12.

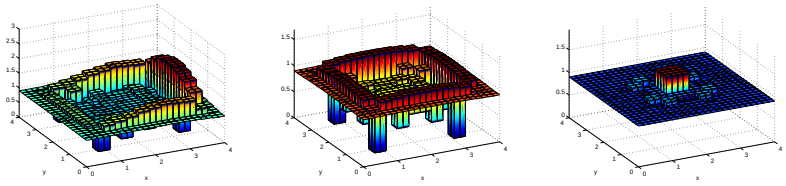

(a) 1 Exp. 1 Beam (left) (b) 1 Exp. 4 Beams (1 beam per side) (c) 8 Experiments (each beam covering half a side

Fig. IV-11. Ex. 4: Effects on reconstruction resolution while increasing the number of experiments on a 4 cm × 4 cm domain

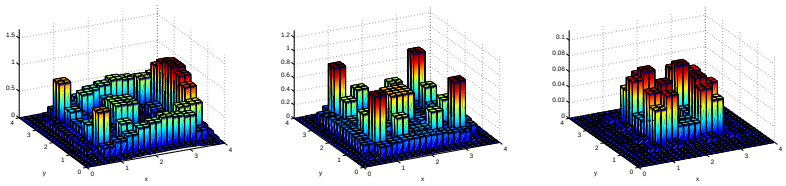

(a) 1 Exp. 1 Beam (left) (b) 1 Exp. 4 Beams (1 beam per side) (c) 8 Experiments (each beam covering half a side)

Fig. IV-12. Ex. 4: Error in reconstructions resolution testing while increasing the number of experiments on a 4 cm $\times$ 4 cm domain

This shows that increasing the number of experiments directly improves the maximum reconstruction resolution, enabling previously unsuccessful cases to have successful reconstructions. While this may be misleading, every problem has its resolution limits independent of the number of experiments. When reconstruction limits are approached, often additional experiments consist of too much noise to add any additional resolution refinement.

2. Example 5: Reconstruction Resolution Testing with Increasing Number of Experiments on a 10 cm $\times$ 10 cm Domain

The next test example examines the effects of multiple experiments on reconstruction resolution for a larger domain. The same example problem of the centered strong absorber was considered here and reconstructions performed with 1, 8, and 32 experiments on a approximately 10 cm by 10 cm domain. With only 1 experiment consisting of beams on all four sides of the domain, Figure IV-13 shows the associated reconstruction with significant error and almost no recognizable features of the true solution.

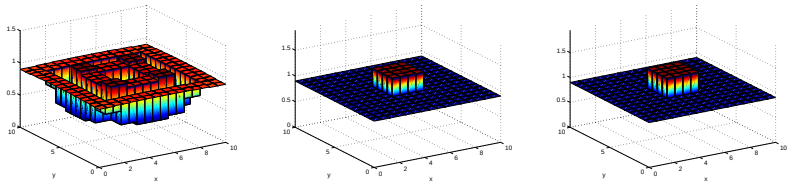

(a) 1 Experiment (1 beam per side) (b) 8 Experiments (each beam covering half a side) (c) 32 Experiments (each beam covering $\frac{1}{8}$th of a side)

Fig. IV-13. Ex. 5: Reconstruction resolution testing of centered strong absorber in a 10 cm $\times$ 10 cm domain

When the number of experiments was set to eight, each covering one eighth of the domain or two per side this resulted in a better reconstruction where the error at the center is on the order of 10^{-2}. When the number of experiments was set to 32, each covering $\frac{1}{32}$ of the domain or eight per side this resulted in a much better reconstruction where the error at the center is on the order of 10^{-3} shown in Figure IV-14.

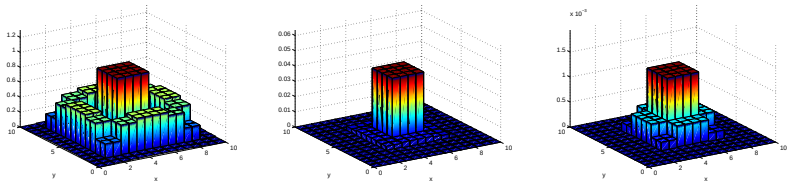

(a) 1 Exp. Error (1 beam per side) (b) 8 Exp. Error (each beam covering half a side) (c) 32 Exp. Error (each beam covering $\frac{1}{8}$th of a side)

Fig. IV-14. Ex. 5: Error in reconstructions for resolution testing of centered strong absorber in 10 cm $\times$ 10 cm domain

3. Example 6: Effects on Reconstruction When the Domain Size is Increased Using 8 and 32 Experiments

Another example problem, with the number of experiments held constant at eight, shows the effects of increased domain size on reconstruction ability. In this example, with the mesh size is held constant along with the number of experiments, the size of the domain is increased and the effects on reconstruction ability was observed. Three different sizes are used here approximately 8×8, 12×12, and 16×16 characteristic lengths. The reconstructions are shown in Figure IV-15 and the corresponding reconstruction error in Figure IV-16.

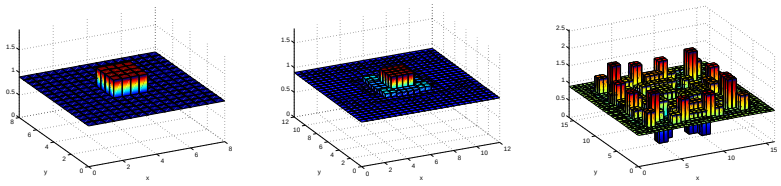

(a) 8 x 8 (b) 12 x 12 (c) 16 x 16

Fig. IV-15. Ex. 6: Effects on reconstructions when domain size is increased using eight experiments

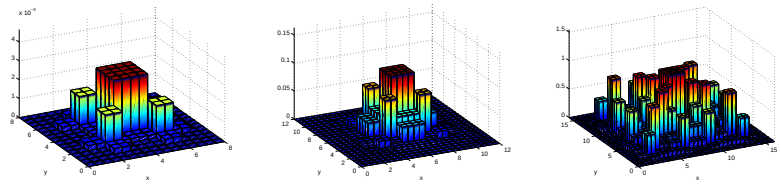

(a) 8 x 8 Error (b) 12 x 12 Error (c) 16 x 16 Error

Fig. IV-16. Ex. 6: Error in reconstructions when domain size is increased using eight experiments

Using eight experiments, the it is only possible to reconstruct approximately

6-7 characteristic lengths deep into an object. As the domain size approached 16 characteristic lengths wide ($L = 1.054$cm in this example), there was too much signal degradation to reconstruct any domain characteristics. These same cases were run with 32 experiments, and the changes in reconstruction are shown below in Figure IV-17 and error Figure IV-18.

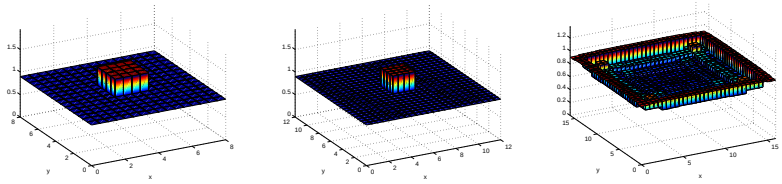

(a) 8 x 8 (b) 12 x 12 (c) 16 x 16

Fig. IV-17. Ex. 6: Effects on reconstructions when domain size is increased using 32 experiments

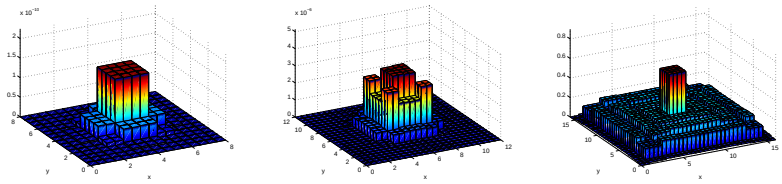

(a) 8 x 8 Error (b) 12 x 12 Error (c) 16 x 16 Error

Fig. IV-18. Ex. 6: Error in reconstructions when domain size is increased using 32 experiments

The implementation of 32 experiments shows improvement for the 12×12 case, while the 16×16 case showed no improvement. This proves that the addition of multiple experiments does provide additional reconstruction power, but reconstruction depth has severe limits independent of the number of experiments.

4. Example 7: Dual Strong Absorbers Embedded in a Large Highly Scattering Domain

The next domain reconstructed consisted of a large and highly scattering domain that contains two embedded identical strong absorbers. This domain size is over the previously mentioned maximum reconstruction size, but contains a very low absorption cross section. The domain parameters for the two regions are shown in Table IV-III.

Table IV-III. Ex. 7: Cross-section data for dual strong absorbers embedded in a large highly scattering domain

Region	D	Σ_a	Σ_s
Absorbers	0.016	21.37	0.012
Domain	0.467	0.0005	0.713

The domain is 10 cm $\times$ 10 cm where the outer region resembles carbon properties, while the absorbers embedded inside it resemble boron properties. The absorption cross section is reconstructed for this domain with an initial guess of a constant $0.008 cm^{-1}$. This reconstruction is performed using eight experiments on a coarse mesh of 10 $\times$ 10 with a refinement of 2 in both dimensions whose true and reconstructed cross sections are shown in Figure IV-19.

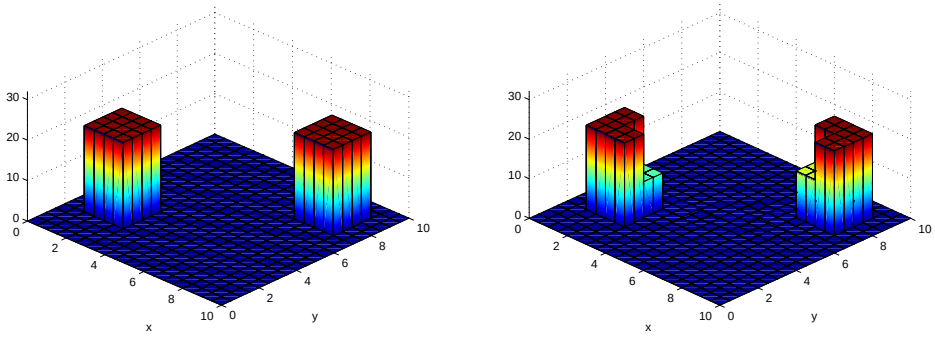

(a) True Cross Section (b) Reconstruction

Fig. IV-19. Ex. 7: Reconstruction of two strong absorbers in a large highly scattering domain

While this reconstruction may look very accurate, the magnitude of the parameters hides the reconstruction error. To better show this effect, the absolute error along with the relative error are shown in Figure IV-20.

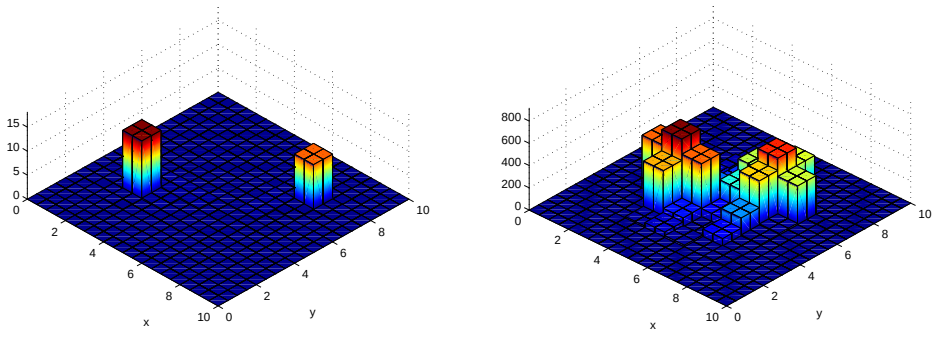

(a) Absolute Error (b) Relative Error

Fig. IV-20. Ex. 7: Error in reconstruction of two strong absorbers in a large highly scattering domain

From the absolute error only, this reconstruction appears to be of excellent quality, but the relative error shows the cross sections in the center regions contain great

variance from the true solutions.

E. Addition of Signal Noise and Bias

To better simulate an actual boundary detector, signal noise and bias have been implemented into the synthetic measured solutions to simulate an actual radiation detector. The addition of noise results in a perturbation of the the synthetic measured solutions z, by a specified percentage using random numbers. The application of a bias would be similar but just averaged in a certain direction either positive or negative as opposed to zero. High accuracy boundary fluxes, or measured solutions, are crucial to achieve quality reconstructions, so as noise and bias are increased, it is expected that reconstruction ability will diminish. This amount of noise was varied and the effect on reconstruction observed.

While there are several ways to implement signal bias and noise, a constant noise distribution and a percentage based bias are used here shown in Equations 4.1-4.2.

$$z_{i,\text{noise}} = z_i(1 + \beta\epsilon_i) \tag{4.1}$$

$$z_{i,\text{biased noise}} = z_i(1 + \delta + \beta\epsilon_i) \tag{4.2}$$

In Equation 4.1, z_i is the clean synthetic measured solution, β is the magnitude of the noise and $\epsilon_i \in (-1, 1)$ is the random number for measurement location i. In Equation 4.2, the same variable magnitude of noise is present but the addition of a flat percentage bias, $\delta \in (-1, 1)$, is added. The magnitude of δ is constant for all measurement points.

1. Addition of Random Signal Noise

a. Example 8: Signal noise added on a homogenous domain

The optimal initial benchmark case would be one who's noiseless reconstruction ability is very high. The problem selected is a 4 cm × 4 cm homogeneous domain broken into 16 regions to reconstruct. This domain has the following properties: $\Sigma_a = 0.3$, $D = 1$, and $\nu\Sigma_f = 0$. All of the signal noise examples are reconstructed using eight experiments as this quantity of experiments is sufficient for noiseless reconstructions in all of the problems used. Three quantities of noise are applied to this domain of magnitudes of 0.01%, 0.1%, and 1.0% and reconstruction results shown in Figure IV-21.

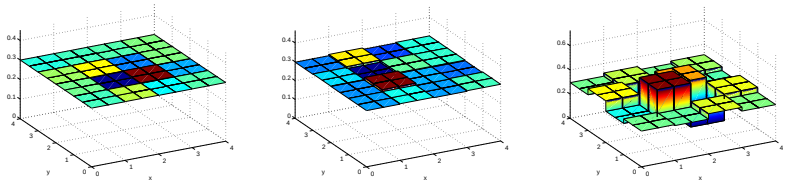

(a) 0.01% Signal Noise (b) 0.1% Signal Noise (c) 1.0% Signal Noise

Fig. IV-21. Ex. 8: Reconstruction with signal noise of a homogeneous domain

The case of β =0.0% noise is not shown due to the high reconstruction ability of the β =0.01% case it is obvious what the true cross-section solution is. With β =0.01% and β =0.1% noise reconstruction ability is still high but as the noise magnitude approaches 1.0%, even this simple homogenous domain becomes almost indistinguishable. The resulting reconstruction errors are shown in Figure IV-22.

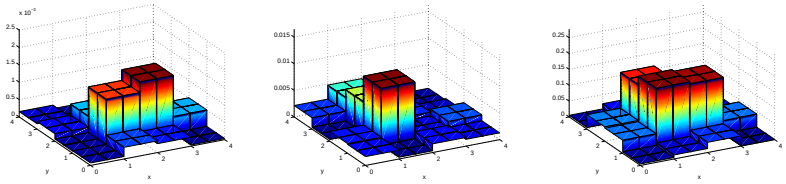

(a) 0.01% Signal Noise Error (b) 0.1% Signal Noise Error (c) 1.0% Signal Noise Error

Fig. IV-22. Ex. 8: Error in reconstruction with signal noise of a homogeneous domain

b. Example 9: Signal noise added to bars of various materials

The next problem implemented with signal noise is similar to Ex. 3 (Section C) which had high reconstruction ability and consisted of bars of various materials whose material properties are shown in Table IV-IV.

Table IV-IV. Ex. 9: Cross-section data for bars of various material

Region	D	Σ_a	Σ_f
1	1.0	0.3	0.0
2	1.0	0.5	0.0
3	1.0	0.7	0.0
4	1.0	0.3	0.0

This domain size is approximately 4 × 4 characteristic lengths thick and is reconstructed using eight experiments. Due to the noiseless high reconstruction ability of this example, the same 0.01%, 0.1% and 1.0% quantities of signal noise are added and reconstructions shown in Figure IV-23.

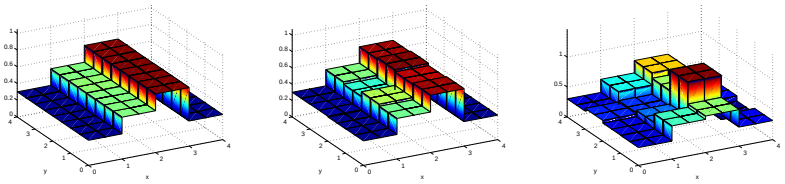

(a) 0.01% Signal Noise (b) 0.1% Signal Noise (c) 1.0% Signal Noise

Fig. IV-23. Ex. 9: Reconstruction with signal noise of multiple materials

Just as in the case of the homogeneous domain, the 0.01% and 0.1% signal noise examples still provided quality reconstructions while features of the domain start to diminish in the center at 1.0% signal noise as shown in the resulting reconstruction error in Figure IV-24.

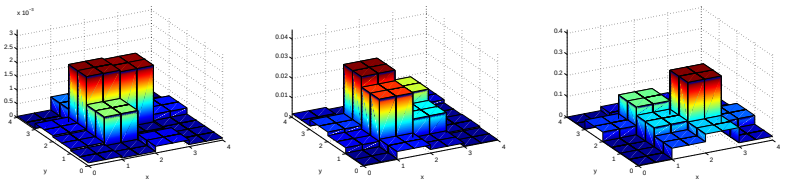

(a) 0.01% Signal Noise Error (b) 0.1% Signal Noise Error (c) 1.0% Signal Noise Error

Fig. IV-24. Ex. 9: Error in reconstruction with signal noise of multiple materials

c. Example 10: Reconstruction testing with signal noise on a centered strong absorber inside various size domains

The final example implemented with signal noise was the previously defined centered strong absorber. This was tested at multiple noise magnitudes along with multiple domain sizes in three cases approaching the maximum reconstruction size. This domain consists of a strong absorbing center region surrounded by a weaker absorbing domain. The center region has the following material properties $\Sigma_a = 0.6$, $\nu\Sigma_f = 0$,

and $D = 1.0$, while the surrounding domain has $\Sigma_a = 0.3$, $\nu\Sigma_f = 0$, and $D = 1.0$. Three domain sizes are used here and reconstructions of the 4 cm $\times$ 4 cm ($L \approx 1$) domain are shown in Figure IV-25. In this example, due to the domains small size, reconstruction ability is high in the noiseless case so noise magnitudes of 0.01%, 0.1% and 1.0% are applied.

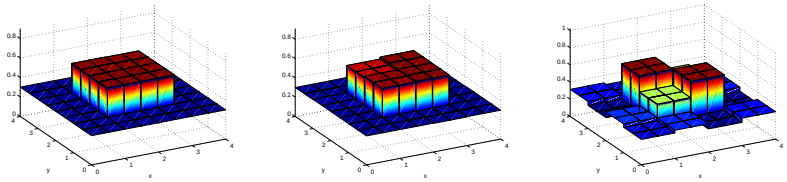

(a) 0.01% Signal Noise Error (b) 0.1% Signal Noise Error (c) 1.0% Signal Noise Error

Fig. IV-25. Ex. 10 Case 1: Reconstruction with signal noise of a centered strong absorber 4x4cm

As in the previous cases of similar domain size, the reconstruction ability diminished when the noise reaches 1.0% and reconstruction erros are shown in Figure IV-26.

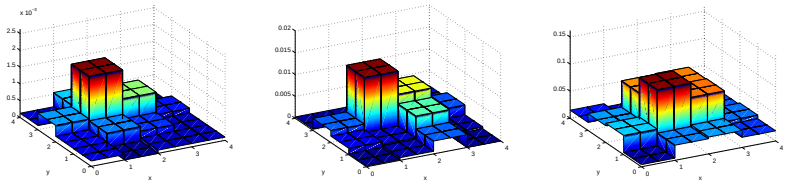

(a) 0.01% Signal Noise Error (b) 0.1% Signal Noise Error (c) 1.0% Signal Noise Error

Fig. IV-26. Ex. 10 Case 1: Error in reconstruction with signal noise of a centered strong absorber 4x4cm

The next case holds reconstruction resolution and material properties the same as the previous case of the centered absorber except the domain size is increased to 8

cm × 8 cm ($L \approx 1$). The material properties of both regions are the same as the 4 × 4 case. Two magnitudes of signal noise are applied in this case of 0.01% and 0.05% and reconstruction results are shown in Figure IV-27 along with the noiseless case.

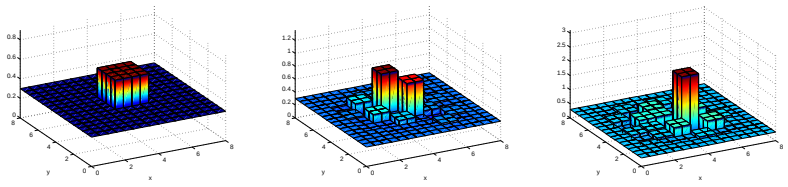

(a) 0.0% Signal Noise Error (b) 0.01% Signal Noise Error (c) 0.05% Signal Noise Error

Fig. IV-27. Ex. 10 Case 2: Reconstruction with signal noise of a centered strong absorber 8x8cm

In the 0.01% signal noise case for this size domain, the model shows reasonably that there is a stronger absorber in the center. While the size of this absorber is incorrect and slightly smeared throught the center, the magnitude is a good approximation. In the 0.05% signal noise case, the entire centered absorber is smeared across the middle including one region whos magnitude is too high by a factor of 3.5. The error in this case is too high to consider this a successful reconstruction, as the features are hardly distinguishable. Thes reconstruction errors are shown in Figure IV-28.

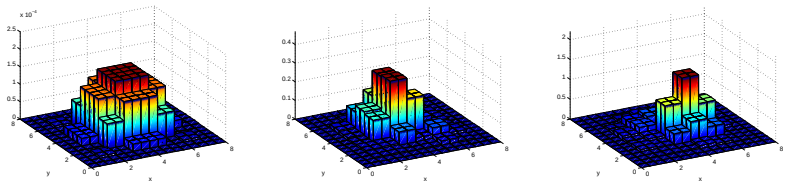

(a) 0.0% Signal Noise Error (b) 0.01% Signal Noise Error (c) 0.05% Signal Noise Error

Fig. IV-28. Ex. 10 Case 2: Error in reconstruction with signal noise of a centered strong absorber 8x8cm

The third case was a domain of 12 cm× 12 cm in size ($L \approx 1$). This is close to the domain size reconstruction limit with no signal noise so reconstructions with any signal noise are expected to be poor. The same material properties of the 4 × 4 and 8 × 8 case are used. Two magnitudes of signal noise are applied in this case of 0.0005% and 0.005% and reconstruction results are shown in Figure IV-29 along with the noiseless case.

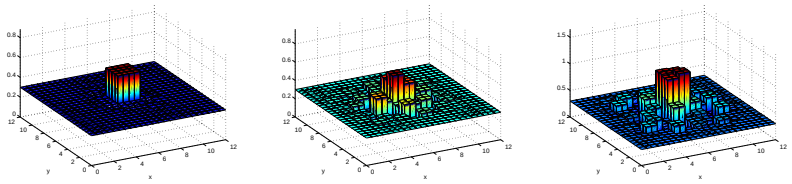

(a) 0.0% Noise (b) 0.0005% Noise (c) 0.005% Noise

Fig. IV-29. Ex. 10 Case 3: Reconstruction with signal noise of a centered strong absorber 12x12cm

This case already had limited reconstruction ability with 0.0% noise, therefore the addition of signal noise is expected to cause poor reconstructions. This case began to lose distinguishable features as error increased over 0.005% and resulting reconstruction error is shown in Figure IV-30.

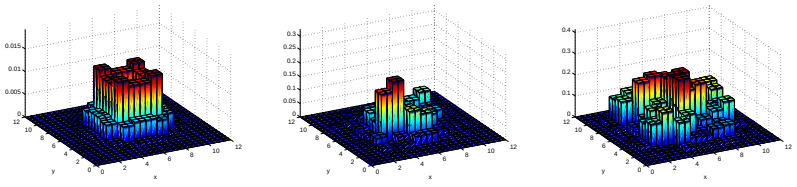

(a) 0.0% Noise Error (b) 0.0005% Noise Error (c) 0.005% Noise Error

Fig. IV-30. Ex. 10 Case 3: Error in reconstruction with signal noise of a centered strong absorber 12x12cm

2. Addition of Signal Bias

The next example was implemented with signal bias was the previously defined centered strong absorber. This was tested at multiple noise strengths along with domain sizes up to approximately the maximum reconstruction size. One of the same domains tested with signal noise is chosen here and two problems tested with a bias with additional signal strength and attenuated signal strength. In these cases a signal bias is added of a specified magnitude, then random noise added of another magnitude to simulate an actual signal bias with variable variance and magnitude.

a. Example 11: Reconstructing with a positive signal bias of a centered strong absorber

In the first case a positive signal bias of various magnitudes was added to the synthetic measured solutions then random signal noise of a 0.1% applied, and an attempt at reconstructions performed. The test domain was the 4×4 characteristic length centered strong absorber. This domain's properties consist of $\Sigma_a = 0.6$, $\Sigma_f = 0$, and $D = 1.0$ in the center and $\Sigma_a = 0.3$, $\Sigma_f = 0$, and $D = 1$ in the surrounding area. The positive bias is applied in two magnitudes of 1.0% and 5.0% and resulting reconstructions shown in Figure IV-31 including the 0.0% bias 0.1% noise case is shown for comparison.

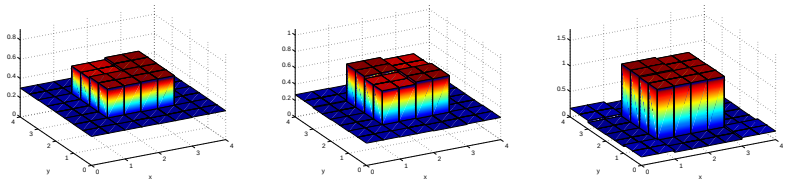

(a) 0.0% Signal Bias (b) 1.0% Signal Bias (c) 5.0% Signal Bias

Fig. IV-31. Ex. 11: Reconstruction with a positive signal bias of a centered strong absorber

When a signal bias of 1.0% is added to the synthetic measured solution, the measured solution is higher then expected leading to a cross section that provides less attenuation. In the region surrounding the center absorber, the cross section is smaller then the true value as expected however, in the center region the magnitude of the cross section is higher then the true cross section. This is mainly due to the fact that the signal bias is percentage based for each element not a flat bias throughout the measurements. When the signal bias is increased to 5.0%, the cross section in the surrounding region is again lowered, while the center region is again increased. These reconstruction errors are shown in Figure IV-32.

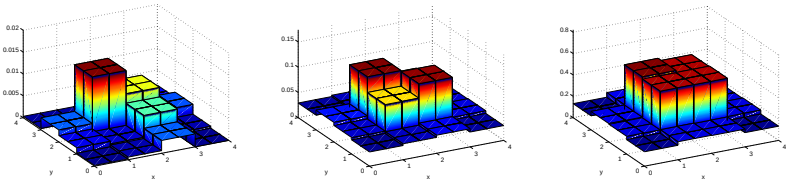

(a) 0.0% Bias Error (b) 1.0% Bias Error (c) 5.0% Bias Error

Fig. IV-32. Ex. 11: Error in reconstruction with a positive signal bias of a centered strong absorber

b. Example 12: Reconstructing with a negative signal bias on a centered strong absorber

The same test as the positive signal bias, but with a negative signal bias instead. The same domain is tested here with -1.0% and -5.0% bias with 0.1% random signal noise. The same material properties as the positive bias are used here and reconstructions are shown in Figure IV-33.

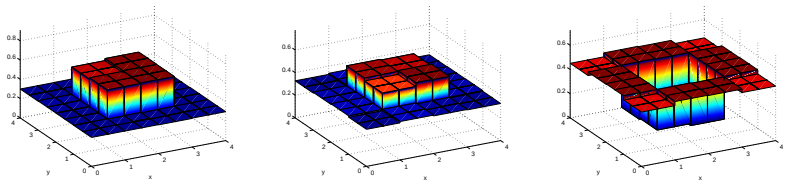

(a) 0.0% Signal Bias (b) -1.0% Signal Bias (c) -5.0% Signal Bias

Fig. IV-33. Ex. 12: Reconstruction with a negative signal bias of a centered strong absorber

When a -1.0% bias is applied to the synthetic measured solutions, an abundance of attenuation is expected leading to an increase in reconstructed cross section. This is true for the surrounding region, this bias over accounts the attenuation in the surrounding region leaving the center region's cross section lower then expected. The same effects are shown in the -5.0% case to a greater effect and the reconstruction errors are shown in Figure IV-34.

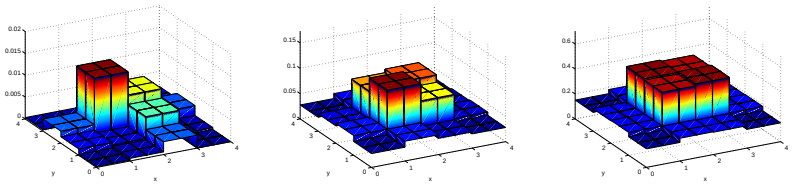

(a) 0.0% Bias Error (b) -1.0% Bias Error (c) -5.0% Bias Error

Fig. IV-34. Ex. 12: Error in reconstruction with a negative signal bias of a centered strong absorber

F. Muli-group Results

With the multigroup equations it is possible to reconstruct multiple parameters at once, for example the removal cross section of every group or a combination of removal cross section and fission cross section simultaneously. In the case of two parameters to be reconstructed, a homogeneous domain can be considered and a misfit surface plot can be constructed to observe the dimensional space of the misfit with respect to the two parameters.

1. Multi-group Misfit Plots

a. Example 13: Multigroup misfit plots of absorption cross sections only

The misfit surface code was modified to examine the variation of the misfit function in the case of a single region multigroup example with respect to various cross-section combinations. This enabled a visualization of reconstruction difficulty with respect to various parameter combinations. The first case that was tested consisted of a two group problem. $\chi_1 = 1$ and $\chi_2 = 0$, and the misfit was computed as a function of $\Sigma_{r,1}$ and $\Sigma_{r,2}$. This problem is very similar to the original one group problem in such there are two systems in energy coupled by parameters different than the ones being

reconstructed. Similarly to the one group models, $\Sigma_{r,i}$ can be reconstructed for any number of energy groups. With incident beams in both energy groups, this misfit surface plot is shown in Figure IV-35. As expected, with incoming beams in both groups, reconstruction of both parameters is fairly simple. If the incident neutrons were only in one group, for example the fast group, the ability to reconstruct was tested as well.

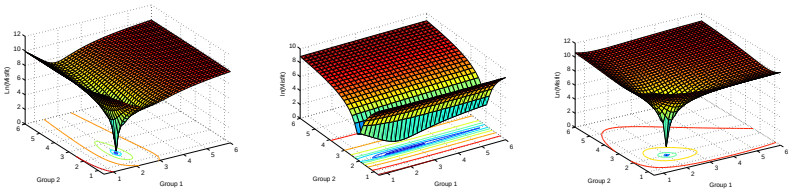

(a) Fast Group Incident Flux (b) Thermal Group Incident Flux (c) Both Group Incident Flux

Fig. IV-35. Ex. 13: Misfit surface plot of $\Sigma_{r,1}$ and $\Sigma_{r,2}$ for 2 group homogeneous region while varying source energy

In the case where incident neutrons are only in the fast group, the problem is more ill-posed as the misfit function has an elongated valley as opposed to a steep conic shape. While reconstruction ability is lower if incident neutrons are not in every group, the coupling of the groups provides enough data for reconstruction of parameters in the other groups. The misfit surface plot changed from a smooth conic shape to smeared cone in the $\Sigma_{r,2}$ direction. In the case where incident neutrons are only in the thermal group, an even more ill-posed problem is present. The reconstruction ability is strongly dependent on the coupling between the two group, down scattering or fission source, and when the source is weak in comparison to the incident neutrons, the problem may be very ill-posed. In multigroup models, incident beams in every group does add reconstruction ability.

b. Example 14: Multigroup misfit plots of fission cross sections only

The next problem space that was tested with the misfit surface plot consisted of $\Sigma_{f,1}$ and $\Sigma_{f,2}$ in a 2 group problem. When reconstructing fission cross sections, one must be careful due to physical limitations of the problem itself. When modifying $\nu\Sigma_f$, special care must be taken due to physical constraints such as criticality and $\Sigma_f \leq \Sigma_a$. In a realistic manner, if $\Sigma_f = \Sigma_a$ and $\nu\Sigma_f$ is still increased, due to Σ_f limitations would have to imply that ν was increasing. This can lead to criticality issues very quickly if conservative step length control is not implemented.

In this problem, when the fission cross section is modified by a large amount, and the multiplication factor of the domain becomes greater then one, the flux can result in a negative solution. The FEM diffusion solver implements the fission terms not as a fixed source but in the current solution, when the system approaches criticality, interesting results can occur such as negative fluxes in certain regions.

These physical limitations really limit the $\Sigma_{f,i}$ and $\Sigma_{f,j}$ workspace to a region around the true solution if they are the only parameters being modified. Now that physical limitations of simply modifying these parameters has been established, a visualization of the reconstruction space was performed. The misfit function was computed as a function of $\Sigma_{f,1}$ and $\Sigma_{f,2}$ of a homogeneous domain and results shown in Figure IV-36. This function space is much flatter than the Σ_r space where quadratic approximations in the Newtonian direction converged less slowly.

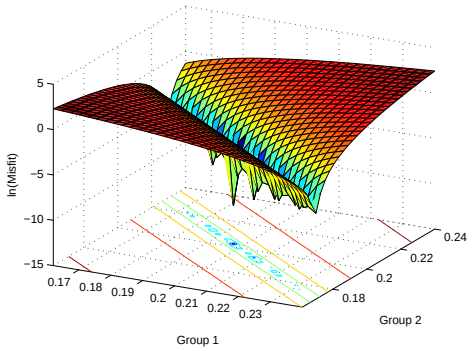

Fig. IV-36. Ex. 14: Misfit surface plot of $\Sigma_{f,1}$ and $\Sigma_{f,2}$ for 2 group homogeneous region

This $\Sigma_{f,i}$ vs. $\Sigma_{f,j}$ workspace has a misfit several orders of magnitude lower then the $\Sigma_{r,i}$ vs. $\Sigma_{r,j}$ workspace. This is partially due to the magnitude of the parameters themselves. Due to criticality concerns, any fissile material placed in a large container, would have to either be spread out or only be of a small quantity. From a reconstruction standpoint, this would lead to a fission cross section much lower then the total absorption cross section on the parameter grid due to the resolution in the reconstruction homogenization. In the misfit surface plot of the $\Sigma_{f,i}$ vs. $\Sigma_{f,j}$ workspace, the parameters can change significantly compared to the $\Sigma_{r,i}$ vs. $\Sigma_{r,j}$ workspace while maintaining a low misfit. This data can be extrapolated to the case of the centered fissile material expecting to limit the maximum reconstruction depth to be shorter than the non-fissile case. One extreme example of the ill-posedness of this type of problem is consisted of a very strong absorber with a fissile region with significantly lower fission cross section than the absorption cross section in the center of a domain, the fission rate, no matter what the fission cross section is, will have little effect on the boundary fluxes.

When χ is distributed across more then one group such as the previously mentioned 4 group example, similar improvements occur, such as the $\Sigma_{r,1}$ and $\Sigma_{f,1}$, but

the workspace for reconstruction is considerably smaller due to physical constraints.

c. Example 15: Multigroup misfit plots of mixed parameters

The next examples consisted of mixed parameters of type and group, for example $\Sigma_{r,i}$ and $\Sigma_{f,j}$. Reconstructions of this type are simpler then fission in multiple groups due to the parameters are coupled weaker with respect to their energy groups. For example, reconstruction of fission in both groups of two total groups, both parameters produce neutrons in group one and are strongly coupled by both the groups fluxes. While in a four group example, if $\Sigma_{f,4}$ and $\Sigma_{r,2}$ are reconstructed they are coupled weaker and are simpler to reconstruct such as reconstructions of single parameters are. Although mixed parameter reconstructions may have a limited workspace in the Σ_f dimension, reconstruction ability is significantly greater due to Σ_r flexibility.

Next, the misfit is computed as a function of $\Sigma_{r,1}$ and $\Sigma_{f,1}$. This problem is very similar to the original one group problem in such that the addition of the second group provided no additional information to these two parameters as long as $\chi_2 = 0$. This function shows a line solution as the minimum as expected and is shown in Figure IV-37. If a 4 group problem is considered, and χ = [0.9 0.1 0.0 0.0] for the four corresponding groups and same misfit was computed, since $\chi_2 = 0.1$ additional information is provided to $\Sigma_{f,1}$. The resulting misfit surface plot is still an elongated valley, but instead of a line solution it has a minimum enabling reconstruction for this case.

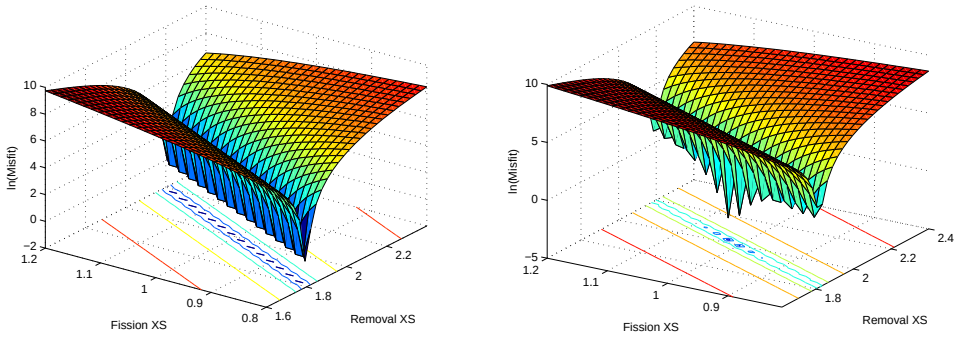

(a) 2 Group (b) 4 Group

Fig. IV-37. Ex. 15: Misfit surface plot of $\Sigma_{r,1}$ and $\Sigma_{f,1}$ for 2 and 4 group homogeneous regions

One example of mixed parameter reconstruction is tested for a four group case. This example consists of $\chi = [0.9\ 0.1\ 0.0\ 0.0]$ where the misfit is computed as a function $\Sigma_{r,2}$ and $\Sigma_{f,4}$ then the same parameters with reverse groups and results shown in Figure IV-38.

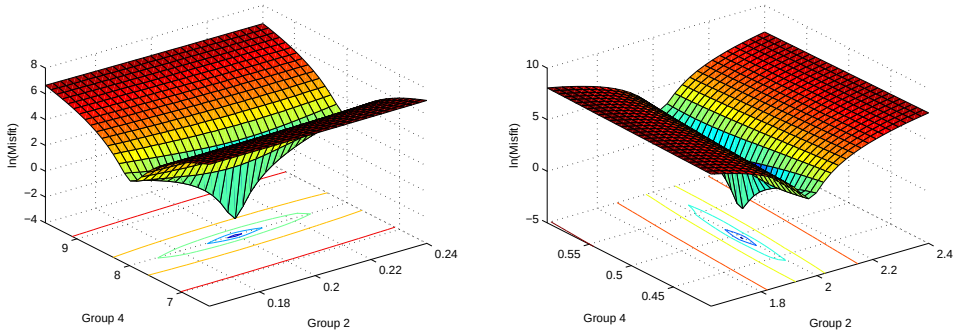

(a) $\Sigma_{r,2}$ and $\Sigma_{f,4}$ (b) $\Sigma_{f,2}$ and $\Sigma_{r,4}$

Fig. IV-38. Ex. 15: Mixed parameter misfit surface plots for 4 energy groups

Instead of the typical Σ_r vs. Σ_r type conic surface, as shown before the misfit function is much flatter in the Σ_f space, so the misfit is expected to change slower

in the Σ_f direction of the Σ_r vs. Σ_f misfit plot. The same effect is shown when the parameters groups are switched.

2. Multigroup Reconstruction Results

a. Example 16: Reconstruction of a thermal strong absorber

The first case consists of reconstruction of Σ_r for multiple groups. As mentioned previously, this example resembles weakly coupled one group cases solved simultaneously so high reconstruction ability is expected. This is essentially the base fundamental reconstruction and similar tests as the single group can be compared to test the reconstruction limits. The test case considered consisted of a homogeneous domain with a centered strong thermal absorber. This is similar to the previous centered strong absorber except that in this test case it only exists in group 2 of 2 total groups. The reconstruction for this problem is shown in Figure IV-39 and corresponding error in Figure IV-40.

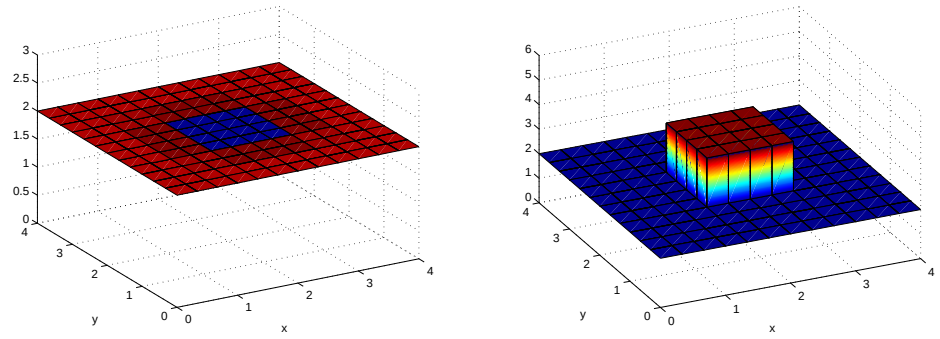

(a) Group 1 Recon. (b) Group 2 Recon.

Fig. IV-39. Ex. 16: Multigroup reconstructions of a thermal centered absorber

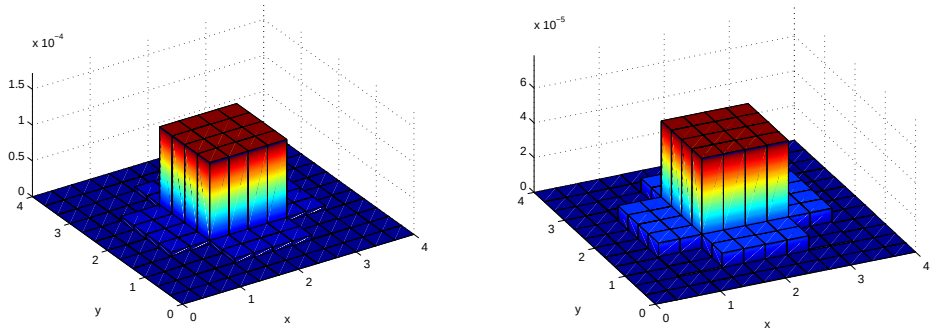

(a) Group 1 Error (b) Group 2 Error

Fig. IV-40. Ex. 16: Error in multigroup recon. of a thermal centered absorber

Essentially the same reconstruction limits for one group problems are similar here for Σ_r reconstructions for multigroup problems. They can be viewed as separate systems only weakly coupled by fission and scattering terms and modification of the Σ_r does not have any limits with respect to the other cross sections making a large workspace in the reconstruction space.

b. Example 17: Reconstruction of centered fissile material

The next example problem attempts to reconstruct the fission cross section of a centered strong fissile material. As mentioned before, the misfit space for the fission cross section is strongly dependent on the magnitude of the fission cross section and this example consists of a centered strong fissile region inside a domain. This problem consists of a coarse mesh of 8×8 or 64 regions to reconstruct and the domain properties shown in Table IV-V.

Table IV-V. Ex. 17: Domain parameters of centered fissile material

Region	D_1	D_2	$\Sigma_{a,1}$	$\Sigma_{a,2}$	$\Sigma_{f,1}$	$\Sigma_{f,2}$
Outer	0.5	0.5	2.0	3.0	0.01	0.01
Center	0.5	0.5	2.0	3.0	0.30	0.30

With an initial guess of $\Sigma_{f,1} = 0$ and $\Sigma_{f,2} = 0$ for the entire domain and, using eight experiments, the optimality conditions were iterated down to the order of 10^{-7}. This reconstruction is shown in Figure IV-41 and reconstruction error in Figure IV-42.

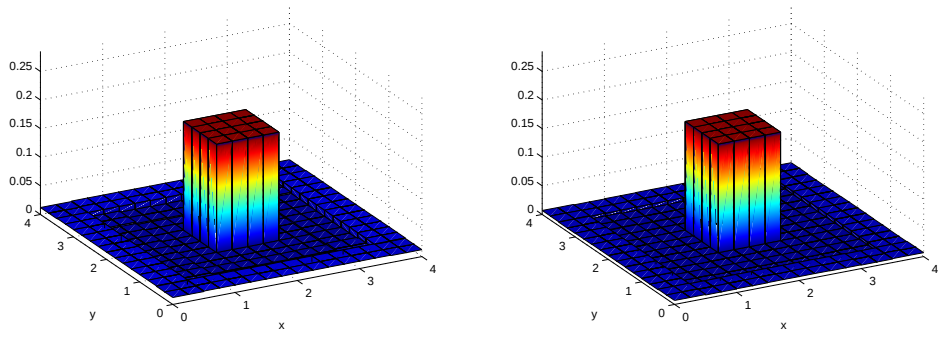

(a) Group 1 Recon. (b) Group 2 Recon.

Fig. IV-41. Ex. 17: $\Sigma_{f,1}$ and $\Sigma_{f,2}$ reconstructions of centered fissile material

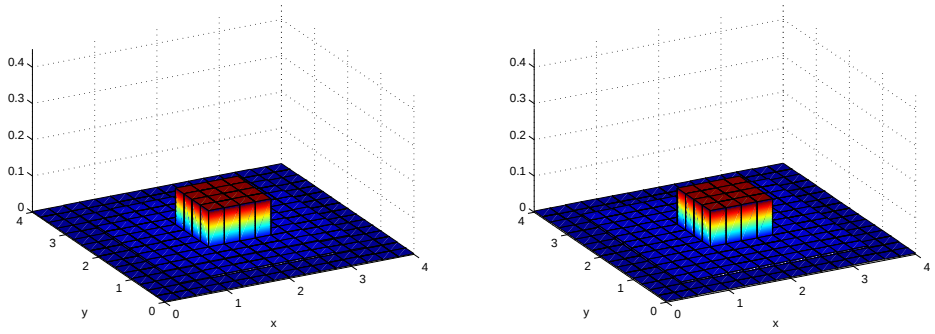

(a) Group 1 Error (b) Group 2 Error

Fig. IV-42. Ex. 17: Error in $\Sigma_{f,1}$ and $\Sigma_{f,2}$ reconstructions of centered fissile material

The reconstruction error is significantly greater then the previous removal or absorption cross-section reconstructions while the optimality conditions are driven down to the same magnitude. This is a result of the ill-posedness of the problem as shown by the flatness of the misfit plot. While the center region has the highest reconstruction error, it is still noticeable that there is stronger fissile material there.

c. Example 18: Maximum reconstruction depth testing for $\nu\Sigma_f$

Another fission reconstruction example demonstrates the maximum reconstruction depth. A simple domain of 8×8 consisting of side by side homogeneous pieces with a total of 64 regions of reconstruction is employed here. This domain has dimensions of approx 12 cm $\times$ 12 cm ($L \approx 1$cm) and 16 experiments are used in this reconstruction each consisting of a beam covering one fourth of a side. This simple case is used as a benchmark to test fission cross-section reconstruction depth. This examples material properties are given in Table IV-VI.

Table IV-VI. Ex. 18: Domain parameters of two region fissile material

Region	D_1	D_2	$\Sigma_{a,1}$	$\Sigma_{a,2}$	$\Sigma_{f,1}$	$\Sigma_{f,2}$
Left	0.33	0.33	2.0	3.0	0.2	0.3
Right	0.33	0.33	3.0	4.0	0.3	0.4

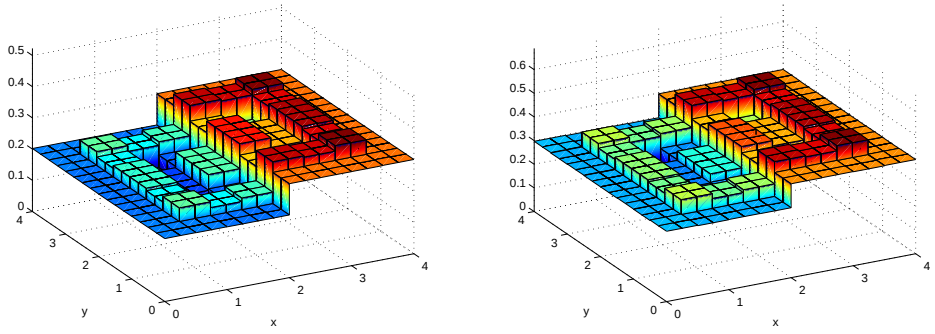

(a) Group 1 Recon. (b) Group 2 Recon.

Fig. IV-43. Ex. 18: $\Sigma_{f,1}$ and $\Sigma_{f,2}$ reconstructions of a two zone fissile step

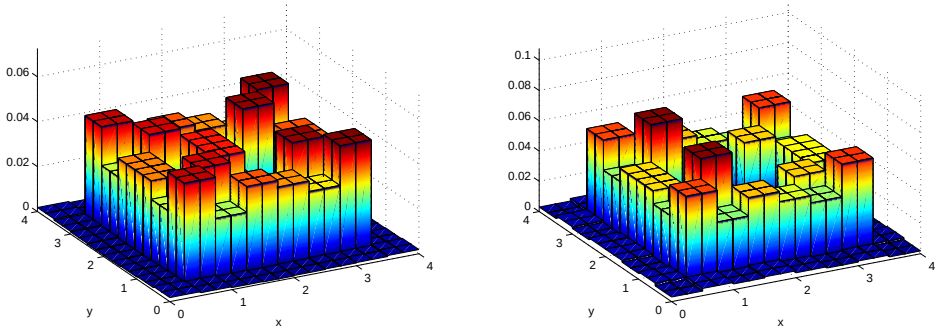

(a) Group 1 Error (b) Group 2 Error

Fig. IV-44. Ex. 18: Error in $\Sigma_{f,1}$ and $\Sigma_{f,2}$ reconstructions of two zone fissile step

This reconstruction, in Figure IV-43 and error in Figure IV-44, was approxi-

mately the maximum depth any noticeable features can be distinguished for fission cross-section reconstructions. This reconstruction was approximately 6 characteristic lengths deep, or half the domain size, where noticeable internal features become indistinguishable. The maximum depth for fission parameter reconstruction is approximately 5-6 characteristic lengths which is 1-2 characteristic lengths shorter then removal cross-section reconstructions.

d. Example 19: Mixed parameter reconstructions

The final multigroup reconstruction problem consists of mixed parameter reconstructions. Due to the physical limitations on Σ_f with respect to Σ_a there is less freedom for parameter modification in these cases, causing the reconstruction space to be smaller. The first case was a 2-group problem where $\Sigma_{r,1}$ and $\Sigma_{f,2}$ are reconstructed. This example has the same paramters as shown in Table IV-VI. The domain has size of 1 cm $\times$ 1 cm ($L \approx 0.33$cm) and strong reconstruction ability is expected. Results from the reconstruction of $\Sigma_{r,1}$ and $\Sigma_{f,2}$ are shown in Figure IV-45.

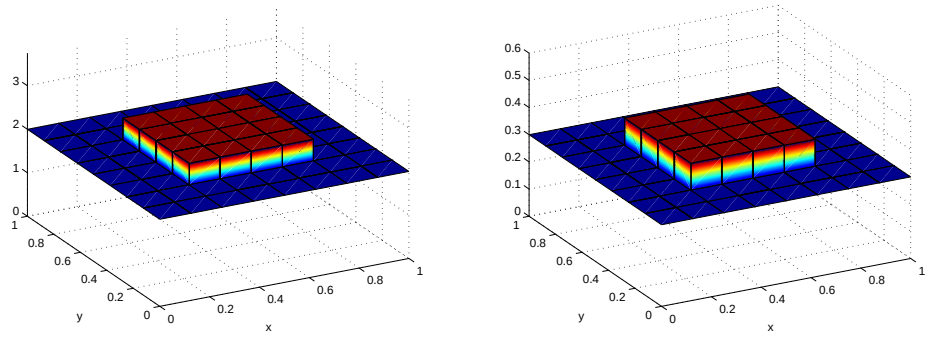

(a) $\Sigma_{r,1}$ (b) $\Sigma_{f,2}$

Fig. IV-45. Ex. 19: Mixed parameter reconstructions for a 2 group problem

As expected, the mixed parameter reconstruction is excellent and the error is

shown in Figure IV-46.

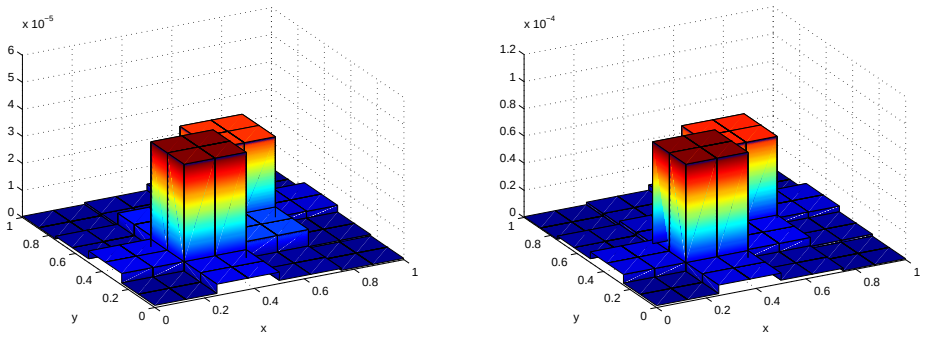

(a) $\Sigma_{r,1}$ (b) $\Sigma_{f,2}$

Fig. IV-46. Ex. 19: Error for mixed parameter reconstructions for a 2 group problem

The reconstruction parameter groups are then and $\Sigma_{f,1}$ and $\Sigma_{r,2}$ are reconstructed and results shown in Figure IV-47.

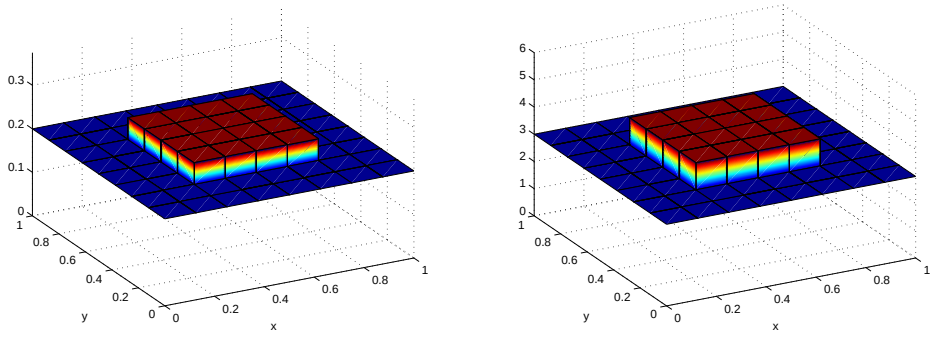

(a) $\Sigma_{f,1}$ (b) $\Sigma_{r,2}$

Fig. IV-47. Ex. 19: Mixed parameter reconstructions for a 2 group problem

As in the previous example, an excellent reconstruction is obtained with resulting error in Figure IV-48.

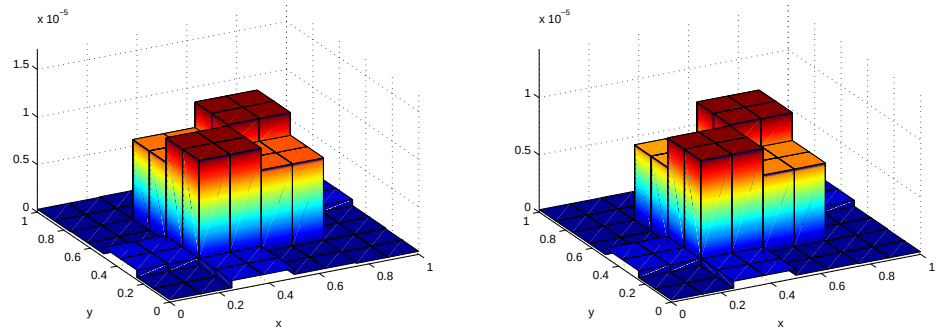

(a) $\Sigma_{f,1}$ (b) $\Sigma_{r,2}$

Fig. IV-48. Ex. 19: Error for mixed parameter reconstructions for a 2 group problem

e. Example 20: Variation of incident neutron and measurement energy

A more ill-posed problem is at hand, as seen by the misfit surface plots in Figure IV-35, when incident neutrons are not present in all groups or measurements are not made in all groups. To demonstrate this, a two-group problem is considered where incoming neutrons are only present in group one and measurements are only made in group 2 and both groups removal cross section is attempted to be reconstructed. In a problem where measurements are made in a group that does not contain any incident neutrons, reconstruction ability is strongly dependent on the source of neutrons to this group by scatter or fission. For this example, the domain properties are shown in Table IV-VII.

Table IV-VII. Ex. 20: Domain parameters for a multigroup centered strong absorber

Region	D_1	D_2	$\Sigma_{a,1}$	$\Sigma_{a,2}$	$\Sigma_{f,1}$	$\Sigma_{f,2}$	$\Sigma_{s,1\to2}$	$\Sigma_{s,2\to2}$
Outer	1	1	0.2	0.2	0.05	0.1	0.14	0.0
Center	1	1	0.4	0.4	0.05	0.1	0.14	0.0

The results for the reconstruction in group one are shown in Figure IV-49.

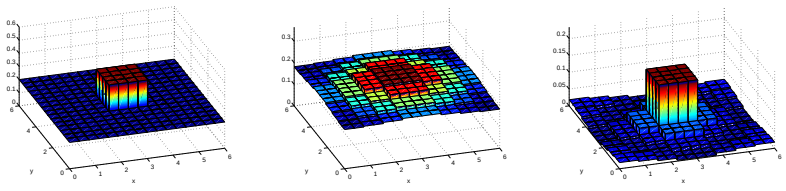

(a) True $\Sigma_{r,1}$ (b) Recon. $\Sigma_{r,1}$ (c) Error

Fig. IV-49. Ex. 20: Reconstruction of $\Sigma_{r,1}$ with incident neutrons only in group one and measuring only in group 2

The results for the reconstruction in group two are shown in Figure IV-50.

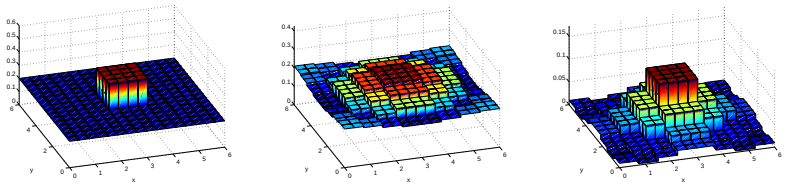

(a) True $\Sigma_{r,1}$ (b) Recon. $\Sigma_{r,1}$ (c) Error

Fig. IV-50. Ex. 20: Reconstruction of $\Sigma_{r,2}$ with incident neutrons only in group one and measuring only in group 2

These reconstructions are not of high quality as the strong absorbers appear to be smeared throughout the domain. This due to the lack of information produced by the presence of incoming neutrons and measuring in single different groups. Even though this domain may have high reconstruction ability with incident neutrons and measurements in both groups, reducing these to one each greatly affects the reconstructions.

CHAPTER V

CONCLUSIONS

The inference or reconstruction of material parameters inside a domain is presented as a PDE-constrained optimization problem. In such problems, non-invasive inverse problem techniques are employed using only boundary input and output as information. An initial guess is performed, then an attempt to iterate to the solution is made where Newton's method implemented.

When a reconstruction is attempted on a domain there are several factors that play a key role in the ability of reconstruction no matter the complexity of the domain. Such factors are the location of measurements, location of incoming beams, and which parameter is being reconstructed. Through a misfit analysis, the location of incident and measurement location has been shown to severely affect the ability of reconstruction. For example in the two parameter case, or side by side homogeneous regions, if you only measure or have incoming particles on one side of the domain, the magnitude of the properties on the other side will have very little effect on the flux at the measurement points. Problems such as this are very ill-posed where the material parameters can change significantly whereas the resulting fluxes at the measurement points have little or no change. In such problems, the optimality conditions must be driven as low as possible to achieve meaningful results. This knowledge can be extracted to more complicated cases and problems can be approached with greater knowledge to provide the best possibility of reconstruction for any given domain.

The material parameter that is being reconstructed plays a role in the ability to reconstruct it based on its magnitude with respect to the other parameters. For example in a moderately thick domain of very strong absorption cross section, if the

center region had a very weak fission cross section, such few of these neutrons born from fission in the center actually make it to the measurement points therefor having negligible change on the boundary fluxes even with significant change in the center region's fission cross section therefore having negligible change on the misfit.

In the one group case with position dependent parameter reconstruction, an attempt at reconstructing the neutron absorption cross section was performed with incoming neutron beams on all four sides of the two dimensional domain. This model proves reconstruction of material parameters is possible with PDE-constrained optimization and more complicated applications should be implemented.

The concept of multiple experiments has been introduced next, where the neutron source is moved creating multiple separate flux and adjoint solutions while the problem optimizes the same set of cross sections. When multiple experiments were applied to this one group problem, a large increase in reconstruction ability was shown. Domains of certain complexity or size that no internal features distinguishable using only one experiment could now be reconstructed successfully. While the addition of multiple experiments proves greater reconstruction ability, no matter how many experiments are used, there still are reconstruction limits with respect to domain size and resolution. In the benchmark case of the centered strong absorber, the maximum reconstruction depth was limited to approximately 6-7 diffusion lengths deep from the boundary. When a domain of larger size is considered, even with a large number of experiments, the internal features of the domain cannot be reconstructed. Reconstruction resolution has limits as well, such that if the size of a domain is held constant and a finer and finer mesh considered, no matter how many experiments used, reconstruction resolution is limited to a fraction of an optical thickness.

The addition of signal noise or bias on the synthetic measured solutions severely affects the reconstruction ability of a domain. In small sized domains, such as 4

$\times$ 4, the addition of signal noise up to about 1.0% still allows reconstruction of distinguishable features of a domain while for larger domains, small quantities of signal noise around 0.005% to 0.01% may still be enough to destroy reconstruction ability. When a signal bias is applied to the synthetic measured solution, or signal noise averaged higher or lower then zero, it is expected that if the measured solutions are stronger, the cross sections be lower causing less attenuation and vice versa. The results from cases where reconstruction ability is high, this shows to be true although areas where reconstruction ability is low error increases significantly with the addition of signal noise or bias.

In the approximation, the same reconstruction limits do not always apply to the inference of various parameters from different energy groups. In the case of removal cross sections only to be reconstruction, these parameters do not couple the groups together in any way and is similar to reconstruction of two one-group problems simultaneously. In this reconstruction parameter configuration, the same reconstruction limits from the one group absorption problems arise here as well. The same maximum reconstruction depth of 6-7 diffusion lengths deep from the boundary is seen here.

If fission cross sections are to be reconstructed, a more complicated problem arises. In simple homogeneous domains, the fission cross section can be reconstructed easily just as the removal cross section. In more complicated problems, the ratio of fission cross section to absorption cross section may play a role in the ability to reconstruct. As mentioned before in the case of a strong absorber around a centered region of weak fissile material, due to the magnitude of the fission cross section with respect to the strength of the absorber, the misfit space in this problem is significantly flatter with respect to change in the cross section. The fission cross section in the center can change significantly without noticeable change in the boundary fluxes and

misfit. This problem is more ill-posed than the case of absorption or removal cross-section reconstruction as shown by the magnitude of the misfit surface plots. Through similar test problems, the maximum reconstruction depth of approximately 5 diffusion lengths is present for multigroup fission cross-section reconstructions. This is smaller then the removal or absorption reconstruction limits by a significant quantity of 1-2 characteristic lengths.

Subsequent work may include a transport model for the governing physics constraint. The same optimization methods would apply, except a transport operator would replace the diffusion operator. This will provide more accurate flux solutions especially in cases where the diffusion approximation is weak. Additional subsequent work may include the implementation of more constraints, for example using barrier methods, for complex problems where the optimization functional is not smooth.

REFERENCES

[1] J. Baker McNeill, "100 percent cargo container scanning: A global disaster," Research report, Kathryn and Shelby Cullom Davis Institute for International Studies, 2008.

[2] K. Ren, G. S. Abdoulaev, and A. H. Hielscher, "Optical tomography as a PDE-constrained optimization problem," *Inverse Problems*, vol. 21, pp. 1507–1530, 2005.

[3] Wolfgang Bangerth and Amit Joshi, "Adaptive finite element methods for the solution of inverse problems in optical tomography," *Inverse Problems*, vol. 24, pp. 034011/1–22, 2008.

[4] A. D. Klose and A. H. Hielscher, "The inverse source problem based on the radiative transfer equation in optical molecular imaging," *Journal of Computational Physics*, vol. 202, pp. 323–345, 2005.

[5] A. Gibson, M. Schweiger, and S. R. Arridge, "Computational aspects of diffuse optical tomography," Research report, Computing in Science & Engineering, Los Alamitos, CA, 2003.

[6] W. Hardin, "Cargo inspection: Imaging solutions wait for government's call," Research report, Machine Vision Online.

[7] V. Scipolo, "Scattered neutron tomography based on a neutron transport problem," M.S. thesis, Texas A&M University, College Station, Texas, May 2004.

[8] Jorge Nocedal and Stephen J. Wright, *Numcerical Optimization, 2nd edition*, Springer Science+Business Media, Madison, WI, 2006.

[9] J. A. Favorite and R. Sanchez, "An inverse method for radiation transport," *Radiation Protection Dosimetry*, vol. 116, pp. 482–4585, 2005.

[10] Computational Science Education Project, *Mathematical Optimization*, United States DOE, e-book, http://www.phy.ornl.gov/csep/, 1996.

[11] Murat Aydin and M. Akif Atalay, "Inverse neutron diffusion problems in reactor design," *Journal of Nuclear Science and Technology*, vol. 44, pp. 1142–1148, 2007.

[12] Weston M. Stacey, *Nuclear Reactor Physics*, Wiley-VCH GmbH & Co. KGaA, Weinheim, 2004.

[13] Richard L. Burden and J. Douglas Faires, *Numerical Analysis, 8th edition*, Thomson Brooks/Cole, Belmont, CA, 2005.

[14] Nuclear Data Evaluation Lab., "Table of nuclides," Tech. Rep., Korea Atomic Energy Research Institute, 2000.

[15] National Nuclear Data Center, "Evaluated nuclear data file (endf)," Tech. Rep., Brookhaven National Laboratory, 2009.

VITA

Matthew Ryan Sternat was born in 1982 to Louis J. Sternat Jr. and Patricia Sternat in Friendswood, TX. He graduated from Friendswood High School in 2001, received his Bachelor of Science in nuclear engineering from Texas A&M University in 2007 and his Master of Science in nuclear engineering from Texas A&M University in 2009. He is a member of Alpha Nu Sigma Honor Society and the National Scholars Honor Society. His primary interests are numerical reactor physics and application towards nuclear safeguards.

Department of Nuclear Engineering
Texas A&M University
3133 TAMU
College Station, TX 77843-3133

m.sternat@tamu.edu
matt.sternat@gmail.com

B Appendix 2

AN ITERATIVE TECHNIQUE FOR IMAGING HETEROGENEOUS OBJECTS USING TRANSPORT THEORY AND NEWTON'S METHOD

A Thesis

by

NATHANIEL RAYMOND FREDETTE

Submitted to the Office of Graduate Studies of
Texas A&M University
in partial fulfillment of the requirements for the degree of

MASTER OF SCIENCE

December 2011

Major Subject: Nuclear Engineering

AN ITERATIVE TECHNIQUE FOR IMAGING HETEROGENEOUS OBJECTS USING TRANSPORT THEORY AND NEWTON'S METHOD

A Thesis

by

NATHANIEL RAYMOND FREDETTE

Submitted to the Office of Graduate Studies of
Texas A&M University
in partial fulfillment of the requirements for the degree of

MASTER OF SCIENCE

Approved by:

Co-Chairs of Committee,	Jean C. Ragusa
	Wolfgang Bangerth
Committee Members,	Marvin Adams
Head of Department,	Raymond Juzaitis

December 2011

Major Subject: Nuclear Engineering

ABSTRACT

An Iterative Technique for Imaging Heterogeneous Objects Using Transport Theory and Newton's Method. (December 2011)

Nathaniel Raymond Fredette, B.S., Marquette University;

Co–Chairs of Advisory Committee: Jean C. Ragusa
Wolfgang Bangerth

This thesis explores the inverse problem of optical tomography applied two-dimensional heterogeneous domains. The neutral particle transport equation was used as the forward model for how neutral particles stream through and interact within these heterogeneous domains. A constrained optimization technique that uses Newton's method served as the basis of the inverse problem.

The capabilities and limitations of the presented method were explored through various two-dimensional domains. The major factors that influenced the ability of the optimization method to reconstruct the cross sections of these domains included the locations of the sources used to illuminate the domains, the number of separate experiments used in the reconstruction, the locations where measurements were collected, the optical thickness of the domain, the amount of signal noise and signal bias applied to the measurements and the initial guess for the cross section distribution. All of these factors were explored for problems with and without scattering.

Increasing the number of source and measurement locations and experiments generally was more successful at reconstructing optically thicker domains while producing less error in the image. The maximum optical thickness that could be reconstructed with this method was ten mean free paths for pure absorber and two mean free paths

for scattering problems. Applying signal noise and signal bias to the measured fluxes produced more error in the produced image. Generally, Newton's method was more successful at reconstructing domains from an initial guess for the cross sections that was greater in magnitude than their true values than from an initial guess that was lower in magnitude.

To my father and mother, Mark and Denise Fredette

ACKNOWLEDGMENTS

I would like to acknowledge my father and mother, Mark and Denise Fredette, for there support and advice during the process of achieving this degree. I would also like to acknowledge my sister, Jackie Fredette, for her suggestions. I would thank my friends and family for helping me develop into a productive young professional.

I would like to acknowledge Dr. Jean C. Ragusa for his time and support throughout this project, his knowledge of transport methods and his professional counsel when considering my career options. In addition, I would like to acknowledge Dr. Wolfgang Bangerth for his insight regarding optimization methods and programming.

TABLE OF CONTENTS

CHAPTER Page

CHAPTER Page

LIST OF TABLES

LIST OF FIGURES

FIGURE Page

FIGURE Page

FIGURE Page

FIGURE Page

FIGURE Page

FIGURE Page

FIGURE Page

CHAPTER I

INTRODUCTION

A. Motivation

A current area of research interest in national security is to effectively and efficiently determine the contents of the many shipping containers that enter ports in the United States. This interest comes as a result of the 9/11 Commission Act passed by Congress in 2007 that requires 100% of inbound cargo to be scanned by 2012.[1] It does not appear that this requirement will be achieved by 2012, but as of Feburary of 2009 eighty percent of the 11.5 million inbound cargo containers were being scanned.[2]

The systems used today in all major U.S. ports to determine the presence of radioactive material within cargo containers are Radiation Portal Monitors (RPM). These devices generally exist in the form of a gate or series of gates that the containers can be driven through and scanned. The monitors are effective for determining the presence of radiation, but offer little more information about the particular source. This simple pass-fail system leads to many false alarms as many everyday items emit radiation including smoke detectors due to the americium-241 source contained inside, bananas, milk, cocoa powder and lean beef due to the trace amounts of potassium-40,[3] and fire brick and kitty litter due to their high clay content which often contains traces of uranium and thorium. In addition, if an illuminating source is imposed on the boundary of the container, the contents of the container may become activated. These materials include steel, aluminum and many agricultural products.[3] Current portal monitors also have not proven to be that effective at identifying natural or highly enriched uranium (HEU). In fact, the best available Advanced Spectroscopic Portal Monitors (ASP) are only capable of identifying bare HEU 70-88 percent of the time

and masked HEU and depleted uranium (DU) only 53 percent of the time.[4] Therefore, a better algorithm that uses more information collected from better detectors about the specific material distribution within the container is desired.

B. Inverse Problems

An inverse problem can be generally defined as case where one wants to know the values of some unknown quantities, often the material properties of a object, but only has access related quantities.[16] This relationship between the desired quantities and the related quantities can be modeled by a partial differential equation (PDE). This PDE serves as the basis for the forward model, since the related measurable quantities (the particle flux or count at a detector location, for instance) can be computed from solving the PDE given some yet unknown quantities (again material properties). Therefore, one must successively guess values of the unknown parameters and solve the PDE to obtain values for the measurable quantities. The values of the computed quantities that result from solving the PDE are then compared with the actual observed quantities and sophisticated techniques are used to propose the next guess for the values of these parameters. This process is then repeated until the difference between is the observable quantities and the computed quantities is reduced to some acceptable level. These inverse problems can be found in many fields including groundwater flow,[16,20] DC resistivity,[20] hydraulic head,[16] optical tomography,[10–18,20] magnetotelluric inversion[20] and gravity gradiometry.[16] Optical tomography is the inverse problem considered in this Thesis.

Since only the values of some related quantities are available at some distance away from the object of interest, inverse problems are ill-posed. This means that the observable quantities could arise from an object of many different parameter

distributions. Because of this fact, the solution to inverse problems is known to be much more difficult to find that simply solving the forward problem. There are also many factors common to many inverse problems that effect the ability to find the searched parameters. Some of these factors are the number and locations of the measuring devices, the number of separate experiments that are conducted where measurements are collected, the amount of signal noise present in the environment, the amount of signal bias due to the limitations of the measuring device, the initial guess for the parameter distribution, the material properties of the object and any surrounding materials and the magnitude of the measurable signal. Each of these factors that affect the ability to find the solution to the inverse problem will be considered in this Thesis.

The specific inverse problem considered in this Thesis is the problem of inverse neutral particle transport through a cargo container. Like many inverse problems, only a measurable quantity of radiation that escapes the container will be used to generate an image of the container. Therefore, when actually implemented, some detection system will be required to collect measurements of the fluxes emitted from the cargo container. Many different detectors can can be used in portal monitors such as scintillators such as Sodium Iodide (NaI), High Purity Germanium (HPGe), Polyvinyl Toluene (PVT) for gamma particle detection and gas-filled detectors like Helium-3 (He-3) tubes for neutron detection. These detectors are positioned within the portal monitor on multiple sides of the scanned vehicle to measure the radiation emitted from the boundary of the vehicle. The portal monitors are used to measure the natural radiation that is emitted from the contents of the cargo container passively or the emitted radiation when sources are used to actively illuminate the container by imposing neutral particles on different sides and at different angles. Active interrogation will be the focus of this Thesis.

Several simplifications will be made in this Thesis to lay the ground for a proof-of-principle demonstration. The cargo container problem will be simplified to a study on two-dimensional heterogeneous domains. The external illuminating sources will be imposed on the boundaries of the domains and only the most normal angles determined by the Sn angular quadrature will be used. The number of possible imposed boundary sources and measurement locations considered in this Thesis will be equivalent to the dimensions of the material map for the considered domain. Several other assumptions will be made in this Thesis to simplify the inverse transport process and they will be presented in the Chapters III, IV and V.

C. Optimization

In mathematics, a simple optimization process can be defined as a systematic approach to minimize or maximize some real function based on choosing values of parameters from a set of acceptable values. There are many different optimization methods that cater to many different specific problem types. Inverse problems are often difficult, ill-posed optimization problems where convergence cannot be guaranteed. Constraints can be applied to the optimizer to narrow the set of possible parameters that will be proposed. In addition, the more information that is provided in the optimization routine, the faster this process can be conducted. This is why derivative free methods where the gradient of the objective function is not provided generally perform slower than methods that use the gradient information. However, the faster Newton-based routines that use gradient information can introduce additional convergence problems. For instance, if the gradient of the objective function is very close to zero, then Newton's method can propose a new guess for the parameters that is very far from the actual minimum and the method can diverge. Both the Nelder-Mead and Newton's methods were explored in this document.

In the case of our problem, the objective or misfit function that is to be minimized is a measure of the difference between the measured boundary angular fluxes as recorded from the detector and the computed angular fluxes as calculated from our model. The computed angular fluxes with be calculated by solving the transport equation iteratively with updated parameters provided by the optimization routine. The formulation of the optimization problem yields systems of nonlinear equations because of the coupling between angular fluxes and cross sections. In addition, because small changes in cross sections can lead to large changes in angular fluxes, the problem is ill-posed.

D. Outline of Thesis

In Chapter II, a summary of some methods that have been explored with respect to solving the inverse problems of cargo container imaging, optical tomography, applied DC-resistivity and magnetostatics is presented. In Chapter III, the transport equation and adjoint transport equation are presented as the balance equations used to model the transport of radiation through a heterogeneous medium. In Chapter IV, the optimization process is described as well as some of the methods investigated in this document. In Chapter V, the particular optimization problem of inverse neutral particle transport through a cargo container is introduced. This entails establishing the objective function, Lagrangian relationship, the optimality conditions and the Hessian matrix. In Chapter VI, some sample problems are presented that were explored to determine some of the capabilities and limitations of the method. Results from both the derivative-free and Newton based methods are presented in this section. In Chapter VII, conclusions are drawn from the results collected in this study. Suggestions for future research in inverse neutral particle transport applied to cargo container imaging are also made in this section.

CHAPTER II

PREVIOUS WORK

A. Inverse Neutral Particle Transport Related to Cargo Container Imaging

The conservation of neutral particles can be modeled using the transport equation. This neutral particle transport equation is applicable to neutron, gamma and coupled neutron-gamma transport. In this Thesis, only neutron transport will be considered, but the model is applicable to other neutral particle transport problems.

The idea of using neutron transport to noninvasively infer the contents of shipping containers is a topic of growing interest for national security reasons. Many researchers in United States are working to solve this challenging problem. Several researchers at Texas A&M University have investigated this topic and three unique approaches to cargo imaging are discussed in the following paragraphs.[7–9]

First, the idea of using both transmitted and scattered radiation to reconstruct images of a object was suggested by Scipolo.[7] In the process of using transmitted radiation, the difference between the original beam and the portion of the beam that makes it through an object is used to generate an image of the object. In other words, it is the removal of some percentage of the original beam in some pattern due to scattering and absorption that allows one to generate an image of an object. In scattered radiation, the angle at which the radiation is redirected after an interaction within some object can be used to make inferences about the material properties of the object. The transmitted radiation is calculated as the uncollided source term and scattered radiation contributions are modeled using the Step Characteristic (SC) method. The SC method transforms the angular dependence of the transport equation

into a one dimensional equation by rotating the axis of the coordinate system along the direction of motion. The angular flux at one point along this line and the known source term can be used to solve for the angular flux anywhere along the characteristic line. The effects of uncollided and collided fluxes are then added and angular fluxes within the entire domain can be determined. The inverse models were composed of the steepest decent and conjugate gradient routines. The steepest decent method used the gradient of the objective function to determine the direction that minimizes the objective function. The conjugate gradient method minimizes the residual of the objective function and the direction of the updated guess for the parameters is determined by a linear interpolation between the old direction and the new gradient. Because the angular flux is calculated as a separate combination of the contributions due to uncollided and collided fluxes, the gradient must also be calculated in this manner. This method showed promise in its ability to correctly identify the location and cross sections of inclusion materials within a domain with some degree of error. The method did tend to smear the size and position of the inclusion. This is possibly an artifact of how the SC method calculates the angular fluxes along the characteristic lines.

Sternat[8] suggested to use diffusion theory to approximate neutral particle transport through a medium and constrained optimization to reconstruct the cross sections of two dimensional domains. The chosen optimization technique was Newton's method with the Armijo algorithm applied for step length control. The gradient and Hessian matrix were formed and substitution was used to form the Schur complement to avoid inverting the large Hessian system. The steepest decent method was also employed for comparison sake. The effects of reconstruction depth, resolution and number of experiments was investigated. The number of experiments generally had the effect of reducing the amount of iterations required for the reconstruction process

and increasing the accuracy of the final image. Single energy and multigroup models were studied and signal noise and bias were added to the synthetic measurement data in some of these models to better simulate real detection systems. The method was successful in its ability to reconstruct many domains, but a reconstruction depth limit of 6-7 characteristic lengths was determined. Some multigroup models were considered where energy dependent cross sections were reconstructed using illuminating sources with specific energies. Adding energy dependence, signal bias and noise increased the complexity of the imaging problem and as a result, the size of the domains that could be reconstructed was reduced. Using multiple experiments generally improved image quality in fewer iterations, but a point of diminishing returns was noticed where more experiments added little new information to the reconstruction and image quality showed little improvement.

Wu[9] suggested the idea of assuming a finite library of possible materials within the container. This then allowed for the use of a discrete optimization method where a discrete material indicator was proposed rather than the continuous cross section value. This method also employed a combined deterministic and stochastic methods for simulating neutron transport. First, inexpensive calculations are conducted using a gradient based deterministic search to get a general idea of the domain using a single energy group, a coarse spatial mesh or diffusion theory instead of transport theory. Next, cells that have similar cross sections or material properties are grouped together and interface regions that may contain multiple materials are identified. Third, the materials that possess similar properties to those identified in the initial deterministic search are placed in material candidate libraries. Fourth, additional constraints can be applied to the material regions to limit the candidate materials. Finally, an iterative optimization process is conducted where guesses for the material distributions are proposed and a high resolution transport forward model is used to compute the objec-

tive function. Because the optimization problem has been reformulated into a discrete problem, meaningful derivatives of the objective function can not be computed and a gradient based technique can not be used. Instead, the problem becomes one of combinatorial optimization where random numbers and some information learned from previous guesses are used to generate the new material distribution for the domain. The idea of reformulating the continuous optimization problem of determining cross sections into a discrete one of determining materials from a candidate library proved to be a novel approach to the cargo container imaging problem. However, this method generates a new interface region materials which contain some combination of two or more materials. Of course, these regions do not really exist and the size of these regions is a function of the resolution of the image. This method is also subject to the same limitations of the other techniques with regard to optically thick and highly scattering materials.

B. Radiation Imaging in Medical Physics

Optical tomography is a method of noninvasive diagnostics that is growing in interest in the medical field. In this process light is used to illuminate tissue and measurements are taken of the transmitted and scattered light. Because of the different scattering and absorption coefficients of fat, muscle, white matter, grey matter, etc., measurements of the transmitted and scattered light can be used to reconstruct an image that depicts the tissue sample. This imaging technique shows promise in applications which include breast and brain imaging for the detection of cancers, finger joint imaging for the diagnosis of arthritis and blood toxicology. Many numerical methods have been reviewed that use the photon transport equation as the forward model and some optimization techniques as the inversion method.

Klose[10–12] and Hielscher[10–15] have thoroughly investigated various numerical meth-

ods for imaging in the field of optical tomography. In most of these methods, the equation of radiative transfer (ERT) or transport equation is used as the basis of the forward model.[10–14] In some of these studies[10,13] the time dependent transport equation was considered, but in most cases the transport equation was simplified by the steady state assumption.[11,12,14] However, Hielscher and Bartel also proposed the time dependent diffusion equation as the model of light propagation in tissue.[15] The objective function took many different forms in these many studies. In all cases an objective function is formed as a least squares comparison between the measured and computed fluxes and it is used to quantify their difference. However, this least squares term is often normalized in different ways. The objective function is normalized by the measurements or detector readings of each source detector pair,[11,14] the predicted fluxes for each source detector pair,[10] a normalization constant that quantifies the confidence in the accuracy of a certain measurement,[12] or some other constant.[15] Abdoulaev, Ren and Hielscher proposed the addition of a regularization term to the objective function that imposes additional constraints.[13] This Tikhonov regularization functional is included in the objective function to help suppress high-frequency components of the optical properties because of the ill-posedness of the optical tomography problem.

Various different optimization techniques were applied in the studies by Hielscher and Klose. A one-dimensional line search using the golden section rule along the gradient direction was used to minimize the objective function in one paper.[10] The gradient of the objective function is determined by differentiating the adjoint transport equation which is accomplished by solving the transport equation in the reverse direction. The method displayed image resolution improvement as the number of iterations was increased. The test cases also displayed the trend that increasing the number of sources and the number of measurement points leads to image resolution

improvement, but there did exist a point of diminishing returns where more experiments and measurements adds little improvement to quality. Klose and Hielscher propose the use of a quasi-Newton method that uses the secant condition to approximate the Hessian system.[11] This specific quasi-Newton method is referred to as Broyden-Fletcher-Goldfard-Shanno method (BFGS) or the limited-memory Broyden-Fletcher-Goldfard-Shanno (lm-BFGS) and it is used to find the zeros of the gradient of the objective function and the minimum of the objective function. The Armijo or sufficient decrease line search was implemented with the quasi-Newton method to ensure that the method did not overshoot the minimum. The quasi-Newton methods were compared to a conjugate gradient optimization technique and a 2-10 fold reduction in the number of iterations to minimize the objective function was noticed. This was determined to be a result of the better search direction determined in the quasi-Newton method and inexact line search which required fewer evaluations of the forward model. The next method used lm-BFGS to determine the spatial distribution of fluorescent sources contained within biological tissue.[12] This method was employed along with an adjoint differentiation scheme that allows for the gradient of the objective function to be calculated during the computation of the forward model. This adjoint differentiation technique eliminated the need to evaluate the adjoint transport equation and decreases the number of computational operations. Experiments were conducted with a phantom and the trend of improved image depth resolution was noticed as the sources and detectors were positioned on more sides of the phantom was noticed. The idea of rescaling the measurements was also explored to reduce the likelihood of reconstruction errors created by coarse spatial grids, ray-effects or false scattering.

In a contrasting method, Abdoulaev, Ren and Hielscher[13] use an augmented Lagrangian approach where the inverse transport problem is formulated into a PDE-

constrained optimization problem. The new objective is to minimize a Lagrangian function that is then formed as the difference between the objective function, the constraints and a penalty term that measures how severely that the constraints are violated for the current guess of the optical properties and fluences. The gradient of this now augmented Lagrangian function is then computed to form the Karush-Kuhn-Tucker (KKT) optimality conditions and lm-BFGS is also employed to find the minimizer of the Lagrangian function. This PDE-constrained optimization technique showed a 10-30 fold decrease in computing time as compared with unconstrained optimization techniques and is highly parallelizable.

Another technique used a gradient based optimization technique that uses the lm-BFGS scheme extended to three dimensions.[14] Hexahedral and tetrahedral spacial meshes were examined on geometries similar to the human head. The limitations of the current implementation to only consider isotropic scattering was mentioned, but plans to add anisotropy were discussed.

Yet another technique considers two different inverse problems where n tissues types with n different optical properties are known to be contained within a medium.[15] In the first case, the volume fractions and locations of these tissues are unknown prior to the reconstruction, where as in the second case the volumes and tissue types are assumed to be known prior to the reconstruction but not the locations of the tissue types. Penalty factors for the two cases were applied to the objective function and a gradient-based iterative image reconstruction (GIIR) scheme was employed. Generally, the addition of the penalty terms limited the search space of the gradient method and led to improvements in image quality. The sensitivity of the reconstruction method with respect to the chosen hyperparameter was noted and the GIIR method with penalty terms was compared to the linear-perturbation approach.

Bangerth[16,17] and Joshi[17] proposed the idea of applying adaptive finite element

methods to the solution to inverse problems, with applications to optical tomography. In the first paper,[16] Bangerth outlines a general framework for the solution of inverse problems that utilizes adaptive finite element meshes. This framework formulates inverse problems as PDE-constrained optimization problems were a Newton-type method is to minimize a Lagrangian function comprised of an objective function and its constraints. A Tikhonov regularization term is included in the Lagrangian to suppress unwanted features in the solutions of the forward model and parallelization is considered throughout the optimization process. A line search technique is proposed that uses the norm of the residual of the optimality conditions as the merit function and the Schur complement method is used to avoid the inversion of the large Hessian matrix. This framework was applied to an optical tomography test case and a tumor of a centimeter in diameter was correctly identified and located. In addition, the adaptive mesh technique proved less computational expensive because of the ability to conduct initial iterations with a coarser mesh. In the second paper,[17] the specific florescence tomography problems was discussed more thoroughly as the process of illuminating a fluorescent dye with red light and the emitted infrared light is measured. The coupled photon diffusion equations were provided as the basis of the forward model. The Lagrangian formulation for the PDE-constrained optimization problem consisted of the least squares error function and Tikhonov regularization term, the constraints on the state equation and the parameter inequalities. A Gauss-Newton method is used where an approximation of the Hessian system is used to determine the search direction for the value of the updates of the parameters. The merit function based line search is then employed to determine an acceptable step length and the Schur complement method is employed to decompose the approximate Hessian matrix. The choice of the regularization functional is more explicitly explained as a function of the material property distribution and the goal reducing the regular-

ization parameter as the misfit decreases was presented. Again, the method proved capable of imaging a small tumor located in a lymph node in the groin of a Yorkshire Swine. The benefits of the adaptive meshes with respect to the reduction in overall computational time and to increase image resolution in the areas of concern was presented.

Roy and Sevick-Muraca[18] propose an active constrained truncated Newton method for optical tomography. In this method the coupled photon diffusion equations formulated in the frequency domain are solved using Galerkin finite elements in the forward model. The objective function is formed as the summation over all sources and all detectors of the product of the difference between the computed and measured fluxes and their respective complex conjugates. An active constrained method is then employed where the set of optical properties that lie between a lower and upper bound is first determined, then the subproblem of minimizing the objective function with respect to the remaining variables is approached as an unconstrained minimization problem. These upper and lower bounds are determined dynamically and the search space for the parameters is reduced with each iteration. A Newton method with trust region is then used to updated the free variables and a line search using both of the Wolfe conditions was employed. Reverse automatic differentiation (RAD) was included in the forward model to calculate the gradient of the error function without the need for an additional sweep. The active constrained Newton method was tested on a few two dimensional domains and the results were compared with those generated with an unconstrained gradient based method. The active constrained method was more efficient, accurate and less computationally expensive than the unconstrained gradient based technique. This was mainly attributed to the second order nature of the Newton method and the reduction in the search space for the parameters due to the constraints.

Hussein and Bowles[19] propose a method that uses the incoherently scattered radiation in imaging. The forward model is generated on a pixel by pixel basis and is comprised of an attenuation term for the beam before it enters the pixel of interest, a probability term that quantifies the likelihood of scattering and another attenuation term for the scattered beam. This forward model yields a detector response function that allows for duplicity of possible solutions based on whether the dominant interaction process is scattering or attenuation. Therefore, a numerical scheme for biasing the solution towards the dominant process is included to overcome this problem of multiple solutions. The source term in each pixel is then calculated in a sweeping manner along the source beam to the pixel of interest and then along the scattered direction to the measurement point. The imaging algorithm was tested on meter scale cargo containers where the detection of weapons was the goal. The reconstruction scheme using scattering radiation and the contraction method proved successful in reconstructing the many test cases examined. The scaling procedure used to modify the measurements improved the conditioning of the problem to allow for the reconstruction of noisy systems without further constraints or regularization. It also permitted the imaging of low density materials and thin objects and the method to be less sensitive to initial guesses.

C. Imaging Applied to DC-Resistivity and Magnetostatics

Haber and Ascher[20] suggest formulating the inverse problem as a constrained optimization problem where a preconditioner can be applied directly to the optimality conditions derived from a Newton-type method. The objective function is formed as the sum of the least squares difference and the Tikhonov regularization term. The Lagrangian is then formed as the sum of the objective function and the product of

the constraints and the Lagrange multiplier. The KKT system is the calculated as the first and second partial derivatives of the Lagrangian. The Hessian system is then permuted so that the blocks on the diagonal of the matrix dominate and a reduced Hessian is computed by decomposing the larger system. A preconditioner that approximates the inverse of the large permuted Hessian system is then used to avoid the computationally expensive inversion process. The suggested method was tested on DC-resistivity and magnetostatic problems. In both cases the proposed preconditioned symmetric quasi-minimal residual (PSQMR) method was compared to a preconditioned conjugate gradient (PCG) method. The number of iterations and the total number of floating point operations were used as metrics for the performance of the method. Generally, the PSQMR method required more iterations, but less floating point operations per iteration than the PCG method. The main advantage noticed by the PSQMR method was the elimination of the need to maintain conjugacy of the direction vectors to a high accuracy when using the conjugate gradient method.

CHAPTER III

TRANSPORT THEORY

A. Balance Equation

The behavior of a neutron population within some differential volume of interest can be described by the quantity of angular flux. Neutrons are produced or removed from a system in several ways and these processes can be described in a balance equation. This relationship is referred to as the neutron transport equation or Eq. (3.1):

$$\frac{1}{v(E)}\frac{\partial\psi(\vec{r},E,\vec{\Omega},t)}{\partial t} = -\vec{\Omega}\cdot\vec{\nabla}\psi(\vec{r},E,\vec{\Omega},t) - \Sigma_t(\vec{r},E)\psi(\vec{r},E,\vec{\Omega},t) + \int_0^{+\infty} dE' \int_{4\pi} d\Omega' \Sigma_s(\vec{r},E'\rightarrow E,\vec{\Omega}'\rightarrow\vec{\Omega})\psi(\vec{r},E',\vec{\Omega}',t) + S(\vec{r},E,\vec{\Omega},t) \tag{3.1}$$

Here, the term with the time derivative represents the change in the angular flux with respect to time. In this study of the cargo container imaging, the neutron population is assumed to be at steady state and this term in the neutron transport equation is zero. The second and third terms of Eq. (3.1) represent the mechanisms by which neutrons can be removed from a specific direction and energy group within a specific differential volume across a specific time interval. These loss terms represent how neutrons are removed due to streaming through and interaction within the differential volume. In imaging, the leakage term is important because of the ability to measure the leaked neutrons that exit the boundary of the domain. The fourth and fifth terms of Eq. (3.1) represents the mechanisms by which neutrons are introduced into the differential phase-space. These mechanisms are due to scattering within the

system and internal sources. Internal sources are especially interesting in cargo container imaging because the presence of internal sources will indicate whether or not SNM is confined within a container. This Thesis will only consider a single energy group analysis, the dependence of all of the terms on energy can also be removed. Now that we have applied some simplifying assumptions to the neutron transport equation, Eq. (3.2) results:

$$\vec{\Omega} \cdot \vec{\nabla}\psi(\vec{r},\vec{\Omega}) + \Sigma_t(\vec{r})\psi(\vec{r},\vec{\Omega}) = \int_{4\pi} d\vec{\Omega}'\Sigma_s(\vec{r},\vec{\Omega}' \rightarrow \vec{\Omega})\psi(\vec{r},\vec{\Omega}') + S(\vec{r},\vec{\Omega}) \text{ for } \vec{r} \in V, \vec{\Omega} \in S^2 \quad (3.2)$$

In addition, it is important to remember that the source term of Eq. (3.2) includes internal sources due to fissionable material contained within the differential volume and the contribution to the angular flux entering the differential volume from adjacent cells and the boundary of the domain. In the cargo container problem, sources are often imposed on the boundary of the domain to illuminate to contents of the domain. Therefore, the boundary conditions that describe these illuminating sources can be seen in Eq. (3.3):

$$\psi(\vec{r},\vec{\Omega}) = \psi^{inc}(\vec{r},\vec{\Omega}) \text{ for } \begin{cases} \vec{r} \in \partial V \\ \vec{\Omega} \cdot \vec{n}(\vec{r}) < 0 \end{cases} \quad (3.3)$$

where $\psi^{inc}(\vec{r},\vec{\Omega})$ is the angular flux imposed on the domain from an illuminating source such as a neutron source from an x-ray generator. Eq. (3.2) can then be rewritten in operator form to better represent the system of linear equations that result as the equation is discretized with respect to space, energy and angle:

$$\hat{\mathbf{L}}(\vec{r},\vec{\Omega})\psi(\vec{r},\vec{\Omega}) = \hat{\mathbf{S}}(\vec{r},\vec{\Omega})\psi(\vec{r},\vec{\Omega}) + \hat{\mathbf{Q}}(\vec{r},\vec{\Omega})\psi(\vec{r},\vec{\Omega}) + \hat{\mathbf{q}}(\vec{r},\vec{\Omega}) \tag{3.4}$$

Here, $\hat{\mathbf{L}}(\vec{r},\vec{\Omega})$, $\hat{\mathbf{S}}(\vec{r},\vec{\Omega})$ and $\hat{\mathbf{Q}}(\vec{r},\vec{\Omega})$ represent the loss, scattering and fission operators, respectively. $\hat{\mathbf{q}}(\vec{r},\vec{\Omega})$ denotes the source term from which includes the contribution to the angular flux within the domain due to internal volumetric sources represented by $S(\vec{r},\vec{\Omega})$ in Eq. (3.2) and the boundary source term represented by $\psi^{inc}(\vec{r},\vec{\Omega})$ in Eq. (3.3). Eq. (3.4) is valid everywhere within the domain and no fissionable materials are considered in the domains studied in this Thesis, so the fission term can be neglected. This relationship can only be used to determine the angular fluxes within the cargo container from a known incident neutron beam with a known energy range. If we combine the loss and scattering operators, we can further simplify the equation to Eq. (3.5):

$$\hat{\mathbf{A}}\boldsymbol{\Psi} = \hat{\mathbf{q}} \tag{3.5}$$

This new operator, $\hat{\mathbf{A}}$, seen in Eq. (3.5), is referred to as the transport operator.

B. Adjoint Transport Equation

The adjoint transport equation serves as the basis of the backward model. By solving the adjoint equation, the Lagrange multipliers or importances can be determined. Obtaining these importances is crucial to solving the constrained optimization problem. When two matrices are said to be adjoint, the relationship written in standard scalar product notation in Eq. (3.6) results:

$$(v, Au) = (A^{\dagger}v, u) \tag{3.6}$$

Here, u and v are vectors, A is a matrix and $A^{\dagger}$ is the adjoint matrix. In other words, the action that matrix A has on vector u initially has been removed and placed onto vector v. In the case where the A matrix is comprised of only real-valued quantities, the adjoint matrix $A^{\dagger}$ is equivalent to the transpose of the A matrix or A^{T}. The transport operator is real valued so its adjoint matrix is simply its transpose. The adjoint relationship can also be presented on a continuous equation prior to discretization. The simplified transport equation seen in Eq. (3.2) will be considered. The same general process is conducted for each term to determine its adjoint, so only the leakage term will be presented in this Thesis. This process is to multiply the term by a real-valued function, $f(\vec{r}, \vec{\Omega})$ and then integrate the term of the differential volume and the entire angle range. The first term is the leakage term, $\vec{\Omega} \cdot \vec{\nabla}\psi(\vec{r}, \vec{\Omega})$. For this term, integration by parts, $\vec{\nabla} \cdot (a\vec{b}) = a\vec{\nabla} \cdot \vec{b} + \vec{b} \cdot \vec{\nabla}a$, is required where $a = f$ and $\vec{b} = \vec{\Omega}\Psi$. Applying integration by parts to the leakage term, the Eq. (3.7) results in inner product notation:

$$(f; \vec{\nabla} \cdot [\vec{\Omega}\Psi]) = (1; \vec{\nabla} \cdot [f\vec{\Omega}\Psi]) - (\vec{\Omega}\Psi\cdot; \vec{\nabla}[f]) \tag{3.7}$$

where f is simply some real-valued function that depends on $\vec{r}$ and $\vec{\Omega}$). The divergence theorem can then be used on the first term in Eq. (3.7) to get Eq. (3.8):

$$\begin{aligned}\int_{4\pi} d\vec{\Omega} \int_{V} d^3r \vec{\nabla} \cdot (f(\vec{r}, \vec{\Omega})\vec{\Omega}\Psi(\vec{r}, \vec{\Omega})) = &\int_{\partial V} d^2r \int_{(2\pi)+} d\vec{\Omega}\vec{\Omega} \cdot \vec{n}(f(\vec{r}, \vec{\Omega})\Psi(\vec{r}, \vec{\Omega})) \\ &+ \int_{\partial V} d^2r \int_{(2\pi)-} d\vec{\Omega}\vec{\Omega} \cdot \vec{n}(f(\vec{r}, \vec{\Omega})\Psi(\vec{r}, \vec{\Omega}))\end{aligned} \tag{3.8}$$

And now the second term can be resolved into the term seen in Eq. (3.9):

$$-\int_{4\pi} d\vec{\Omega} \int_V d^3r \vec{\Omega}\Psi(\vec{r},\vec{\Omega})) \cdot \vec{\nabla} f(\vec{r},\vec{\Omega}) = -\int_{4\pi} d\vec{\Omega} \int_V d^3r \Psi(\vec{r},\vec{\Omega}) \vec{\nabla} \cdot (\vec{\Omega} f(\vec{r},\vec{\Omega})) \quad (3.9)$$

Finally, the full leakage term as seen in Eq. (3.10) results and this adjoint relationship tracks neutrons in the opposite or reverse direction:

$$\Big(f(\vec{r},\vec{\Omega}); div[\vec{\Omega}\Psi(\vec{r},\vec{\Omega})]\Big) = -\Big(\Psi(\vec{r},\vec{\Omega}); div[\vec{\Omega} f(\vec{r},\vec{\Omega})]\Big) + \langle \Psi, f \rangle_+ - \langle f, \Psi \rangle_- \quad (3.10)$$

This process can be conducted for all of the terms of the transport equation and similar results to Eq. (3.10) can be found for the interaction, scattering and source terms and the full adjoint transport equation or Eq. (3.11) results:

$$(f; \mathbf{A}\Psi) = (\Psi; \mathbf{A}^\dagger f) + \langle \Psi, f \rangle_+ - \langle f, \Psi \rangle_- \quad (3.11)$$

CHAPTER IV

OPTIMIZATION TECHNIQUES

A. Overview

Optimization in engineering is the process of deciding which is the best choice from a set of choices. Optimization involves minimizing some real valued cost function by systematically choosing real valued parameters from a set of allowable values. Optimization is a large field in applied mathematics with many different iterative approaches to achieve the final solution parameters. The best optimization algorithm depends on the specific problem being solved and the trade-offs between robustness, efficiency and accuracy of each method.

The general form of an optimization problem can be formulated as the minimization relationship seen in Eq. (4.1):

$$\min_{x \in R^n} f(x) \tag{4.1}$$

where x is the vector of variables or parameters, $f(x)$ is the scalar objective function or misfit that we want to minimize and R^n is the set of all possible real numbers to which the parameters belong. Based on knowledge of the problem or physical system that is being modeled, often times the searchable space for the parameters can be reduced to some subset of R^n. This reduction in the searchable space is accomplished through the application of constraints to the optimization process. The general form of a constrained optimization problem can be seen in Eq. (4.2):

$$\min_{x \in R^n} f(x) \text{ subject to } \quad c_i(x) = 0, i \in \mathcal{E} c_i(x) \geq 0, i \in \mathcal{I} \tag{4.2}$$

where $c_i(x)$ is the equality or inequality constraint imposed on $f(x)$, i is the index of the constraint, $\mathcal{E}$ is the set of all equality constraints and $\mathcal{I}$ is the set of all inequality constraints imposed on the minimization problem.

There are various classifications of problems that are encountered in engineering applications that govern which optimization techniques are best suited for the problem. First, optimization problems can be constrained or unconstrained as evidenced by Eq. (4.2). Constrained optimization problems have limitations that are imposed on the objective function or parameters to limit the number of possible solutions. For example, the parameters of cargo container transport represent the cross sections of the materials contained within the container. Since a negative cross section has no physical meaning, a logical constraint on this optimization problem would be to limit the possible parameters that the optimizer could propose to values greater than or equal to zero. Unconstrained optimization problems do not propose any limitations on the solution process. Generally, the more information that can be provided to the optimization routine, the more accurate and efficient the routine can be. However, the algorithms used in constrained optimization problems are generally much more complex than those for unconstrained techniques and require more computations to determine the next update for the parameters. The cargo container problem can be approached as either a constrained or unconstrained optimization problem. Second, optimization problems can be discrete or continuous. This classification can also be thought of as a constraint that is imposed on the solution parameters. The cargo container problem is a continuous optimization problem because cross sections are positive real valued numbers and are not limited to some discrete set. Third,

optimization problems can be stochastic or deterministic. This classification of the problems is rooted in the model that is used to represent the problem. Transport theory as presented in this document is deterministically modeled, but similar processes in particle physics can be stochastically modeled as well.

Just as there are many different classifications of optimization problems, there are also many different optimization algorithms or methods used to achieve the solution. These methods are all iterative, but they differ in the amount of information they require to achieve the solution. All optimization routines make use of the objective function and any constraints that exist to arrive at the solution parameters. Other optimization routines make use of the first and second derivatives of the objective function and constraints to solve the problem. Newton based methods generally require first and second derivative information, where as derivative-free methods do not. Derivative-free methods are applicable to a wider variety of optimization problems and require less computer storage, but require more computational time. Newton methods require less computational time, but also require more computer storage and are specific to problems where derivative information is accessible. Two methods are investigated in this document. The first is the Nelder-Mead method, a derivative-free method. The second is a Newton based method.

B. Nelder-Mead Method

The Nelder-Mead algorithm[5] for function minimization is an unconstrained, derivative-free optimization technique. It works by evaluating an objective function of n variables by a creating a simplex of n+1 vertices. The objective function is then evaluated for each of the combination of variables that form the vertices of the simplex, and the combination of these variables that leads to the largest and smallest value of the objective function, x_h and x_l, are stored. Three operations are then preformed based

on this largest value of the objective function which are reflection, expansion and contraction. In reflection, the centroid of the simplex defined by all of the vertices except the one with the largest objective function value, $\bar{x}$, is calculated. The vertex with the largest value is then reflected across the centroid using Eq. (4.3):

$$x^* = (1 + \alpha)\bar{x} - \alpha x_h \tag{4.3}$$

Here, α is a positive constant known as the reflection coefficient. The objective function is then evaluated at this new reflection point and if the resulting value lies between the maximum and minimum values of the original simplex, then this new point replaces x_h and a new simplex is formed. However, if this refection point yields a value of the objective function which is new minimum, then an expansion can be conducted to determine the amplification of magnitude of the reflection point based on Eq. (4.4):

$$x^{**} = \gamma x^* + (1 - \gamma)\bar{x} \tag{4.4}$$

Here, γ is a real number greater than one which is calculated based on the ratio of the distance from the centroid to the expanded point, x^{**}, to the distance from the centroid to the reflected point, x^*. Once the new expanded point has been determined, the objective function is evaluated at this point. If the evaluation of the expanded point is the new minimum, then the new simplex is formed by replacing x_h by x^{**}. Otherwise, the new simplex is formed by replacing x_h by x^*. In the last case where the objective function evaluated at the reflected point is larger than that of x_h, a contraction occurs described by Eq. (4.5):

$$x^{**} = \beta x_h + (1 - \beta)\bar{x} \tag{4.5}$$

Here, β is a real number between zero and one which is calculated based on the ratio of the distance from the centroid to the contracted point, x^{**}, to the distance from the centroid to the original point, x_h. In the contraction process, the value of the objective function evaluated at the initial point is compared with that of the reflected point and the larger of the two is redefined as x_h. If the contracted point yields an objective function that is greater than that associated with either the reflected or original points, then all of the original simplex vertices are averaged with x_l to generate the new simplex. Otherwise, the contracted point replaces x_h to form the next simplex.

The Nelder-Mead algorithm is a robust algorithm that is only capable of finding local minima. It only requires the evaluation of the objective function, which makes it applicable to optimization problems where the objective function is non-differentiable. It is also a very stable method that generally does not propose outrageous values for the parameters, because the gradient is not used to propose new guesses for the parameters. However, because only the objective function is evaluated, the method requires many iterations and much computational time to locate the solution.

C. Newton's Method

In optimization problems, Newton-based methods require the gradient and Hessian system to be calculated in order to generate an updated prediction of the parameters. Newton methods generally converge to the solution more rapidly than derivative free methods, but they are less reliable and do not guarantee convergence unless considered with a line search. In this Thesis, the inverse neutral particle transport

problem is tackled with Newton's method as a constrained optimization problem. In this constrained optimization problem, prior knowledge about neutral particle physics is applied to the objective function in the form of a constraint. Only one equality constraint will be applied to the objective function in this Thesis even though other constraints could be applied. Because of this, Eq. (4.2) can be simplified to consider only equality constraints and the general formulation of the constrained optimization problem becomes Eq. (4.6):

$$\min_{x\in\Omega} f(x) \text{ where } \Omega = \{x|c_i(x) = 0, i \in \mathcal{E}\} \tag{4.6}$$

Here, Ω is the acceptable domain space of possible parameter combinations defined by the set of imposed equality constraints, $\mathcal{E}$. In the case of the inverse neutral particle transport problem, a set of equality constraints is applied to the optimization problem that ensures that the transport equation is satisfied for every angular flux at every angle and spatial coordinate. A relationship known as the Lagrangian function can be defined as the combination of the objective function and its constraints or Eq. (4.7):

$$\mathcal{L}(x, \lambda) = f(x) + \sum_{i\in\mathcal{E}} \lambda_i c_i(x) \tag{4.7}$$

Here, λ_i is the importance factor and $\mathcal{L}$ is the Lagrangian. Also, it can be seen that the objective function is only dependent on x, where as the Lagrangian is dependent on both x and λ. This evidences the fact that the objective function requires only the evaluation of the forward model or transport equation and the Lagrangian requires this computation plus the evaluation of the backward model or adjoint transport equation. This is because the Lagrangian function required that the

Lagrange multipliers, λ_i, be computed. These Lagrange multipliers track the neutral particles in the reverse direction and they contain information about the direction and magnitude of the computed angular fluxes. They also serve as a weighting function that determines how severely each constraint is applied to the parameters.

1. Gradient and Hessian System

Now that the constrained optimization problem has been presented, the gradient and Hessian systems can be computed as the first and second partial derivatives of the Lagrangian function with respect to the coupled independent variables. In inverse problems, these variables are generally the input and output variables of physical model and importances or adjoint variables. The specific independent variables of the inverse neutral particle transport problem are presented in the next section of this Thesis. Since the goal of the minimization process is to determine the minimum of the objective function while still satisfying the constraints, the value of the gradient of the Lagrangian function at this minimum is zero or $\vec{\nabla}\mathcal{L} = 0$. Therefore, the gradient of the Lagrangian function also known as the Karush - Kuhn - Tacker (KKT) optimality conditions[13] seen in Eq. (4.8) result:

$$\mathbf{F}(\mathbf{y}) = \begin{pmatrix} \frac{\partial \mathcal{L}}{\partial x} \\ \frac{\partial \mathcal{L}}{\partial \lambda} \end{pmatrix} = \begin{pmatrix} 0 \\ \vdots \\ 0 \end{pmatrix} \tag{4.8}$$

Here, x again represents the input and output variables of the transport model, λ represents the importances or adjoint variables and y is one vector that combines both x and λ. The Hessian operator can then be computed as the second derivative of the Lagrangian with respect to each the variables and importances or Eq. (4.9):

$$\mathbf{H} = \begin{pmatrix} \partial_{xx}\mathcal{L} & \partial_{\lambda x}\mathcal{L} \\ \partial_{x\lambda}\mathcal{L} & \partial_{\lambda\lambda}\mathcal{L} \end{pmatrix} \tag{4.9}$$

Now that the gradient and Hessian terms have been presented, Newton's method can be used to determine the update values for the parameters of interest. These parameters of interest now include both the input and output variables of the transport model, x, and the importances or adjoint variables, λ. So a new vector $\delta\mathbf{y}$ is introduced as a update vector that contains all of the variables and importances and the general equation that is solved in Newton's method to calculate this update vector is Eq. (4.10):

$$\delta\mathbf{y} = -\mathbf{H^{-1}F(y^k)} \tag{4.10}$$

Here, $\mathbf{H}$ is the Hessian matrix and $\mathbf{F}$ is the gradient vector. The change in the vector of variables can then be used to update the vector of variables or Eq. (4.11) where k represents the Newton iteration index:

$$\mathbf{y}^{k+1} = \mathbf{y}^k + \delta\mathbf{y} \tag{4.11}$$

Newton's method is iterated until $||F(y^k)|| < \epsilon$, where ϵ is a user-defined tolerance.

2. Schur Complement

The Schur Complement is a technique that recognizes that the Hessian system seen in Eq. (4.9) is composed of multiple smaller matrices or blocks and uses substitution to solve for each of the updated unknowns that are contained in $\delta\mathbf{y}$ individually. This

method is less computationally expensive because it requires that matrices only as large as the blocks of the Hessian be stored and inverted as supposed to storing and inverting the full Hessian matrix. The Schur complement method can be implemented on any linear system that consists of blocks.

3. Line Search

When using Newton's method, it is common to use a line search method to determine an acceptable step length or fraction of the update direction vector to apply to the vector of parameters. This is done because using the full Newton step length can lead to divergence especially when the initial guess is far from the solution and the objective function has a minimum that is difficult to locate. Divergence can occur because often, a full step in the update direction can stride beyond the minimum and this can yield a worse guess than in the previous iteration. The general equation that displays how the parameters are updated in Newton's method with the additional damping parameter, α, can be seen in Eq. (4.12):

$$\mathbf{x}^{k+1} = \mathbf{x}^k + \alpha^k \delta \mathbf{x}^k \tag{4.12}$$

The goal of the line search is solely to determine an acceptable value for this damping parameter that yields an improved guess for the parameters. This damping parameter is generally determined by computing two conditions. These two conditions are collectively referred to as the Wolfe conditions. Separately, the first condition is referred to as the sufficient decrease or Armijo condition and the second condition is referred to as the curvature condition. Both of these conditions are more fully explained in the following sections. In practice, an initial value for α of unity is attempted first and the two conditions are checked. If these conditions are satisfied,

then the current step length is accepted, otherwise then value of alpha is reduced and the conditions are recomputed. This process is repeated until the conditions are satisfied or some minimum step length specified by the developer is achieved. This minimum step length was chosen to be 10^{-3} and the step length was reduced by a constant 1.5 with every iteration for this Thesis. These values were chosen because the value of the Lagrangian function changes only minimally with each successive guess when a step size of this magnitude is applied and 1.5 was chosen because reducing the step size by half each time was thought to reduce it too rapidly.

a. Sufficient Decrease Condition

The sufficient decrease condition evaluates the Lagrangian and gradient at the current Newton iteration and compares these values with the Lagrangian evaluated at the next iteration as seen in Eq. (4.13):

$$\mathcal{L}(\mathbf{x}_k+\alpha\delta\mathbf{x}) \leq \mathcal{L}(\mathbf{x}_k) + c_1\alpha\nabla\mathcal{L}(\mathbf{x}_k)^T\delta\mathbf{x} \tag{4.13}$$

Here, $\mathcal{L}(\mathbf{x}_k+\alpha\delta\mathbf{x})$ is the Lagrangian function evaluated at the possible next Newton step, $\mathcal{L}(\mathbf{x}_k)$ is the Lagrangian function evaluated at the current Newton step, c_1 is a constant that was set to 10^{-4} in the results in this Thesis, α is the fraction of the update direction vector to be added to the current Newton iteration, $\delta\mathbf{x}$ is the update direction vector and $\nabla\mathcal{L}(\mathbf{x}_k)^T$ is the transpose of the gradient of the Lagrangian function evaluated at the current Newton iteration. The sufficient decrease condition ensures that the value of the Lagrangian function has been sufficiently reduced between successive iterations.

b. Curvature Condition

The curvature condition evaluates the gradient at the current Newton iteration and compares it with the gradient of the Lagrangian evaluated at the next iteration as seen in Eq. (4.14):

$$\nabla\mathcal{L}(\mathbf{x}_k+\alpha\delta\mathbf{x})^T\delta\mathbf{x} \geq c_2\nabla\mathcal{L}(\mathbf{x}_k)^T\delta\mathbf{x} \tag{4.14}$$

Here, $\nabla\mathcal{L}(\mathbf{x}_k+\alpha\delta\mathbf{x})^T$ is the gradient of the Lagrangian function evaluated at the possible next Newton step and c_2 is a constant that was set to 0.9 in the results in this Thesis. The curvature condition ensures that the slope of the Lagrangian function has been sufficiently reduced between successive iterations. Satisfying both of these conditions generally implies that the updated parameters represent a better approximation of the true parameters.

Both the sufficient decrease and curvature conditions served as the basis of the line search used for all of the test cases explored in this Thesis except for in Example 14 or the optical thickness study with scattering. These two conditions were applied to Newton's method because they are a common line search that is often used to ensure that Newton's method does not overshoot the solution parameters.

c. Merit Function

Another technique that can be employed to overcome the challenges presented when trying to satisfy the conditions of the line search is a merit function. This merit function provides a measure of how severely the constraints are violated within the line search with the addition of a penalty function. The ℓ_1 penalty function seen in Eq. (4.15) was explored in this Thesis:

$$\phi(\mathbf{x};\mu) = \mathcal{L}(\mathbf{x}) + \mu \sum_{\mathbf{i}\in\mathcal{E}} |\mathbf{c_i}(\mathbf{x})| \tag{4.15}$$

Here, $\phi(\mathbf{x};\mu)$ is the merit function and μ is the penalty parameter. Again, since only equality constraints are considered, the reformulation of the line search with the merit function only considers equality constraints. The $\updownarrow_1$ penalty function is not differentiable because the absolute value of the constraints is taken, so a true gradient of the merit function can not be computed. However, a directional derivative, $D(||x||_1;\delta x)$, can be computed as seen in Eq. (4.16):

$$\mathbf{D}(||\mathbf{x}||_\mathbf{1};\delta\mathbf{x}) = \sum_{\mathbf{i}|\mathbf{x_i}<\mathbf{0}} -\delta\mathbf{x_i} + \sum_{\mathbf{i}|\mathbf{x_i}>\mathbf{0}} \delta\mathbf{x_i} + \sum_{\mathbf{i}|\mathbf{x_i}=\mathbf{0}} |\delta\mathbf{x_i}| \tag{4.16}$$

Here, x_i is the vector of variables and δx_i is the update direction vector. This directional derivative can then be used in the sufficient decrease condition as presented in Eq. (4.17):

$$\phi(\mathbf{x}+\alpha\delta\mathbf{x};\mu) \leq \phi(\mathbf{x};\mu) + \mathbf{c_1}\alpha\mathbf{D}(\phi(\mathbf{x};\mu);\delta\mathbf{x}) \tag{4.17}$$

This line search technique was used for Example 14 or the optical thickness problem with scattering. This was done because it was noticed that the values of the cross sections of the inclusion contributed only slightly to the value of the objective function. This meant that these cross section values were less significant in the reconstruction process than the cross sections of the surrounding material. The Newton's method quickly began to proposed values for these cross sections that greatly deviated from the true values when the sufficient decrease and curvature condition line search was applied. Therefore, the alternative merit function line search was employed.

d. Additional Checks

A negative cross section backtrack method was also applied that allowed the minimum step length value to be 10^{-4} so that Newton's method would be less likely to propose negative values for the cross sections. Along these same line of thought, a backtrack was also applied that reduced the step length if the proposed scattering cross section was larger than the proposed total cross section for any region. This check also allowed the step length to be reduced to values less than 10^{-4}.

CHAPTER V

INVERSE TRANSPORT PROBLEM

A. Objective Function

In the case of noninvasive cargo container imaging, the only data that are available are outgoing angular flux measurements. Therefore, the model of radiation transport is used to make predictions for these outgoing angular fluxes and a metric to quantify the difference between the computed and measured fluxes is required. This measure of the difference between the computed and measured angular fluxes is the objective function or misfit. This function is generally computed using a least squares technique where the difference between the measured and computed fluxes is squared to treat positive and negative flux differences equally. All of the squared flux differences are then summed and then divided by two to yield a single value for the objective function. Reducing the magnitude of this value should lead to a better material map and is the basis for most optimization techniques. The expression that describes the misfit in the inverse transport problem is given in Eq. (5.1):

$$f = \tfrac{1}{2} \int_{\partial V^m} d^2r \int_{\vec{\Omega}\cdot\vec{n}>0} d\vec{\Omega} |\vec{\Omega}\cdot\vec{n}| \left(\psi(\vec{r},\vec{\Omega}) - \tilde{\psi}(\vec{r},\vec{\Omega})\right)^2 \tag{5.1}$$

Here, f is the objective function, ∂V^m is the subset of the cargo boundary where measurements are taken, $\vec{n}$ the outward normal unit vector, ψ is the computed angular flux and $\tilde{\psi}$ is the measured angular flux. This misfit function written in discrete notation in Eq. (5.2) will serve as the metric to determine the quality of the material map at every iteration for every simulation studied in this Thesis:

$$\boldsymbol{\Delta} = \tfrac{1}{2}(\boldsymbol{\Psi} - \tilde{\boldsymbol{\Psi}})^T \mathbf{M} (\boldsymbol{\Psi} - \tilde{\boldsymbol{\Psi}}) \tag{5.2}$$

Here, $\tilde{\boldsymbol{\Psi}}$ and $\boldsymbol{\Psi}$ are the vectors of measured and computed angular fluxes for every spatial coordinate, angle and energy group, respectively. The matrix $\mathbf{M}$ is a filtering matrix that only extracts the outgoing angular fluxes that lie on the boundary where measurements were taken. This is done again because for noninvasive imaging, the only measurements that are accessible lie on some portion of the boundary.

B. Formulation of Lagrangian

As discussed in the section on optimization, the Lagrangian function is comprised of the objective function and its constraints. In this inverse transport problem, the only constraint that is applied to the objective function is that the proposed cross sections must produce angular fluxes that satisfy the transport equation. The Lagrangian can be defined more specifically to the inverse transport problem as seen in Eq. (5.3):

$$\mathcal{L}(\boldsymbol{\Psi}, \lambda, \boldsymbol{\Sigma}) = \tfrac{1}{2}(\boldsymbol{\Psi} - \tilde{\boldsymbol{\Psi}})^T \mathbf{M} (\boldsymbol{\Psi} - \tilde{\boldsymbol{\Psi}}) + \lambda^T (\mathbf{A}\boldsymbol{\Psi} - \mathbf{q}) \tag{5.3}$$

Here, $\tilde{\boldsymbol{\Psi}}$ and $\boldsymbol{\Psi}$ are the vectors of measured and computed angular fluxes, $\mathbf{M}$ is a filtering matrix that extracts only the outgoing angular fluxes that lie on the boundary where measurements were taken, λ is the importance function or the adjoint angular flux vector, $\mathbf{A}$ is the transport operator and $\mathbf{q}$ is the external volumetric and surface source term of the transport equation. $\boldsymbol{\Sigma}$ is the vector of parameters or cross sections and this term can be found within the transport operator, $\mathbf{A}$. Again, in order to minimize the Lagrangian, the transport equation, $(\mathbf{A}\boldsymbol{\Psi} - \mathbf{q})$, must be fulfilled.

C. Optimality Conditions

The optimality conditions form the gradient or first derivative of the Lagrangian with respect to the vector of angular fluxes, the vector of adjoint fluxes and the vector of cross sections. These optimality conditions determine the direction of the steepest ascent of the Lagrangian function and the location of the minimum of the Lagrangian will be found when all these conditions are zero. When the derivative of the Lagrangian functional is taken with respect to the variable vectors, a dimension is added and the optimality conditions are vector quantities. The derivative of the Lagrangian with respect to the vector of angular fluxes is Eq. (5.4):

$$\frac{\partial \mathcal{L}}{\partial \boldsymbol{\Psi}} = \mathbf{M}(\boldsymbol{\Psi} - \tilde{\boldsymbol{\Psi}}) + \mathbf{A}^T \lambda = \begin{pmatrix} 0 \\ \vdots \\ 0 \end{pmatrix} \tag{5.4}$$

Here, it can be noted that the filtering matrix, $\mathbf{M}$, and the adjoint transport operator matrix, $\mathbf{A}^T$, are present. Conventionally, the variable vectors of the Lagrangian equation and the optimality conditions are presented as column vectors. In this term, the filtering matrix extracts the measured flux differences and the result is summed with the transport operator which models all the radiation interaction processes weighted according to their computed importances. This term represents the gradient of the objective function and the constraints with respect to the angular fluxes. The derivative of the Lagrangian with respect to the vector of adjoint angular fluxes is Eq. (5.5):

$$\frac{\partial \mathcal{L}}{\partial \lambda} = \mathbf{A}\boldsymbol{\Psi} - \mathbf{q} = \begin{pmatrix} 0 \\ \vdots \\ 0 \end{pmatrix} \tag{5.5}$$

When the derivative of the Lagrangian is taken with respect to the importance function, the result is the transport equation. This result is true for all optimization problems. The derivative of the Lagrangian with respect to the vector of cross sections is Eq. (5.6):

$$\frac{\partial \mathcal{L}}{\partial \boldsymbol{\Sigma}} = \lambda^T \frac{\partial \mathbf{A}}{\partial \boldsymbol{\Sigma}} \boldsymbol{\Psi} = \begin{pmatrix} 0 \\ \vdots \\ 0 \end{pmatrix} \tag{5.6}$$

The only place that the cross sections are found in the Lagrangian are in the transport operator. Therefore, the derivative of the transport operator matrix with respect to the vector of cross sections yields a three dimensional tensor or a vector of two dimensional matrices. In other words, there should exist a collection of N matrices based on the number of cross sections each with a row dimension with a length equivalent to the length of the importance function and a column dimension with a length equivalent to the length of the angular flux vector. In this term, the contribution to the transport equation constraint attributed to each reconstructed cross section is isolated in the $\frac{\partial \mathbf{A}}{\partial \boldsymbol{\Sigma}}$ term. In summary, the full gradient vector, $\mathbf{F}$, is Eq. (5.7):

$$\mathbf{F} = \begin{pmatrix} \mathbf{M}(\boldsymbol{\Psi} - \tilde{\boldsymbol{\Psi}}) + \mathbf{A}^T \\ \mathbf{A}\boldsymbol{\Psi} - \mathbf{q} \\ \lambda^T \partial_{\boldsymbol{\Sigma}} \mathbf{A}\boldsymbol{\Psi} \end{pmatrix} \tag{5.7}$$

D. Hessian Matrix

Newton's method requires the formulation of the Hessian matrix, **H**, in addition to the gradient of the Lagrangian function. The requirement is because the $\nabla\mathcal{L} = \vec{0}$ is a nonlinear problems that must be solved with an iterative method. The optimality conditions form a nonlinear problem because in each term a product of the variables of the linear system or their derivatives can be found. Therefore, a root finding method is needed to solve this nonlinear system and Newton's method was chosen because of the low computational time and number of iterations required to find the solution. The Hessian matrix is formulated by taking a derivative of the optimality conditions with respect to the angular flux, adjoint flux and cross section vectors. In other words, this large matrix represents all of the combinations of the second partial derivative of the Lagrangian equation with respect to each of the variable vectors or Eq. (5.8):

$$\mathbf{H} = \begin{pmatrix} \partial_{\Psi\Psi}\mathcal{L} & \partial_{\lambda\Psi}\mathcal{L} & \partial_{\Sigma\Psi}\mathcal{L} \\ \partial_{\Psi\lambda}\mathcal{L} & \partial_{\lambda\lambda}\mathcal{L} & \partial_{\Sigma\lambda}\mathcal{L} \\ \partial_{\Psi\Sigma}\mathcal{L} & \partial_{\lambda\Sigma}\mathcal{L} & \partial_{\Sigma\Sigma}\mathcal{L} \end{pmatrix} \tag{5.8}$$

Here, the rows of the Hessian represent each of the optimality conditions and all have the same first derivatives. The columns of the Hessian represent the process of taking the derivative of the optimality conditions with respect to each of the variable vectors and all have the same second derivatives. From looking at this matrix, we

can predict that the Hessian matrix should be symmetric because the below diagonal derivatives are the same as the above diagonal derivatives taken in the opposite order. The results of evaluating the derivatives of the Lagrangian for the inverse transport problem are provided in Eq. (5.9):

$$\mathbf{H} = \begin{pmatrix} \mathbf{M} & \mathbf{A}^T & \partial_\Sigma \mathbf{A}^T \lambda \\ \mathbf{A} & \mathbf{0} & \partial_\Sigma \mathbf{A} \boldsymbol{\Psi} \\ \lambda^T \partial_\Sigma \mathbf{A} & \boldsymbol{\Psi}^T \partial_\Sigma \mathbf{A}^T & \mathbf{0} \end{pmatrix} \tag{5.9}$$

This equation does display symmetry where the below diagonal sub-matrices are simply the transposes of the above diagonal sub-matrices. Because of the ambiguity associated with taking the transpose of a vector of matrices for the $\partial_\Sigma \mathbf{A}^T$ term, the matrix has been rewritten and given indices in Eq. (5.10):

$$\mathbf{H} = \begin{pmatrix} \mathbf{M}_{i,j} & \mathbf{A}_{j,i} & \sum_j \left(\frac{\partial}{\partial \Sigma_k} \mathbf{A}_{j,i} \right) \lambda_j \\ \mathbf{A}_{i,j} & \mathbf{0}_{i,j} & \sum_i \left(\frac{\partial}{\partial \Sigma_k} \mathbf{A}_{i,j} \right) \boldsymbol{\Psi}_i \\ \sum_j \lambda_j^T \left(\frac{\partial}{\partial \Sigma_k} \mathbf{A}_{i,j} \right) & \sum_i \boldsymbol{\Psi}_i^T \left(\frac{\partial}{\partial \Sigma_k} \mathbf{A}_{j,i} \right) & \mathbf{0}_{k,k} \end{pmatrix} \tag{5.10}$$

Here, the index, i, corresponds to the index of the angular flux vector, the index, j, corresponds to the index of the adjoint flux vector and the index, k, corresponds to the parameter vector. The transpose of the transport operator simply swaps the indices of this two dimensional matrix. The product of a flux and the partial derivative of the transport matrix with respect to the vector of cross sections can be clearly represented as the dot product of the flux and the partial of the transport operator over the flux index represented in summation notation as shown in Eq. (5.10). The system of equations that is solved in Newton's method can be seen in Eq. (5.11):

$$\begin{pmatrix} \mathbf{M} & \mathbf{A}^T & \partial_\Sigma \mathbf{A}^T \lambda \\ \mathbf{A} & \mathbf{0} & \partial_\Sigma \mathbf{A}\boldsymbol{\Psi} \\ \lambda^T \partial_\Sigma \mathbf{A} & \boldsymbol{\Psi}^T \partial_\Sigma \mathbf{A}^T & \mathbf{0} \end{pmatrix} \begin{pmatrix} \delta\boldsymbol{\Psi} \\ \delta\lambda \\ \delta\boldsymbol{\Sigma} \end{pmatrix} = - \begin{pmatrix} \mathbf{M}(\boldsymbol{\Psi} - \tilde{\boldsymbol{\Psi}}) + \mathbf{A}^T \\ \mathbf{A}\boldsymbol{\Psi} - \mathbf{q} \\ \lambda^T \partial_{\boldsymbol{\Sigma}} \mathbf{A}\boldsymbol{\Psi} \end{pmatrix} \tag{5.11}$$

E. Schur Complement Method

Newton's method requires building and inverting the large Hessian system. This process can require large amounts of memory and computational time. The Schur complement of the Hessian system was found to alleviate some of these memory and time problems. The Schur complement method simply recognizes that the Hessian system is block diagonal and it uses substitution to solve for the change in each of the variables of the nonlinear system independently. This process gains a computational edge over the Hessian method, because the transport operator is the largest matrix that is formed which alleviates some of the memory problems of building the full Hessian. This Schur complement still requires the transport operator to be inverted several times, but since the full Hessian does not need to be inverted, this method still save computational time. Based on Eq. (5.11), the Hessian system can be deconstructed into three basic equations. The quantity that we desire to update first is the cross sections, so substitution will be used to eliminate the $\delta\boldsymbol{\Psi}$ and $\delta\lambda$ from (5.11). Evaluating the second row of the Hessian matrix yields Eq. (5.12):

$$\mathbf{A}\delta\boldsymbol{\Psi} + \partial_{\boldsymbol{\Sigma}} \mathbf{A}\boldsymbol{\Psi}\delta\boldsymbol{\Sigma} = \mathbf{q} - \mathbf{A}\boldsymbol{\Psi} \tag{5.12}$$

Solving this equation for $\delta\boldsymbol{\Psi}$, Eq. (5.13) result:

$$\delta\mathbf{\Psi} = \mathbf{A^{-1}}(\mathbf{q} - \mathbf{A\Psi} - \partial_{\mathbf{\Sigma}}\mathbf{A\Psi}\delta\mathbf{\Sigma}) \tag{5.13}$$

Evaluating the first row of the Hessian system, Eq. (5.14) results:

$$\mathbf{M}\delta\mathbf{\Psi} + \mathbf{A^T}\delta\lambda + \partial_{\mathbf{\Sigma}}\mathbf{A}\lambda\delta\mathbf{\Sigma} = -\mathbf{M}(\mathbf{\Psi} - \tilde{\mathbf{\Psi}}) - \mathbf{A^T}\lambda \tag{5.14}$$

Solving this equation for $\delta\lambda$, Eq. (5.15) results:

$$\delta\lambda = \mathbf{A^{-T}}(-\mathbf{M}(\mathbf{\Psi} - \tilde{\mathbf{\Psi}}) - \mathbf{A^T}\lambda - \mathbf{M}\delta\mathbf{\Psi} - \partial_{\mathbf{\Sigma}}\mathbf{A}\lambda\delta\mathbf{\Sigma}) \tag{5.15}$$

Eq. (5.13) can be substituted into Eq. (5.15) and Eq. (5.16) results:

$$\delta\lambda = \mathbf{A^{-T}}(-\mathbf{M}(\mathbf{\Psi} - \tilde{\mathbf{\Psi}}) - \mathbf{A^T}\lambda - \mathbf{MA^{-1}}(\mathbf{q} - \mathbf{A\Psi} - \partial_{\mathbf{\Sigma}}\mathbf{A\Psi}\delta\mathbf{\Sigma}) - \partial_{\mathbf{\Sigma}}\mathbf{A}\lambda\delta\mathbf{\Sigma}) \tag{5.16}$$

The third row of the Hessian system can now be evaluated and the result is Eq. (5.17):

$$\lambda^{\mathbf{T}}\partial_{\mathbf{\Sigma}}\mathbf{A}\delta\mathbf{\Psi} + \mathbf{\Psi^T}\partial_{\mathbf{\Sigma}}\mathbf{A}\delta\lambda = -\lambda^{\mathbf{T}}\partial_{\mathbf{\Sigma}}\mathbf{A\Psi} \tag{5.17}$$

Eqs. (5.13) and (5.16) can now be substituted into Eq. (5.17) and the result is Eq. (5.18):

$$\mathbf{\Psi^T}\partial_{\mathbf{\Sigma}}\mathbf{A}\mathbf{A^{-T}}(-\mathbf{M}(\mathbf{\Psi}-\tilde{\mathbf{\Psi}})-\mathbf{A^T}\lambda-\mathbf{M}\mathbf{A^{-1}}(\mathbf{q}-\mathbf{A}\mathbf{\Psi}-\partial_{\mathbf{\Sigma}}\mathbf{A}\mathbf{\Psi}\delta\mathbf{\Sigma})-\partial_{\mathbf{\Sigma}}\mathbf{A}\lambda\delta\mathbf{\Sigma})+$$
$$\lambda^{\mathbf{T}}\partial_{\mathbf{\Sigma}}\mathbf{A}\mathbf{A^{-1}}(\mathbf{q}-\mathbf{A}\mathbf{\Psi}-\partial_{\mathbf{\Sigma}}\mathbf{A}\mathbf{\Psi}\delta\mathbf{\Sigma})=-\lambda^{\mathbf{T}}\partial_{\mathbf{\Sigma}}\mathbf{A}\mathbf{\Psi} \tag{5.18}$$

This equation can now be solved for the $\delta\mathbf{\Sigma}$. The terms that contain $\delta\mathbf{\Sigma}$ are grouped together to form a square matrix that will be referred to as the $\mathbf{S}$ matrix or Schur complement. The terms that do not contain a $\delta\mathbf{\Sigma}$ are grouped together to form a vector that will be referred to as the $\mathbf{U}$ vector. Therefore, the systems of linear equations is reformulated in the form of $\mathbf{S}\delta\mathbf{\Sigma}=\mathbf{U}$. The terms that form the $\mathbf{S}$ matrix are displayed in Eq. (5.19):

$$\mathbf{S}=\lambda^{\mathbf{T}}\partial_{\mathbf{\Sigma}}\mathbf{A}\mathbf{A^{-1}}\partial_{\mathbf{\Sigma}}\mathbf{A}\mathbf{\Psi}+\mathbf{\Psi^T}\partial_{\mathbf{\Sigma}}\mathbf{A}\mathbf{A^{-T}}(\mathbf{M}\mathbf{A^{-1}}\partial_{\mathbf{\Sigma}}\mathbf{A}\mathbf{\Psi}-\partial_{\mathbf{\Sigma}}\mathbf{A}\lambda) \tag{5.19}$$

The terms that form the $\mathbf{U}$ vector can be seen in Eq. (5.20):

$$\mathbf{U}=-\lambda^{\mathbf{T}}\partial_{\mathbf{\Sigma}}\mathbf{A}\mathbf{A^{-1}}\mathbf{q}+\mathbf{\Psi^T}\partial_{\mathbf{\Sigma}}\mathbf{A}(\lambda+\mathbf{A^{-T}}\mathbf{M}(\mathbf{A^{-1}}\mathbf{q}-\tilde{\mathbf{\Psi}})) \tag{5.20}$$

Once $\delta\mathbf{\Sigma}$ has been found, then the updates for the other parameters, $\delta\mathbf{\Psi}$ and $\delta\lambda$, can be found by solving Eqs. (5.14) and (5.15) with these these values of $\delta\mathbf{\Sigma}$.

CHAPTER VI

RESULTS AND DISCUSSION

A. Pure Absorber Problems

In this section, the ability of Newton's method to identify the material properties of some simple pure absorber problems with only a single experiment will be explored. Example 1 presents the minimization problem that Newton's method is trying to solve. The effects of the number and position of the illuminating sources used to scan the domain is also examined in example 1. Example 2 serves as a comparison between Newton's method and the derivative-free Nelder-Mead method. The convergence process as Newton's method get closer to the actual solution is also present in example 2 for a problem with two inclusions. Example 3 displays the ability of Newton's method to reconstruct a more complex four-strip domain. Finally, Example 4 presents the effects of applying illuminating sources on different sides of a four-region domain.

1. Example 1 - Misfit Surfaces

The first example problem is a simple model with two homogeneous domains each encompassing half of the geometry and it can be seen in figure VI-1. The two regions of the model are divided vertically down the center of the model. A complete description of the problem layout can be seen in Table VI-I. This two-parameter problem allows the objective function surface to be plotted as function of the two total cross sections of the two regions. The surface plots of the objective function will display the challenges associated with inverse transport because the finding the minimum of the objective function is not a trivial task.

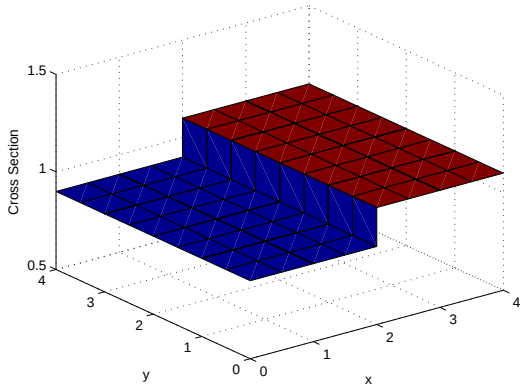

Fig. VI-1.: Two Parameter Problem - True Cross Section Distribution.

Tables similar to Table VI-I will be used to describe the input parameters used to define the model geometry, reconstruction parameters and boundary sources used in each example. An angular quadrature of S_8 was maintained for all of the example problems in this Thesis because it provided a reasonable compromise between sufficient angular resolution and reasonable computing times. Only square domains were examined in this thesis and the domain size is identified in either centimeters or number of mean free paths. The number of material regions specifies how many distinct materials regions exist in true geometry of the example problem. For example, there are two distinct material regions in this problem. The material mesh specifies the number of possible distinct material regions. In example 1, a total of sixteen distinct materials could be modeled and independently reconstructed. However, the domain was assumed to consist of only two material regions so that the misfit surface could be plotted. The flux mesh specified the total number of cells used in the angular flux computation. This mesh is generally finer than the material mesh to increase model accuracy. The number of search parameters specifies the number of independent cross sections that are to be reconstructed in the optimization process.

The actual cross sections of the various material regions specify the values of the true solution which are used to obtain the the reference solution and then discarded before the reconstruction begins. In this problem, the objective function surface was generated by evaluating the misfit function at 625 different parameter combinations. The parameter combinations were generated by varying the cross sections from 50 to 200% of their actual values in 25 equally-spaced increments. The surface source intensity was maintained at 100 for all examples explored in this thesis. In the reconstruction process, only the comparison between the boundary angular fluxes at each iteration and of the actual solution is significant and the exact magnitude of the illuminating source is irrelevant. The boundaries where each illuminating source was imposed is also presented in this Table. In future test problems, the initial guess for the cross section distribution within the domain is also presented in the Table. The initial guess is very crucial in the optimization process and the performance of the routine is highly dependent on the quality of the initial guess. Finally, the addition of multiple experiments on the reconstruction process is explored in future problems and the number of experiments is specified in these Tables.

Table VI-I.: Example 1 Layout.

Angular Quadrature (Sn)	8
Domain Size (cm)	4x4
Number of Material Regions	2
Material Mesh	4x4
Flux Mesh	8x8
Number of Searched Parameters	2
Actual Cross Section of Material 1 (cm^{-1})	0.9
Actual Cross Section of Material 2 (cm^{-1})	1.1
Number of Guessed Parameter Pairs	625
Range of Guesses for Cross Section of Material 1 (cm^{-1})	0.45-1.80
Range of Guesses for Cross Section of Material 2 (cm^{-1})	0.55-2.20
Illuminating Source Intensity ($\frac{n}{(cm^2-Sr)}$)	100
Boundaries of Imposed Illuminating Sources	left, right, both

As can be seen in Table VI-I, the misfit surface was plotted for three different illuminating sources. These illuminating sources only imposed a flux directed at the angle that was most normal to that boundary of the domain. The misfit values in the following surface plots were represent logarithmically to amplify the small changes in the value of the object function as the two parameters varied. However, since the logarithm of zero is infinite, nothing is plotted for the combination of the parameters that yields the true domain configuration. This accounts for the holes in the data plotted in the following misfit surface plots.

First, a beam that encompassed the entire left side of the model was used to

illuminate the domain. The objective function surface that resulted from this process can be seen in Fig. VI-2. Because the left boundary is formed completely by the first region and the illuminating source is only imposed on this boundary, the flux measured at the boundaries offers little recognition that the domain consists of two regions. This is the reason why the misfit surface appears as a shallow valley with a minimum that is rather difficult to locate. In fact, if one only imposed the source on the left side and only measured the emitted radiation on the right side, one might expect that the reconstructed domain would be homogeneous with a magnitude equivalent to the average of the cross sections of the two actual regions. The orientation of the misfit surface is also interesting to note. The valley of the misfit surface for the first case runs parallel to the value of the cross section of the second region. This means that the illuminating source provides more information about the first region than the second region. This makes sense because the illuminating source is imposed directly on the first region and the signal has already undergone much attenuation before it reaches the second region.

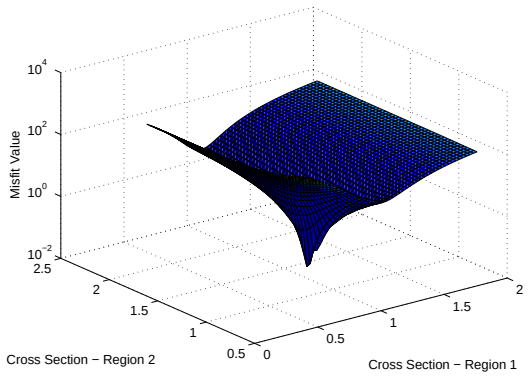

Fig. VI-2.: Two Parameter Problem - Left Beam.

In Fig. VI-3, again the objective function surface can be seen as a shallow valley. This is the result of the fact that the emitted flux on the left boundary offers

little information about the existence of the two distinct regions of the model. The orientation of the valley should also be noted. Since the boundary flux is imposed on the right side of the model, more information is now provided about the cross section of the second region than the first.

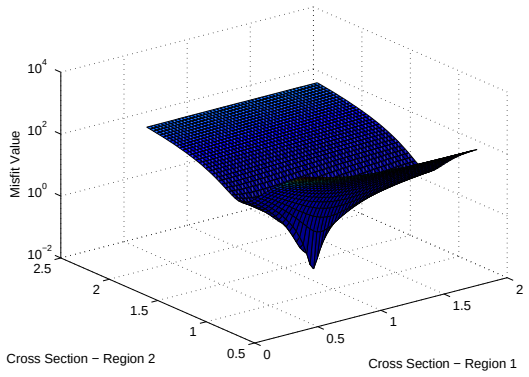

Fig. VI-3.: Two Parameter Problem - Right Beam.

Finally, illuminating sources were imposed on both the left and right boundaries of the model in Fig. VI-4. In this case, the sources illuminate both sides of the model and both cross sections become much more distinguishable. This is evidenced by the fact that the misfit surface plot is no longer a shallow valley, but more conical in shape. Finding the minimum of a cone is a much simpler optimization problem than finding the minimum of a shallow valley, because the objective function varies greatly along the conical surface and the gradient of a conical surface points more directly toward the minimum of the objective function. This also evidences a general trend that will be reinforced in the example problems to come that the addition of more illuminating beams, more measurement points and more experiments improves the ability of Newton's method to reconstruct the cross section values.

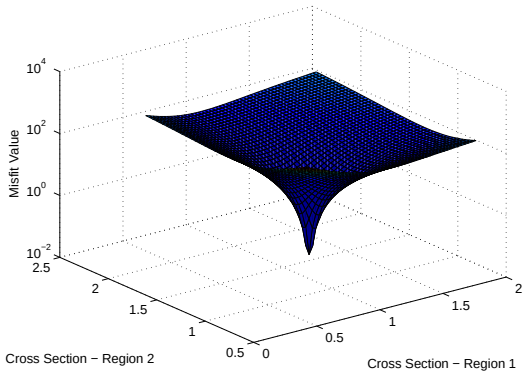

Fig. VI-4.: Two Parameter Problem - Both Beams.

2. Example 2 - Homogeneous Domain and Dual Absorber Convergence Study

The second example problem explores the ability of Newton's method to reconstruct the total cross sections of a homogeneous domain. All twenty-five of the cross sections of the domain are reconstructed independently and the Nelder-Mead method was also explored as a comparison between a method that computes the first and second derivatives of the Lagrangian versus one that simply evaluates the objective function. A list of the parameters that define the geometry, discretization scheme and source positions for the problem can be seen in Table VI-II.

Table VI-II.: Example 2a Layout.

Angular Quadrature (Sn)	8
Domain Size (cm)	6x6
Number of Material Regions	1
Material Mesh	5x5
Flux Mesh	15x15
Number of Searched Parameters	25
Actual Cross Section (cm^{-1})	1.00
Newton Initial Guess for Cross Section (cm^{-1})	1.75
Nelder-Mead Initial Guess for Cross Section (cm^{-1})	1.10
Illuminating Source Intensity ($\frac{n}{(cm^2-Sr)}$)	100
Illuminating Sources	all sides

The reconstruction and error results for the homogeneous domain can be seen in Fig. VI-5 for Newton's method and in Fig. VI-6 for the derivative free method. It is noticeable that the error in the reconstruction for Newton's method is orders of magnitude less than the error found using the Nelder-Mead method. The Nelder-Mead method was also provided with a homogeneous initial guess for the total cross section within the domain of 1.1. This value was much closer to the actual cross section of the domain than the initial guess provided for Newton's method of 1.75. Based on these results, it seems that the Nelder-Mead algorithm is more susceptible to be stuck in local minima than Newton's method. Further comparison of the two methods has been included in Table VI-III.

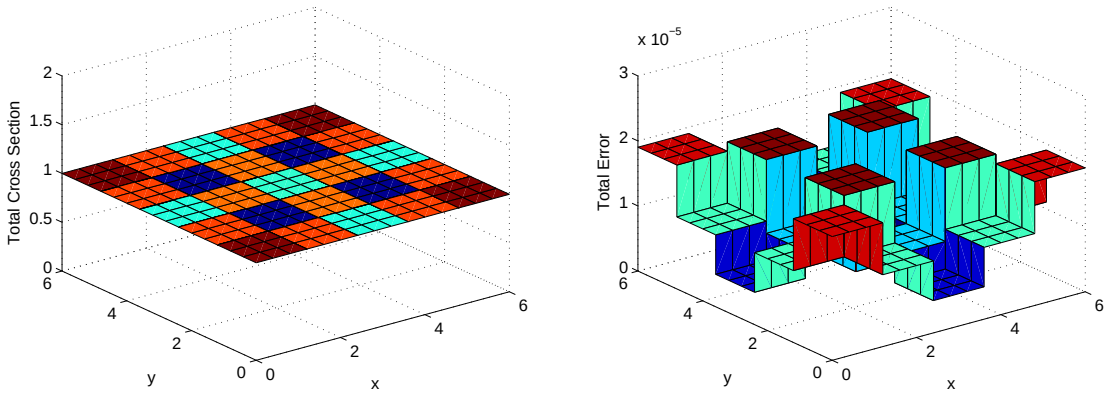

(a) Reconstruction (b) Error

Fig. VI-5.: Homogeneous Domain Reconstructed Cross Sections and Error Using Newton's Method.

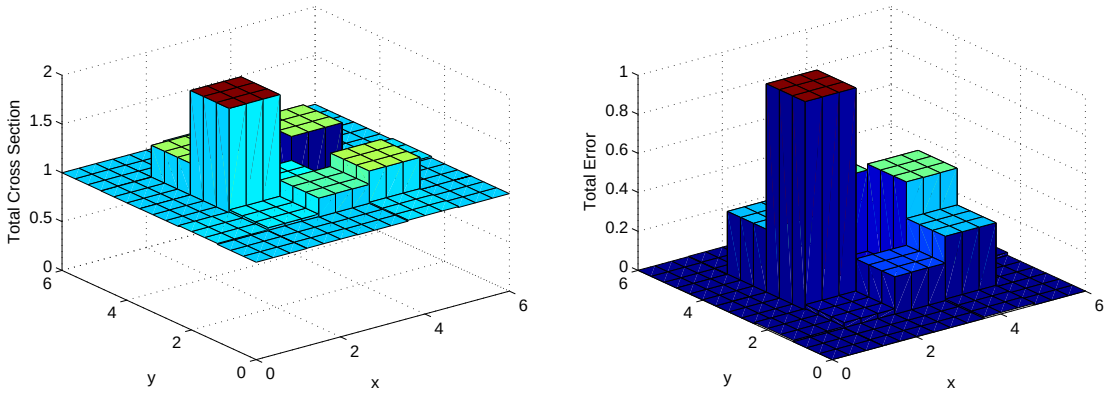

(a) Reconstruction (b) Error

Fig. VI-6.: Homogeneous Domain Reconstructed Cross Sections and Error Using Nelder-Mead Method.

In Table VI-III, we can see that Newton's method required much less computational time and fewer iterations than the Nelder-Mead algorithm. This is expected because Newton's method is a second order method that uses more information about

the objective function to locate its minimum. The final value of the Lagrangian was also determined to be orders of magnitude smaller for Newton's method as supposed to the derivative free method. This also is to be expected because the quality of the reconstruction was much better for Newton's method than that of the Nelder-Mead method.

Table VI-III.: Convergence Comparison between Optimization Techniques.

Method	Newton	Nelder-Mead
Time (hrs)	0.06	8.47
Number of Iterations	56	72515
Order of $\mathcal{L}$	10^{-6}	10^{-1}

Once the ability of Newton's method to reconstruct a homogeneous domain was established, a domain with two inclusions was reconstructed using Newton's method. Multiple figures have been included in this thesis to display the convergence process of Newton's method as it tries to find the parameters of the domain. A list of the parameters that define the geometry, discretization scheme and source positions for the problem can be seen in Table VI-IV. Again, all twenty-five parameters were reconstructed independently and further refinement was used in the computation of the flux solution to achieve a more accurate result.

Table VI-IV.: Example 2b Layout.

Angular Quadrature (Sn)	8
Domain Size (cm)	6x6
Number of Material Regions	3
Material Mesh	5x5
Flux Mesh	60x60
Number of Searched Parameters	25
Actual Cross Section of Surroundings (cm^{-1})	1.00
Actual Cross Section of Absorbers (cm^{-1})	1.50
Homogeneous Initial Guess for Cross Section (cm^{-1})	1.75
Illuminating Source Intensity ($\frac{n}{(cm^2-Sr)}$)	100
Illuminating Sources	all sides

Fig. VI-7 shows the convergence history for the dual inclusion problem. Each picture represents about every ninth iteration. In can be noticed that solution changes greatly in the first thirty iterations as Newton's method is searching for the parameters that best represent those of the domain. After iteration 30, the image changes very little and even large Newton steps lead to very small changes in the values of the parameters. Finally, the convergence criteria of reducing the Lagrangian and misfit functions to values less than 10^{-6} is achieved by iteration 92. This convergence criteria was used on all of the problems in this Thesis unless specified otherwise.

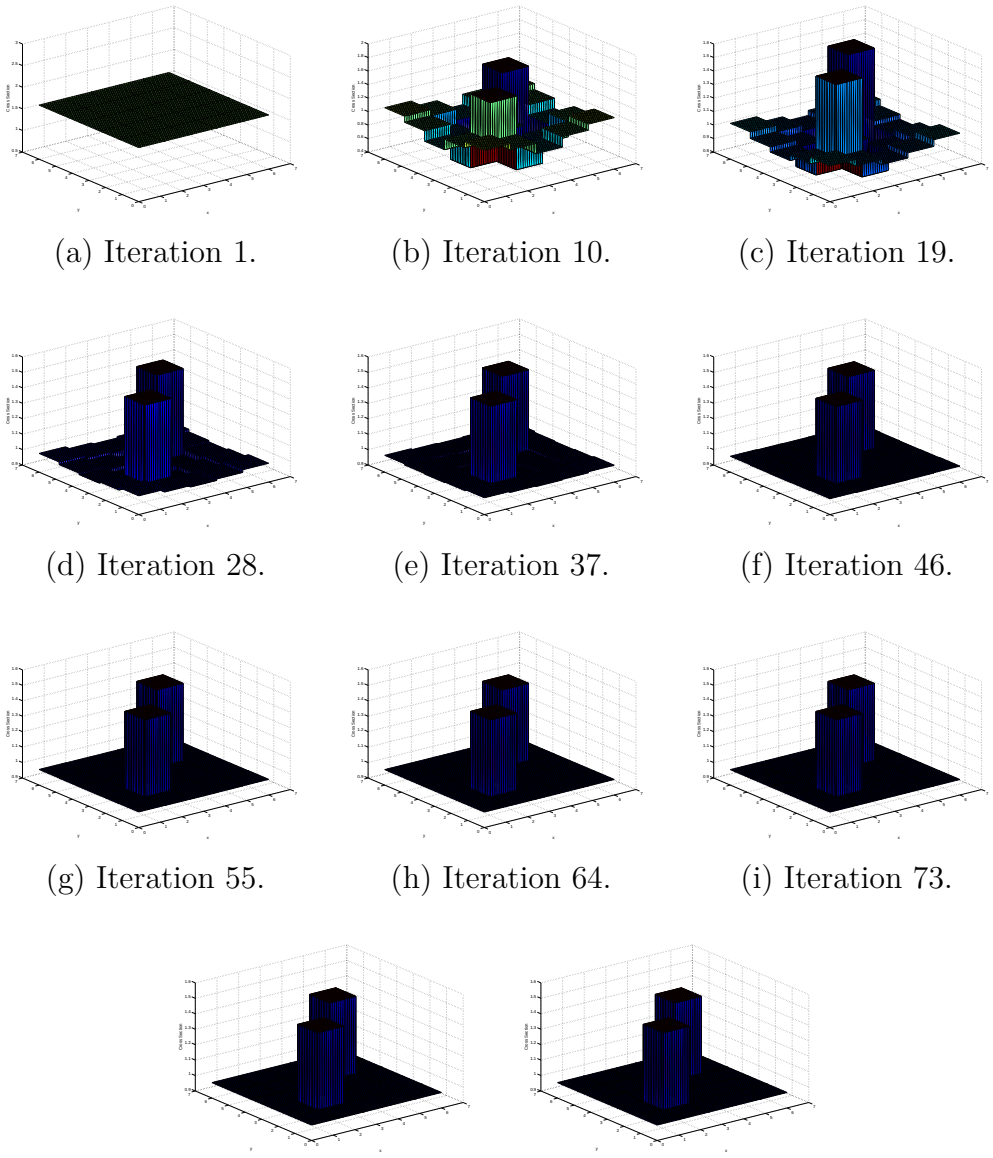

(a) Iteration 1. (b) Iteration 10. (c) Iteration 19.

(d) Iteration 28. (e) Iteration 37. (f) Iteration 46.

(g) Iteration 55. (h) Iteration 64. (i) Iteration 73.

(j) Iteration 82. (k) Iteration 92.

Fig. VI-7.: Dual Inclusion Domain Reconstruction

3. Example 3 - Four-Strip Domain

The third example problem explores the ability of the optimization method to reconstruct a domain comprised of four different materials aligned in a series of strips

of equal width. Each of the four different regions possesses a different cross section value and the example tests the ability of Newton's method to reconstruct a more complex domain. The true cross section map of the four strip domain can be seen in Fig. VI-8. A detailed description of the parameters that definite the geometry, discretization scheme, source locations and reconstructed cross sections can be found in Table VI-V. Because of the increased complexity of this four domain model, further refinement was required in the flux solution to allow domain reconstruction. In this model, all 16 of the possible distinct materials were allowed to independent in the reconstruction process. Sources were imposed and measurements were recorded on all boundaries of this model.

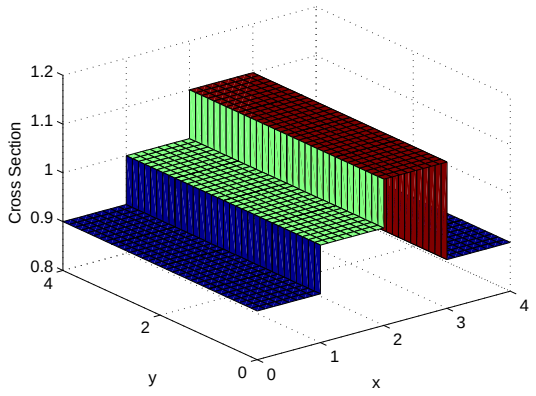

Fig. VI-8.: Actual Four-Strip Domain.

Table VI-V.: Example 3 Layout.

Angular Quadrature (Sn)	8
Domain Size (cm)	4x4
Number of Material Regions	4
Material Mesh	4x4
Flux Mesh	32x32
Number of Searched Parameters	16
Actual Cross Section of Material 1 (cm^{-1})	0.9
Actual Cross Section of Material 2 (cm^{-1})	1.0
Actual Cross Section of Material 3 (cm^{-1})	1.1
Actual Cross Section of Material 4 (cm^{-1})	0.9
Homogeneous Initial Guess for Cross Section (cm^{-1})	1.0
Illuminating Source Intensity ($\frac{n}{(cm^2-Sr)}$)	100
Illuminating Sources	all sides

In Fig. VI-9, it can be noticed that the reconstruction was a success and the final error was on the order of 10^{-5}. In this process the misfit and Lagrangian values were minimized to less that 10^{-6} in fourteen iterations. This convergence tolerance was maintained for all of the results presented in this thesis. All fourteen iterations were conducted in about twenty minutes.

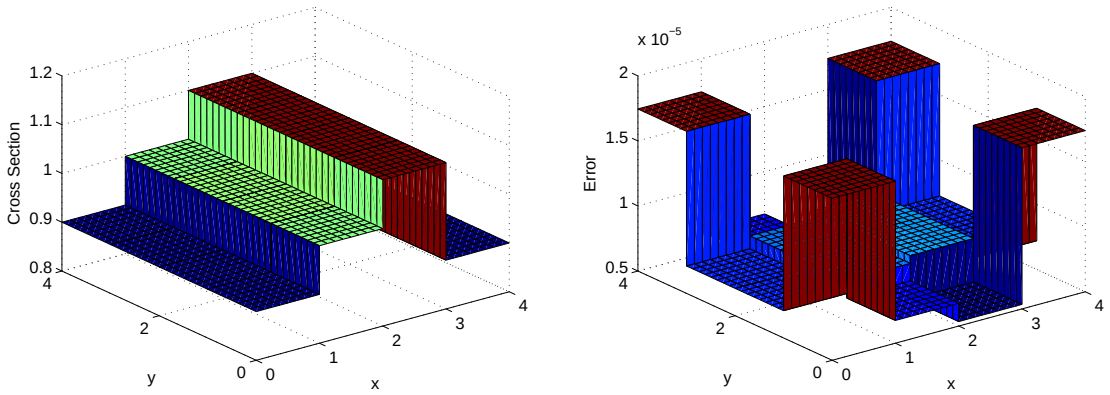

(a) Reconstruction (b) Error

Fig. VI-9.: Four-Strip Domain Reconstructed Cross Sections and Error.

4. Example 4 - Four Region Domain with Illuminating Sources on 1, 2, 3 or 4 Sides

In example 4, the ability of Newton's method to reconstruct the cross sections of a four-region domain is explored as illuminating beams are imposed on 1, 2, 3 or 4 sides of the geometry. Each reconstruction is conducted with only one experiment and it is shown that reconstruction ability improves as illuminating beams are imposed on more sides of the model. A list of the parameters that define the geometry, discretization scheme and source positions for the problem can be seen in Table VI-VI.

Table VI-VI.: Example 4 Input Parameters.

Angular Quadrature (Sn)	8
Domain Size (cm)	8x8
Number of Material Regions	4
Material Mesh	4x4
Flux Mesh	16x16
Number of Searched Parameters	16
Actual Cross Section of Material 1 (cm^{-1})	0.7
Actual Cross Section of Material 2 (cm^{-1})	0.9
Actual Cross Section of Material 3 (cm^{-1})	1.1
Actual Cross Section of Material 4 (cm^{-1})	1.3
Homogeneous Initial Guess for Cross Section (cm^{-1})	1.5
Illuminating Source Intensity ($\frac{n}{(cm^2-Sr)}$)	100
Illuminating Sources	1, 2, 3, 4 sides

A diagram that display the locations of each of the four material regions and labels each of the sides of the geometry can be seen in Fig. VI-10. This same material layout and side numbering scheme was maintained for all of the four region problems examined in this Thesis. These four region problems can be found in examples 8, 16 and 17.

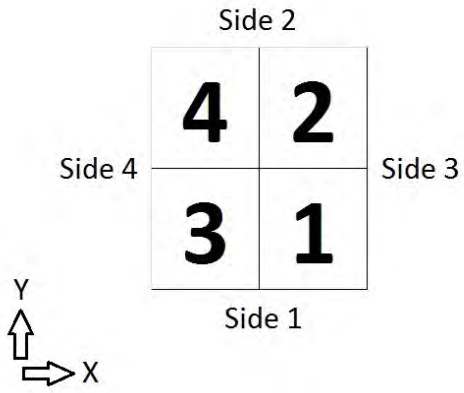

Fig. VI-10.: Diagram of Four Region Domain with Sides and Material Regions Identified.

In Fig. VI-11, the results of the test case where beams were only imposed on the side 1 of the geometry as seen in Fig. VI-10. In this case, Newton's method fails to generate a reconstruction of the domain because insufficient radiation is transmitted through the regions defined by materials 2 and 4 when the beam is only imposed on side 1. Because only minimal radiation is transmitted through regions 2 and 4, Newton's method has little information about these regions and begins to propose outrageous values for the cross sections of these regions. Because Newton's method was diverging from the solution and reconstruction was unlikely, the process was terminated after 100 iterations and these results are presented in Fig. VI-11. Similar results are expected if the sources were applied solely to any other side of the geometry simply because insufficient information is collected from a single scan conducted on a single side of the domain.

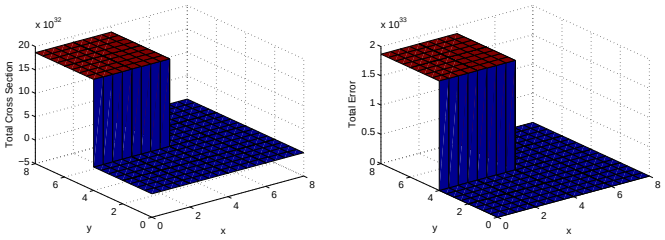

(a) Total Reconstruction. (b) Total Error.

Fig. VI-11.: Domain with Source on 1 Side Reconstructing both Scattering and Total Cross Sections

In Figs. VI-12, VI-13 and VI-14, sufficient information was collected from imposing beams on multiple sides of the model to permit reconstruction. The trend of reduced reconstruction error as illuminating sources were imposed on more sides of the model can also be noticed. In Fig. VI-12, beams were imposed on the sides 1 and 2 of the geometry as explained in Fig. VI-10. In Fig. VI-13, beams were imposed on sides 1, 2 and 3 as seen in Fig. VI-10. Finally, illuminating sources were modeled on all sides of the model in Fig. VI-14.

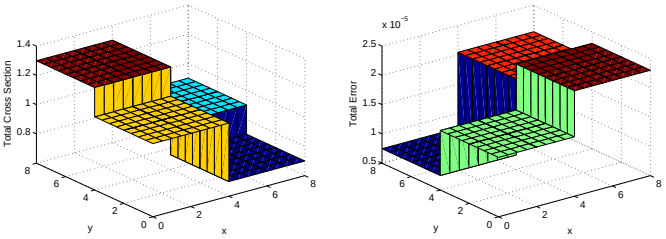

(a) Total Reconstruction. (b) Total Error.

Fig. VI-12.: Domain with Sources on 2 Sides Reconstructing both Scattering and Total Cross Sections

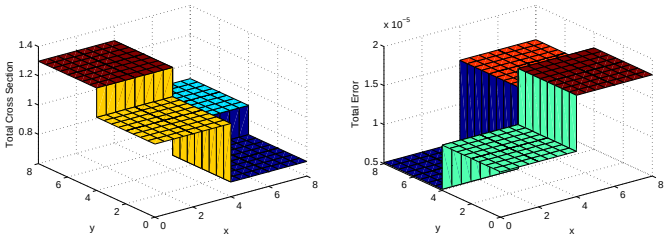

(a) Total Reconstruction. (b) Total Error.

Fig. VI-13.: Domain with Sources 3 Sides Reconstructing both Scattering and Total Cross Sections

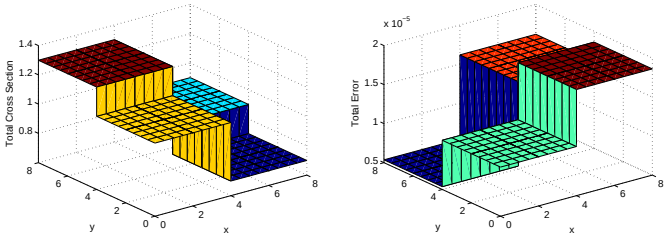

(a) Total Reconstruction. (b) Total Error.

Fig. VI-14.: Domain with Sources on 4 Sides Reconstructing both Scattering and Total Cross Sections

5. Summary of Findings from Pure Absorber Problems

In the pure absorber problems section, some initial simple problems were explored to visually get a feel for the inverse transport problem and how Newton's method uses variation of parameters to locate the solution of this inverse transport problem. In example 1, the surface of objective function for a simple two-parameter problem was plotted to understand what the surface looks like and the challenges associated with locating the minimum of this surface. In this problem, the reduction in the complexity

of the optimization problem by applying illuminating sources to two opposite sides of the model rather than just to one side was also noticed. This simplification in the optimization process was noticed as the misfit surface changed shape from a shallow valley with a minimum that was rather difficult to locate to more of a conical surface with an apparent minimum. In example 2, the ability of Newton's method to reconstruct a homogeneous domain was explored. The Nelder-Mead method was also used to reconstruct the same homogeneous domain to show the benefits of Newton's method. Newton's method required fewer iterations, less computational time and reconstructed an image with less error than the Nelder-Mead algorithm. This was attributed to Newton's method's utilization of the gradient and Hessian information of the constrained optimization problem. A problem with with two inclusions was also studied to display the reconstruction process using Newton's method. It was noticed that in the early iterations as Newton's method is searching for the parameters of the domain, the image varies greatly. As Newton's method begins to propose values of the parameters that are close to those used to create the synthetic data, the image changes very little even as Newton takes large steps. In example 3, a domain comprised of four strips was considered to display Newton's ability to reconstruct the material properties of a more complex domain. Finally in example 4, a four region domain each with unique cross sections was considered while imposing beams on 1, 2, 3 or all sides of the model in a single experiment. This study displayed the general trend that as illuminating sources are applied to more sides of the model, the error in the resulting image is reduced. It was also noticed that if insufficient radiation is transmitted through a domain, Newton's method can not determine the cross sections of certain regions of the model and outrageous values for the cross sections of those regions are proposed.

B. Pure Absorbers with Multiple Experiments

In this section, the ability of Newton's method to reconstruct the cross sections of various pure absorber domains where multiple experiments or scans are used. Examples 5 and 6 explore the optical thickness limits where the measurable signal becomes too small to permit reconstruction. Eight experiments each covering one half of a side are used in example 5, where as sixteen experiments each covering one fourth of a side are used in example 6. Example 7 examines the sensitivity of Newton's method to the proposed initial guess for the cross sections of a homogeneous domain reconstructed as four independent regions. Finally, example 8 displays the effects of using measurements collected from different sides of the domain. This example is successful in reconstructing all of the cross sections for all of the cases, but the same example will be revisited in example 17 in the scattering section and this will not be the case.

1. Example 5 - Central Inclusion Domains with 8 Experiments

In example 5, domains with a central inclusion and surrounding medium of increasing size are studied. These problems explored the optical thickness limit of Newton's method as more material is padded around the central inclusion. This additional material increases the number of mean free paths that the incident radiation must travel through until it reaches the boundary. This results in a reduction in the measurable signal at the boundary and increases the difficulty of the reconstruction process. In each of the models in this example, the flux cell size was held constant at 0.5 by 0.5 centimeters and eight experiments with beams covering half of a side were used in the reconstruction process. The domains were assumed to be comprised of only two parameters representing the surroundings and central inclusion and only the two

cross sections were reconstructed. The condition number of the Schur matrix was tracked throughout the reconstruction to determine how ill-conditioned the problem was and the reliability of the results. A list of the parameters that define the geometry, discretization scheme, reconstructed cross sections and source positions for the problem can be seen in Table VI-VII.

Table VI-VII.: Example 5 Input Parameters.

Angular Quadrature (Sn)	8
Domain Sizes (cm)	8x8, 12x12, 16x16, 20x20
Number of Material Regions	2
Material Mesh	4x4, 6x6, 8x8, 10x10
Flux Mesh	16x16, 24x24, 32x32, 40x40
Number of Searched Parameters	2
Actual Cross Section of Surroundings (cm^{-1})	0.9
Actual Cross Section of Absorber (cm^{-1})	1.3
Homogeneous Initial Guess for Cross Section (cm^{-1})	1.5
Illuminating Source Intensity ($\frac{n}{(cm^2-Sr)}$)	100
Illuminating Sources	8-exp, 1/2-side each

Figs. VI-15, VI-16, VI-17 and VI-18 present the reconstruction, error and condition number results for the 8x8, 12x12, 16x16 and 20x20 centimeter central inclusion problems, respectively. It can be noticed that the error in the reconstruction and the condition number of the Schur matrix is increased as the optical thickness of the problem is increased. The reconstruction is successful for the 8x8, 12x12 and

16x16 centimeter cases, but it fails for the 20x20 centimeter case. In all of the successful cases, there is a spike in the condition number in the early iterations before the method stabilizes. The maximum order of magnitude of the condition numbers registered for the 8x8, 12x12 and 16x16 centimeter cases were 10^6, 10^{11} and 10^{15}, respectively. In the 20x20 centimeter case, the condition number of the Schur matrix grows exponentially to 10^{27} in later iterations resulting in a failed reconstruction. In this case, again insufficient radiation reaches the center of the model where the inclusion is and therefore, the value of the cross section of this region has a negligible effect on the computed fluxes. Because of this Newton's method can not see the inclusion and begins to propose huge values for the cross section of this region. In this case, the termination criteria of minimizing the misfit and Lagrangian below 10^{-6} were still satisfied after 134 iterations because the inclusion cross section value has no effect on the flux solution. The final reconstructed cross section of the surroundings is correct, but the cross section of the inclusion varies by orders of magnitude from the actual solution as seen in Fig. VI-18.

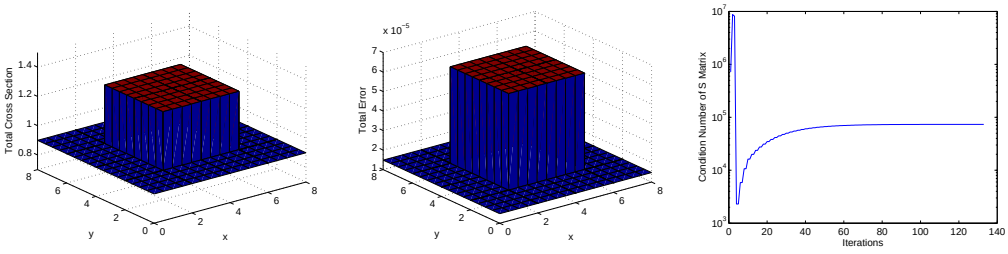

(a) Reconstruction. (b) Error. (c) Condition Number.

Fig. VI-15.: Reconstruction, Error and Condition Number Results for the 8x8cm Central Inclusion Problem

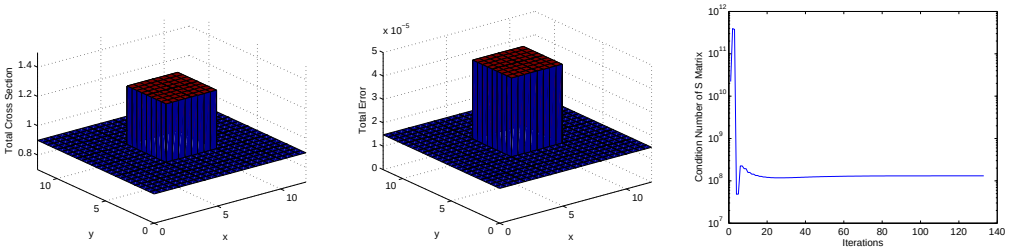

(a) Reconstruction. (b) Error. (c) Condition Number.

Fig. VI-16.: Reconstruction, Error and Condition Number Results for the 12x12cm Central Inclusion Problem

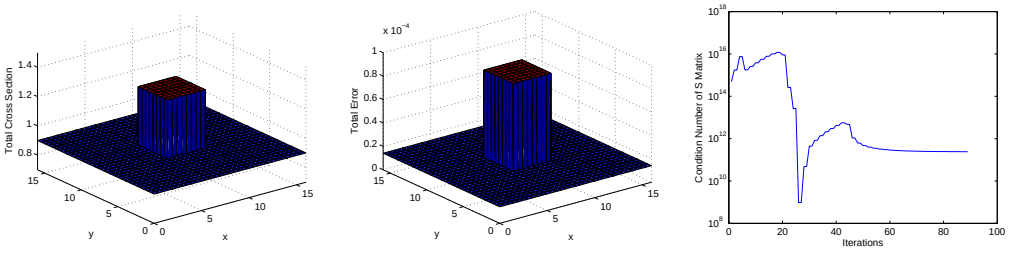

(a) Reconstruction. (b) Error. (c) Condition Number.

Fig. VI-17.: Reconstruction, Error and Condition Number Results for the 16x16cm Central Inclusion Problem

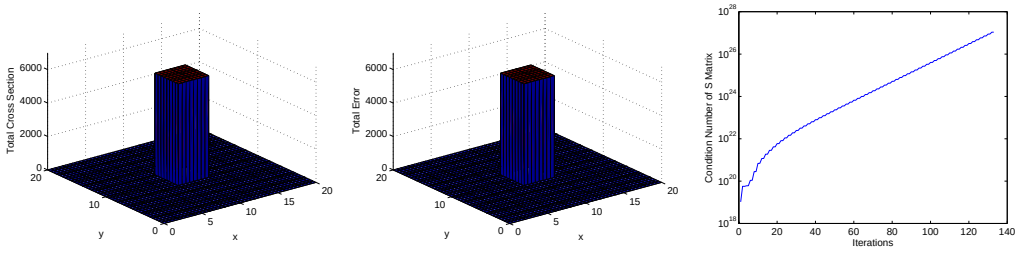

(a) Reconstruction. (b) Error. (c) Condition Number.

Fig. VI-18.: Reconstruction, Error and Condition Number Results for the 20x20cm Central Inclusion Problem

2. Example 6 - Central Inclusion Domains with 16 Experiments

Example 6 is very similar to example 5 where central inclusion of increasing optical thickness is studied. In example 6, sixteen experiments each encompassing one fourth of a side are modeled as supposed to the eight experiment problems studied in example 5. Because of the additional experiments, 8x8, 12x12, 16x16 and 20x20 centimeter domains were able to be reconstructed and the method did not fail until the 24x24 centimeter domain was attempted. Again the domains were assumed to be comprised of only two materials and only two parameters were reconstructed. The same flux cell size was maintained as in example 5. A list of the parameters that define the geometry, discretization scheme, reconstructed cross sections and source positions for the problem can be seen in Table VI-VIII.

Table VI-VIII.: Example 6 Input Parameters.

Angular Quadrature (Sn)	8
Domain Sizes (cm)	8x8, 12x12, 16x16, 20x20, 24x24
Number of Material Regions	2
Material Mesh	4x4, 6x6, 8x8, 10x10, 12x12
Flux Mesh	16x16, 24x24, 32x32, 40x40, 48x48
Number of Searched Parameters	2
Actual Cross Section of Surroundings (cm^{-1})	0.9
Actual Cross Section of Absorber (cm^{-1})	1.3
Homogeneous Initial Guess for Cross Section (cm^{-1})	1.5
Illuminating Source Intensity ($\frac{n}{(cm^2-Sr)}$)	100
Illuminating Sources	16-exp, 1/4-side each

Figs. VI-19, VI-20, VI-21, VI-22 and VI-23 present the reconstruction, error and condition number results for the 8x8, 12x12, 16x16, 20x20 and 24x24 centimeter central inclusion problems, respectively. As display in example 5, the error in the reconstruction and the condition number of the Schur matrix increase as the optical thickness of the problem increases. The reconstruction is successful for the 8x8, 12x12, 16x16 and 20x20 centimeter cases, but it fails for the 24x24 centimeter case. In all of the successful cases, there is a spike in the condition number in the early iterations before the method stabilizes. The maximum order of magnitude of the condition numbers registered for the 8x8, 12x12, 16x16 and 20x20 centimeter cases

were 10^6, 10^{11}, 10^{16} and 10^{19} respectively. In the 24x24 centimeter case, the condition number of the Schur matrix grows exponentially to 10^{31} in later iterations resulting in a failed reconstruction. Just as in example 5, the termination criteria of minimizing the misfit and Lagrangian below 10^{-6} were still satisfied after 134 iterations because the inclusion cross section value has no effect on the flux solution. The method was again able to correctly reconstruct the cross section of the surrounding material, but the cross section of the inclusion region is off by orders of magnitude as seen in Fig. VI-23.

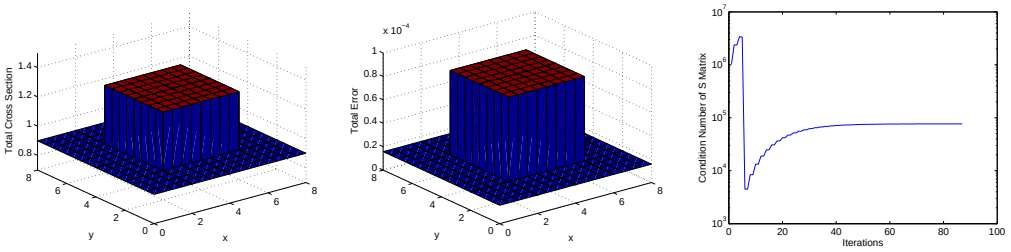

(a) Reconstruction. (b) Error. (c) Condition Number.

Fig. VI-19.: Reconstruction, Error and Condition Number Results for the 8x8cm Central Inclusion Problem

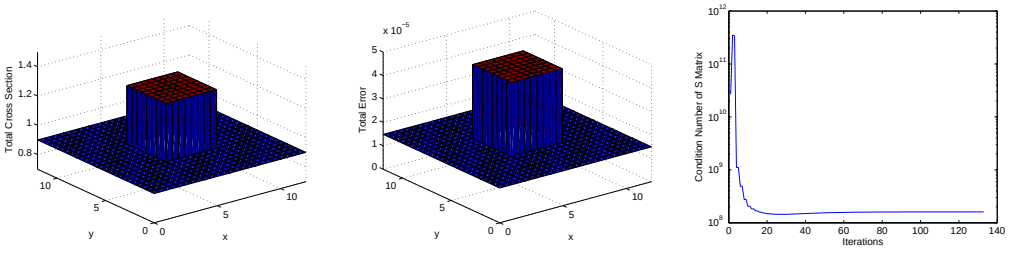

(a) Reconstruction. (b) Error. (c) Condition Number.

Fig. VI-20.: Reconstruction, Error and Condition Number Results for the 12x12cm Central Inclusion Problem

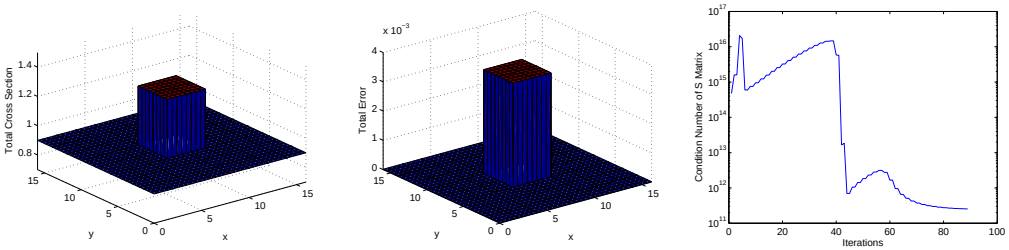

(a) Reconstruction. (b) Error. (c) Condition Number.

Fig. VI-21.: Reconstruction, Error and Condition Number Results for the 16x16cm Central Inclusion Problem

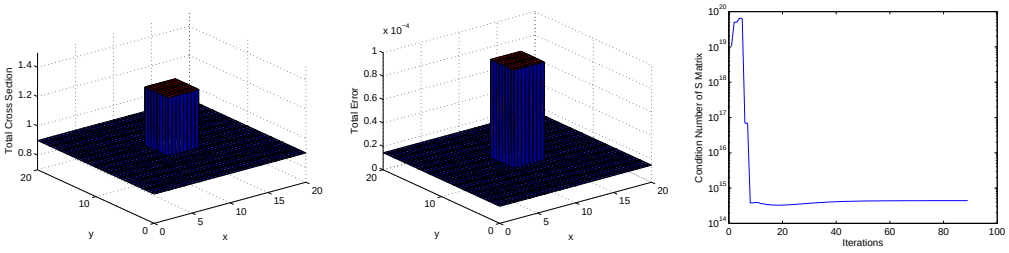

(a) Reconstruction. (b) Error. (c) Condition Number.

Fig. VI-22.: Reconstruction, Error and Condition Number Results for the 20x20cm Central Inclusion Problem

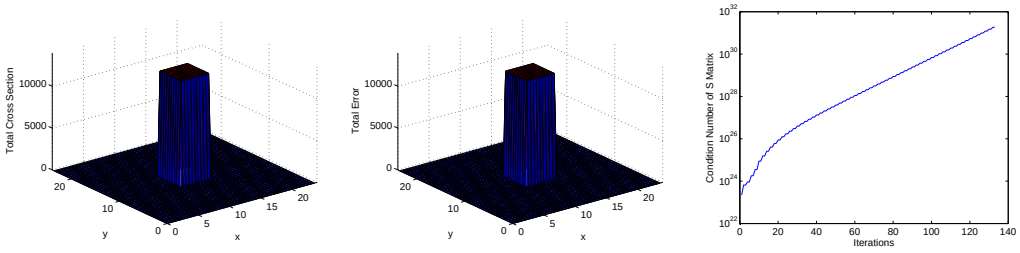

(a) Reconstruction. (b) Error. (c) Condition Number.

Fig. VI-23.: Reconstruction, Error and Condition Number Results for the 24x24cm Central Inclusion Problem

Because of the only minimal improvement in the reconstruction ability when sixteen versus eight experiments were conducted and the increased computational time required for the additional experiments, the remaining problems in this thesis will be simulated with eight experiments unless otherwise specified. But, generally increasing the number of experiments leads to some improvements which include more accurate reconstructions with less error, reconstructions that converge in fewer iterations and reduction in the condition numbers seen in the Schur matrix. The one downfall is that increasing the number of experiments leads to more computational time spent in each Newton iteration. There definitely exits a threshold were the addition of more experiments leads to minimal improvement in image quality because imposing sources extremely close together and taking additional measurements extremely close together adds little new information to the reconstruction.

3. Example 7 - Homogeneous Domain Initial Guess Study

In example 7, the effect of varying the initial guess for the parameters was studied for a homogeneous domain. The proposed initial guesses were varied at different distances from the actual solution in the positive and negative directions. The method proved rather robust for reconstructing the parameters of this problem for all of the initial guesses attempted. Since the domain considered in this problem was homogeneous, a heterogeneous initial guess generated using random numbers was used to make the reconstruction more challenging. In each case, the initial guess for the parameters was shifted based on some percentage of the actual parameter distribution and then random numbers were then used to create heterogeneity in the initial guess at 20-25% of the shift percentage. A description of these initial guesses and the input parameters for the problem can be found in Table VI-IX.

Table VI-IX.: Example 7 Input Parameters.

Angular Quadrature (Sn)	8
Domain Sizes (cm)	4x4
Number of Material Regions	1
Material Mesh	4x4
Flux Mesh	16x16
Number of Searched Parameters	4
Actual Cross Section of Domain (cm^{-1})	1.0
Initial Guesses Approaching from Above (%)	1000 ± 200, 5000 ± 1000, 10000 ± 2500
Initial Guesses Approaching from Below (%)	75 ± 5, 50 ± 10, 25 ± 15
Illuminating Source Intensity ($\frac{n}{(cm^2 - Sr)}$)	100
Illuminating Sources	8-exp, 1/2-side each

The sufficient decrease and curvature conditions were employed in all of the initial guess reconstructions conducted in this example. It was noticed that on many of the problems where the initial guess was below the actual solution, the Wolfe conditions would never be satisfied and the minimum step length was always used. To combat this problem, a slightly heuristic approach was employed were a check was conducted on the magnitude of the step length. If the step length was determined to be the same values for the five preceding iterations, the step length was then reset to 0.25 and the Newton iteration was continued. This approach proved successful for all of the cases tested in this example. The results of the three initial guess studies where the solution was approach from below can be seen in Figs. VI-24, VI-25 and VI-26. All of these figures display the proposed initial guess, the final reconstruction and the

error in the final reconstruction. All of these reconstructions were successful and the errors are all of similar magnitudes. The total number of iterations required to reduce the misfit and Lagrangian to less than 10^{-6} was determined to be 163, 81 and 62 for initial guesses of 75%, 50% and 25% of the actual paramters, respectively. Each of these reconstructions required the value of the step length to be reset to 0.25 multiple times.

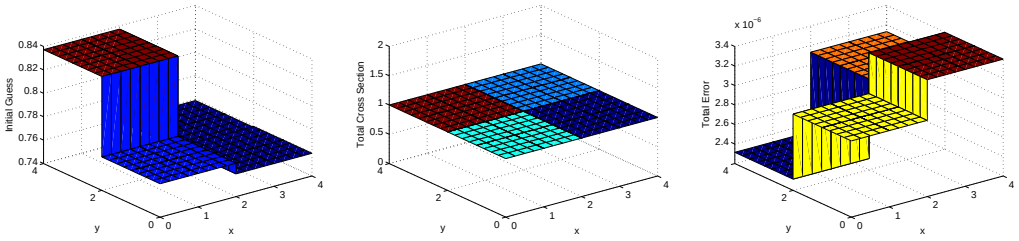

(a) Initial Guess. (b) Reconstruction. (c) Error.

Fig. VI-24.: Initial Guess of 75% ± 5% of Actual Cross Section of Homogeneous Domain

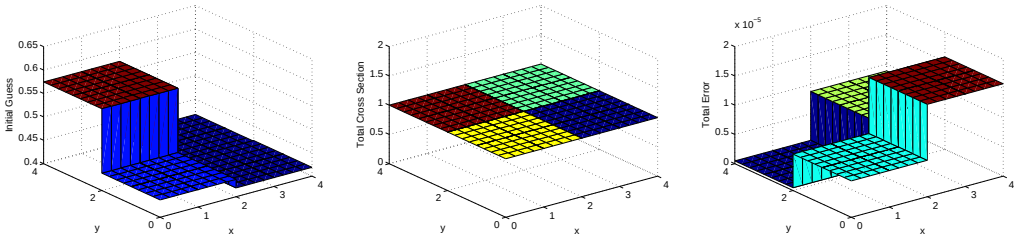

(a) Initial Guess. (b) Reconstruction. (c) Error.

Fig. VI-25.: Initial Guess of 50% ± 10% of Actual Cross Section of Homogeneous Domain

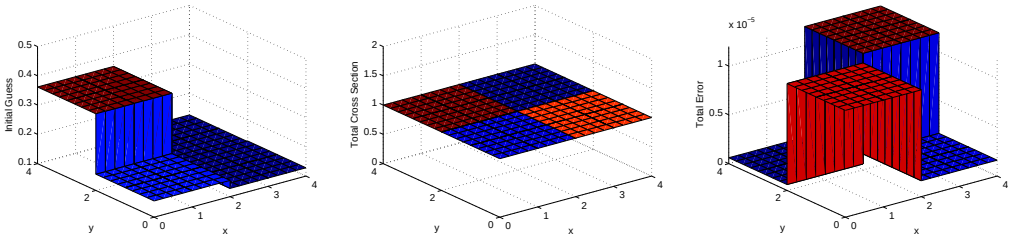

(a) Initial Guess. (b) Reconstruction. (c) Error.

Fig. VI-26.: Initial Guess of 25% ± 15% of Actual Cross Section of Homogeneous Domain

In the case of the initial guess that approach the solution from above, the optimization method never stagnated with the minimum step length. These reconstructions took many fewer iterations than when the solution was approached from below. The results of the three initial guess studies where the solution was approached from above can be seen in Figs. VI-27, VI-28 and VI-29. All of these figures display the proposed initial guess, the final reconstruction and the error in the final reconstruction. All of these reconstructions were successful and the errors are all of similar magnitudes. The total number of iterations required to reduce the misfit and Lagrangian to less than 10^{-6} was determined to be 14, 25 and 18 for initial guesses of 1000%, 5000% and 10000% of the actual paramters, respectively.

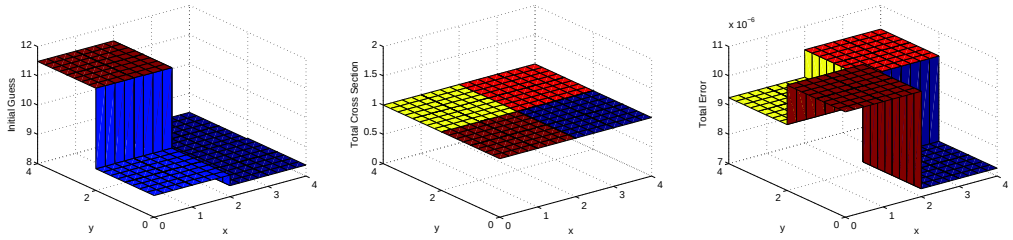

(a) Initial Guess. (b) Reconstruction. (c) Error.

Fig. VI-27.: Initial Guess of $1000\% \pm 200\%$ of Actual Cross Section of Homogeneous Domain

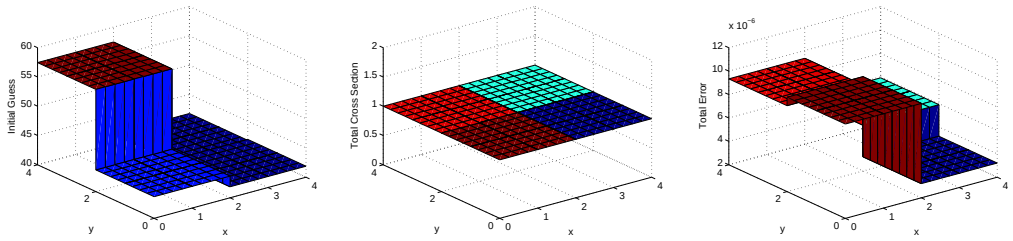

(a) Initial Guess. (b) Reconstruction. (c) Error.

Fig. VI-28.: Initial Guess of $5000\% \pm 1000\%$ of Actual Cross Section of Homogeneous Domain

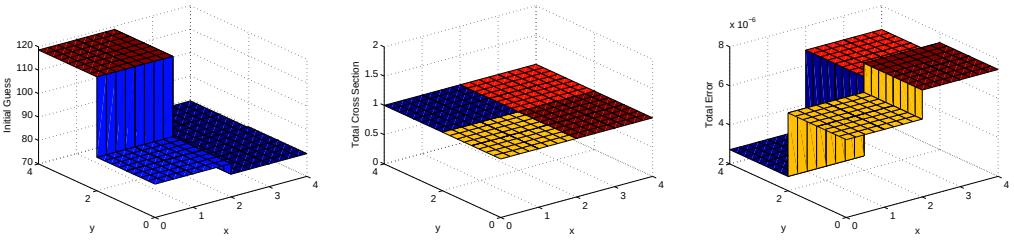

(a) Initial Guess. (b) Reconstruction. (c) Error.

Fig. VI-29.: Initial Guess of $10000\% \pm 2500\%$ of Actual Cross Section of Homogeneous Domain

Generally, Newton's method with the Wolfe conditions line search was able to reconstruct the solution easier from an initial guess that was above the values of the actual parameters. These higher initial guesses converged in many fewer iterations to solutions with lower error and the step size was never artificially modified.

4. Example 8 - Four-Region Domain with Measurements taken on 1, 2, 3 and 4 Sides

In example 8, a four-region domain is reconstructed with information collected from measurements on 1, 2, 3 or 4 sides of the model. All of these reconstructions were conducted with 8 experiments and a homogeneous initial guess for the parameters of 1.5 was used as the starting point for the reconstruction. The same material region layout and side numbering scheme was used in this example as can be seen in Fig. VI-10 of example 4. The example where measurements are only recorded from one side of the geometry collect measurements from side 1 as explained in Fig. VI-10. The test case where measurements are collected from two sides uses sides 1 and 2 as seen in Fig. VI-10. The test case where measurements are collected from three sides of the geometry uses sides 1, 2 and 3 as seen in Fig. VI-10. Finally, the last model uses measurements from all sides of the geometry to generate the image. A list of the parameters that define the geometry, discretization scheme, reconstructed cross sections and the source and measurement locations for the problem can be seen in Table VI-X.

Table VI-X.: Example 8 Input Parameters.

Angular Quadrature (Sn)	8
Domain Sizes (cm)	8x8
Number of Material Regions	4
Material Mesh	4x4
Flux Mesh	16x16
Number of Searched Parameters	4
Actual Cross Section of Material 1 (cm^{-1})	0.7
Actual Cross Section of Material 2 (cm^{-1})	0.9
Actual Cross Section of Material 3 (cm^{-1})	1.1
Actual Cross Section of Material 4 (cm^{-1})	1.3
Homogeneous Initial Guesses (%)	1.5
Illuminating Source Intensity ($\frac{n}{(cm^2-Sr)}$)	100
Illuminating Sources	8-exp, 1/2-side each
Measurements	1, 2, 3 or 4 Sides

Figs. VI-30, VI-31, VI-32 and VI-33 show the reconstruction and error results for the four region domain reconstructions with measurements taken on 1, 2, 3 and 4 sides of the model, respectively. In every case investigated in this example, Newton's method was able to correctly identify the parameters of the domain. It can also be noticed that the quality of the reconstruction is improved and the error in the reconstruction is reduced as measurements from more sides of the model are used. The reconstructions were conducted in fifty-five, fifty-nine, fifty-nine and forty-five minutes for the models with measurements on 1, 2, 3 and 4 sides, respectively. The images

were generated in 126, 124, 132 and 130 iterations for the models with measurements on 1, 2, 3 and 4 sides, respectively. The total number of iterations is pretty consistent for all of the cases, but the reconstruction using measurements from all four sides finished ten minutes quicker than other cases.

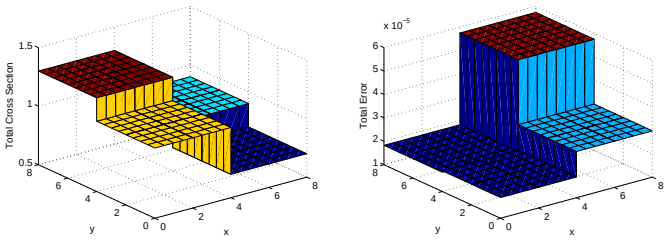

(a) Reconstruction. (b) Error.

Fig. VI-30.: Four Region Domain Measuring on 1 Side

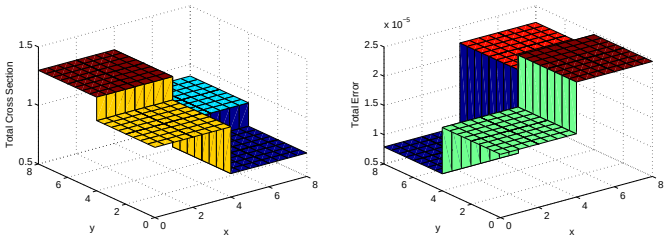

(a) Reconstruction. (b) Error.

Fig. VI-31.: Four Region Domain Measuring on 2 Sides

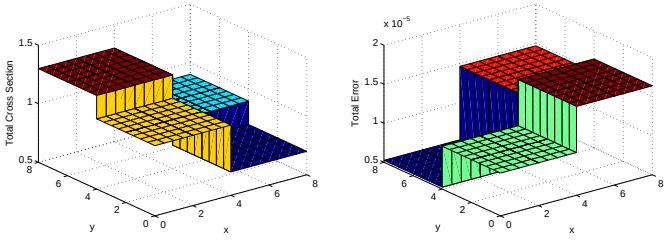

(a) Reconstruction. (b) Error.

Fig. VI-32.: Four Region Domain Measuring on 3 Sides

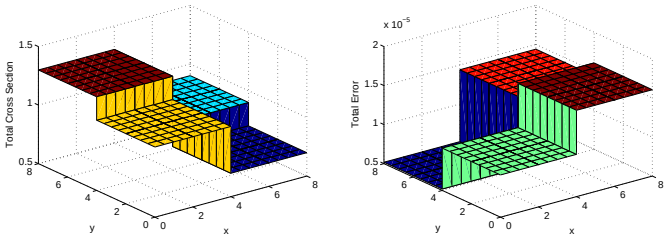

(a) Reconstruction. (b) Error.

Fig. VI-33.: Four Region Domain Measuring on 4 Sides

5. Summary of Findings from Pure Absorbers with Multiple Experiments

In this section on pure absorbers with multiple experiments, the improvements in image quality when using multiple experiments was explored. In example 5, the optical thickness limit of the Newton's method was explored through central inclusion problems of increasing size. Eight experiments each with a beam covering half of a side were used to reconstruct these problems. The optical thickness limit was determined to be eight mean free paths deep into the object. The condition number of the Schur complement matrix was also tracked in these reconstructions and it was a good indicator of the difficulty of the reconstruction problem. The condition number of the Schur matrix increased as the optical thickness increased and all of the successful cases showed sharp peaks in the condition number in earlier iterations, but lower condition numbers as method got closer to the solution. In the unsuccessful reconstruction, the condition number of the Schur matrix continued to increase through all the interactions of the optimization process and never stabilized. Example 6 showed many of the same trends as example 5. An optical thickness limit of nearly ten mean free paths was achieved with sixteen experiments rather than only eight. The same trends were observed with regard to the condition number of the Schur complement matrix as were seen in example 5. In example 7, the sensitivity of Newton's method

to the initial parameter distribution used to start the optimization process was studied. It was noticed that Newton's method could reconstruct images much easier from an initial guess consisting of values that were larger in magnitude than the actual parameters than from one with values lower in magnitude. This was noticed from the need to force Newton's method to take larger steps at various times in the optimization process to overcome stagnation points when starting from lower initial guesses. Also, many more iterations were required for lower initial guesses than higher ones. Finally in example 8, it was noticed that using measurements from more sides of the model in the reconstruction process generally leads to higher quality reconstruction with less error.

C. Pure Absorbers with Signal Noise and Bias

The next few test cases will simulate the effects of signal noise and bias on the measured angular fluxes that are used in the reconstruction process. The addition of signal noise simulates how the presence of background radiation will affect your detector readings. The addition of signal bias simulates the signal drift in the detector as the crystal temperature is increased from cold startup to operating temperatures. Multiplicative signal noise assumes that all measurements experience the same level of noise represented by Eq. (6.1):

$$z_{i,\text{noise}} = z_i(1 + \beta\epsilon_i) \tag{6.1}$$

Here, β is the percentage of the actual signal that is noise, ϵ_i is the random number that ranges from positive to negative unity and z_i is the measured angular flux vector without signal noise. Signal bias can be represented by the relationship seen in Eq. (6.2):

$$z_{i,\text{biased noise}} = z_i(1 + \delta + \beta\epsilon_i) \tag{6.2}$$

Here, the additional δ term is the signal bias and this term simply shifts all of the measurements in either the positive or negative direction.

1. Example 9 - Four Strip Domain with Signal Noise

In the ninth example a domain comprised of four strips of different cross sections is considered where 0.01%, 0.10%, and 1.00% signal noise is applied to the measured angular fluxes. The geometry consists of a 4x4 material mesh where all sixteen of these parameters are independently reconstructed. The cross sections of the four regions are 0.9, 1.0, 1.1 and 0.9, respectively. The inital guess for the domain was a homogeneous 1.5 and eight experiments with each beam encompassing half of a side were modeled. A list of the parameters that define the geometry, discretization scheme, reconstructed cross sections and source positions for the problem can be seen in Table VI-XI.

Table VI-XI.: Example 9 Input Parameters.

Angular Quadrature (Sn)	8
Domain Sizes (cm)	4x4
Number of Material Regions	4
Material Mesh	4x4
Flux Mesh	32x32
Number of Searched Parameters	16
Actual Cross Section of Material 1 (cm^{-1})	0.9
Actual Cross Section of Material 2 (cm^{-1})	1.0
Actual Cross Section of Material 3 (cm^{-1})	1.1
Actual Cross Section of Material 4 (cm^{-1})	0.9
Homogeneous Initial Guess for Cross Section (cm^{-1})	1.5
Illuminating Source Intensity ($\frac{n}{(cm^2-Sr)}$)	100
Illuminating Sources	8-exp, 1/2-side each
Multiplicative Signal Noise (%)	0.01, 0.1, 1.0

In Fig. VI-34, the results of the four bar domain reconstruction can be seen with 0.01%, 0.10%, and 1.00% signal noise. As is to be expected, the reconstructed image posseses much less acuracy when more noise is applied to the measured angular fluxes. The error plots seen in Fig. VI-35 also evidence this trend. An additional termination criteria was required so that Newton's method would stop. Based on the amount of signal noise, there is a minimum value of the Lagrangian and objective function that Newton's method can achieve which is generally greater than the convergence tolerance of 10^{-6} used in this thesis. This occurs because Newton's method can not

account for the noise in the synthetic data and will always search for the parameters without the applied noise. This leads to an error between the measured and computed fluxes that can never be removed completely. Therefore, an additional check was introduced to see if the two concurrent values of the Lagranigain and misfit only deviate by less than 10^{-6}, then the optimization routine is terminated.

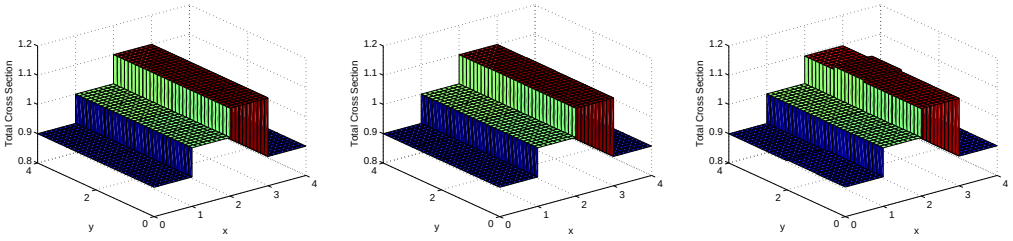

(a) 0.01% Noise. (b) 0.10% Noise. (c) 1.00% Noise.

Fig. VI-34.: Reconstructions of Four Strip Domain with Differing Amounts of Signal Noise

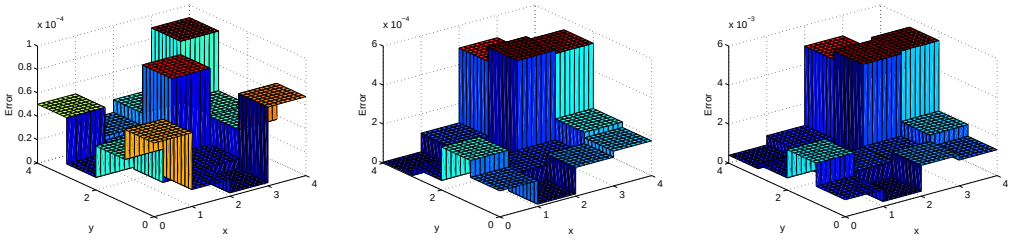

(a) 0.01% Noise. (b) 0.10% Noise. (c) 1.00% Noise.

Fig. VI-35.: Error in Reconstructions of Four Strip Domain with Differing Amounts of Signal Noise

2. Example 10 - Central Inclusion with Signal Noise and Positive and Negative Signal Bias

In the tenth example a domain comprised of a central inclusion and surrounding medium is considered where only signal noise is applied, noise and positive signal bias are applied or noise and negative signal bias are applied to the measured angular fluxes. In the first set of cases, 0.01%, 0.10%, and 1.00% signal noise is applied to the measured angular fluxes. In the second set of cases, 0.10% signal noise and either 1.00% or 5.00% positive signal bias is applied to the measured angular fluxes. In the third set of cases, 0.10% signal noise and either 1.00% or 5.00% negative signal bias is applied to the measured angular fluxes. However, the geometry of the model remains the same for all of these studies and it consists of a 4x4 material mesh where all sixteen of these parameters are independently reconstructed. The cross sections of the two regions are 1.0 and 1.3, respectively. The inital guess for the domain was a homogeneous 1.5 and eight experiments with each beam encompassing half of a side were modeled. A list of the parameters that define the geometry, discretization scheme, reconstructed cross sections and source positions for the problem can be seen in Table VI-XII.

Table VI-XII.: Example 10 Input Parameters.

Angular Quadrature (Sn)	8
Domain Sizes (cm)	4x4
Number of Material Regions	2
Material Mesh	4x4
Flux Mesh	8x8
Number of Searched Parameters	16
Actual Cross Section of Surroundings (cm^{-1})	1.0
Actual Cross Section of Inclusion (cm^{-1})	1.3
Homogeneous Initial Guess for Cross Section (cm^{-1})	1.5
Illuminating Source Intensity ($\frac{n}{(cm^2-Sr)}$)	100
Illuminating Sources	8-exp, 1/2-side each
Multiplicative Signal Noise (%)	0.01, 0.10, 1.00
Positive Signal Bias (%)	1.00, 5.00
Negative Signal Bias (%)	1.00, 5.00

Figs. VI-36 and VI-37 display the reconstruction and error results for the noise only studies where 0.01%, 0.10%, and 1.00% signal noise is applied to the measured angular fluxes. As expected, the quality of the reconstruction and the amount of error as more signal noise is imposed. The effects of the signal noise on the reconstructed cross sections are nearly unnoticable for the models with 0.01% and 0.10% signal noise. The effects are more prominant in the case with 1.00% signal noise. The images were generated in 8.4, 9.9 and 10.5 minutes for the 0.01%, 0.10%, and 1.00% signal noise cases, respectively. The 0.01% and 0.10% signal noise studies required seventy-one

iterations and the 1.00% signal noise study required seventy-five iterations.

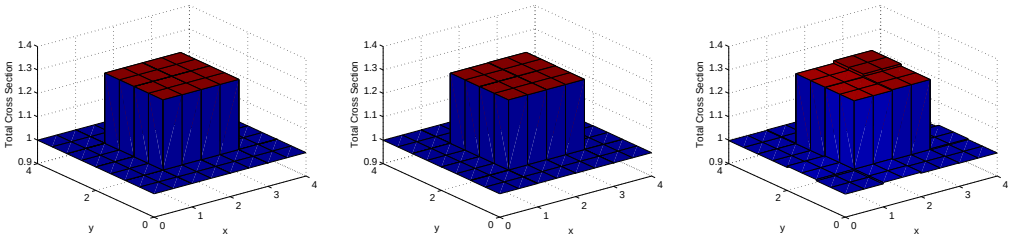

(a) 0.01% Noise. (b) 0.10% Noise. (c) 1.00% Noise.

Fig. VI-36.: Reconstruction of Central Inclusion Domain with Differing Amounts of Signal Noise

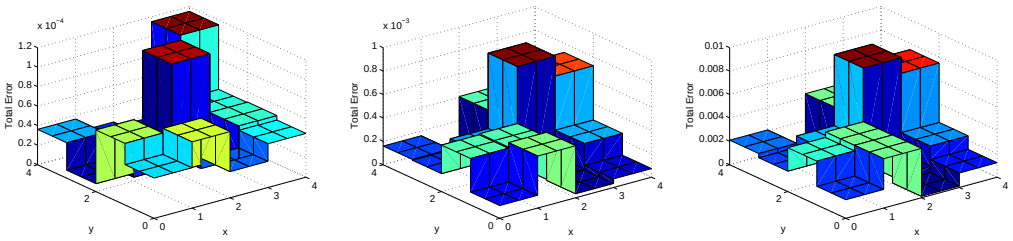

(a) 0.01% Noise. (b) 0.10% Noise. (c) 1.00% Noise.

Fig. VI-37.: Error in Reconstruction of Central Inclusion Domain with Differing Amounts of Signal Noise

Figs. VI-38 and VI-39 display the reconstruction and error results for the signal noise and positive signal bias studies where 0.10% signal noise and 1.00% or 5.00% signal bias are applied to the measured angular fluxes. Since positive signal bias has the effect of increasing all of the measured fluxes by some constant value, the effects are rather apparent in the reconstruction and error results. In the reconstructions for the positive signal bias cases, the reconstructed central inclusion region is lower by approximately 1.00% or 5.00% than the actual cross section of this region of 1.3. These results make sense because if the measurements are influenced by positive

signal bias, then the fluxes are 1.00% or 5.00% higher than they would be if the bias was not present. This implies that the inverse transport method should predict 1.00% or 5.00% less absorption to occur in this region of the domain and this is the case. The cells in the corners of the domain also show this same trend where there predicted values are 1.00% or 5.00% less than if the signal bias was not present. The remaining material regions that lie in the region surrounding the inclusion but not on the corners of the domain are 1.00% or 5.00% more than they would be if the bias was not present. This can be attributed to the fact that the predicted flux distribution with signal bias is still similar to the predicted flux distribution without signal bias and this causes these regions to be elevated to compensate for the decrease in the other cross sections.

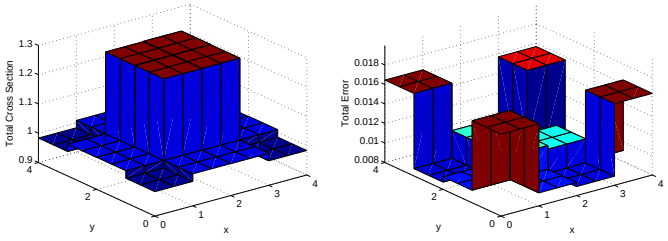

(a) Reconstruction. (b) Error.

Fig. VI-38.: Central Inclusion Domain with 0.10% Signal Noise and Positive 1.00% Signal Bias

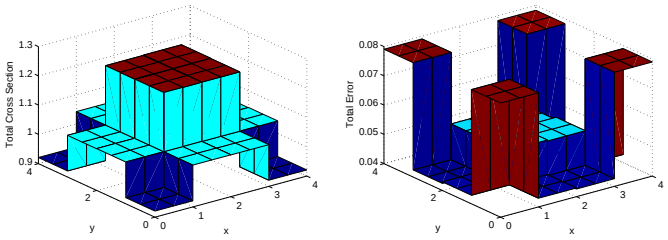

(a) Reconstruction. (b) Error.

Fig. VI-39.: Central Inclusion Domain with 0.10% Signal Noise and Positive 5.00% Signal Bias

Figs. VI-40 and VI-41 display the reconstruction and error results for the signal noise and negative signal bias studies where 0.10% signal noise and 1.00% or 5.00% signal bias are applied to the measured angular fluxes. Since negative signal bias has the effect of decreasing all of the measured fluxes by some constant value, the effects are rather apparent in the reconstruction and error results. In the reconstructions for the negative signal bias cases, the reconstructed central inclusion region is higher by approximately 1.00% or 5.00% than the actual cross section of this region of 1.3. These results make sense because if the measurements are influenced by negative signal bias, then the fluxes are 1.00% or 5.00% lower than they would be if the bias was not present. This implies that the inverse transport method should predict 1.00% or 5.00% more absorption to occur in this region of the domain and this is the case. The cells in the corners of the domain also show this same trend where there predicted values are 1.00% or 5.00% more than if the signal bias was not present. The remaining material regions that lie in the region surrounding the inclusion but not on the corners of the domain are 1.00% or 5.00% less than they would be if the bias was not present. This can be attributed to the fact that the predicted flux distribution with signal bias is still similar to the predicted flux distribution without signal bias

and this causes these regions to be decreased to compensate for the increase in the other cross sections.

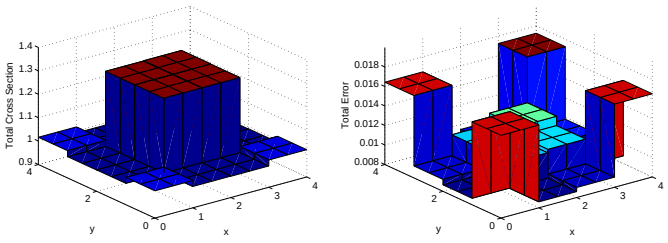

(a) Reconstruction. (b) Error.

Fig. VI-40.: Central Inclusion Domain with 0.10% Signal Noise and Negative 1.00% Signal Bias

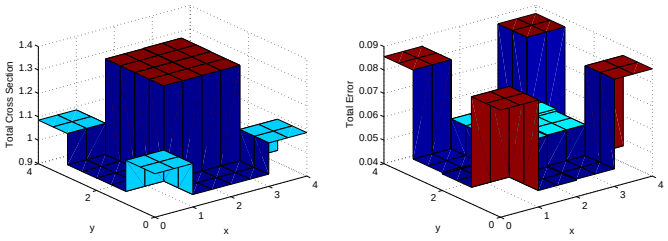

(a) Reconstruction. (b) Error.

Fig. VI-41.: Central Inclusion Domain with 0.10% Signal Noise and Negative 5.00% Signal Bias

3. Summary of Findings from Pure Absorbers with Signal Noise and Bias

In this section, the effects of the addition of signal noise and signal bias was explored on some pure absorber problems. Generally, the addition of signal noise and signal bias increased the difficulty in image reconstruction and produced images with greater error. In example 9, a four strip domain was examined where various amounts of signal noise was applied to the synthetic data. Image quality declined as the signal noise

was increased. The need for an additional convergence criteria was required in the reconstructions with signal noise due to the fact that noise represented a minimum amount of error that Newton's method could never eliminate. In example 10, the effects of signal noise and signal bias were examined on a central inclusion problem. The same trend of decreased image quality as the amount of signal noise and bias was increased was also evident for this example. The results seen for the cases with signal bias could be explained by the increased or decreased flux values. An increase in the fluxes would generally imply that less absorption occurred in the domain and visa versa and these trends were apparent in the reconstructions.

D. Scattering Problems

In this section, the ability of Newton's method to reconstruct the material properties of domains with scattering is examined. In example 11, a two-parameter problem is studied so that the surface of the objective function can be plotted for problems with various amounts of scattering. In example 12, the scattering and total cross sections of a homogeneous domain are reconstructed as eight independent parameters to test Newton's ability to reconstruct a simple domain with scattering. In example 13, the effects of adding signal noise and bias to the reconstruction process for a four-strip domain. In examples 14, 15, 16 and 17 the optical thickness, initial guess, different source locations and different measurement locations example problems are revisited with scattering, respectively. Eight experiments are used in all of the reconstructions in this section with the exception of example 16 where the source locations are varied. In example 16, only one experiment is used in the reconstruction.

1. Example 11 - Scattering Misfit Surface Plots

In the eleventh example the surface of the objective function is considered for a homogeneous domain with constant total and scattering cross sections. This two-parameter problem allows for the misfit surface to be plotted as a function of the scattering and total cross sections. The misfit surface is considered for four different scattering cross sections. These scattering cross sections were determined based on a percentage of the total cross section so that the complete range of low to high scattering medium could be plotted. The scattering percentages considered in these misfit surface plots were 10%, 50%, 90% and 99%. A 50x50 grid of values was used to generate the suface of the objective function and these values ranged from 50% to 200% of the true value of the parameters. The true total cross section was maintained at a value of 1.00 cm^{-1} for all of the studies. Therefore, the true scattering cross sections were 0.10, 0.50, 0.90 and 0.99 cm^{-1}. A list of the parameters that define the geometry, discretization scheme and source positions used to generate these misfit surfaces can be seen in Table VI-XIII.

Table VI-XIII.: Example 11 Input Parameters.

Angular Quadrature (Sn)	8
Domain Size (cm)	4x4
Number of Material Regions	1
Material Mesh	4x4
Flux Mesh	8x8
Number of Searched Parameters	2
True Total Cross Section (cm^{-1})	1.00
True Scattering Cross Section (cm^{-1})	0.10, 0.50, 0.90, 0.99
Number of Guessed Parameter Pairs	2500
Range of Guesses for Total Cross Section (cm^{-1})	0.50-2.00
Range of Guesses for Scattering Cross Section (%)	50-200
Illuminating Source Intensity ($\frac{n}{(cm^2-Sr)}$)	100
Boundaries of Imposed Illuminating Sources	all sides

In Fig. VI-42, the misfit surface that results from the 10% scattering case is presented. With this low amount of scattering, the misfit surface resembles the misfit surface from the the pure absorber model seen in example 1. In this case, determining the total cross section is much easier than determining the scattering cross section. This is evidenced by the fact that the misfit surface changes more drastically with changes in the total cross section than with changes in the scattering cross section. The scattering cross section is generally more difficult to reconstruct than the total cross section using Newton's method. Therefore, some of the problems seen in the pure absorber section of this thesis were simplified when it was desired to reconstruct

both the total and scattering cross sections. In addition, because a 50x50 grid of values was used to generate the misfit surface, the combination of cross sections that yeilds the true values was not plotted and no hole is present in the data for any of these figures.

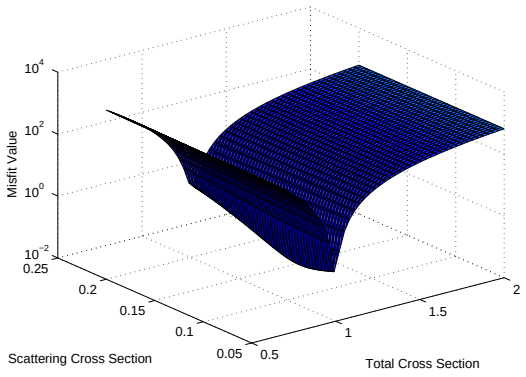

Fig. VI-42.: Misfit Surface Plot with 10% Scattering.

In Fig. VI-43, the misfit surface that results from the 50% scattering case is presented. The area where the sharp peaks are found can be ingored in this figure because the combination of cross sections that were used to generate these values correspond to a situation where the scattering cross section is larger than the total cross section. Since the scattering cross section can never be larger than the total cross section, these values are non-physical and should be ignored. It can also be noticed that the misfit surface of the case with 50% scattering is very flat and the gradient only changes drastically very near the true value of the parameters. This means that the gradient of the objective function provides little information about the location of the minimum of the objective function unless the proposed values of the parameters is very near the true parameters. This displays the difficulty of the optimization problem where both the total and scattering cross section are to be reconstructed and one may expect slow convergence for initial guesses that are far

from the actual solution.

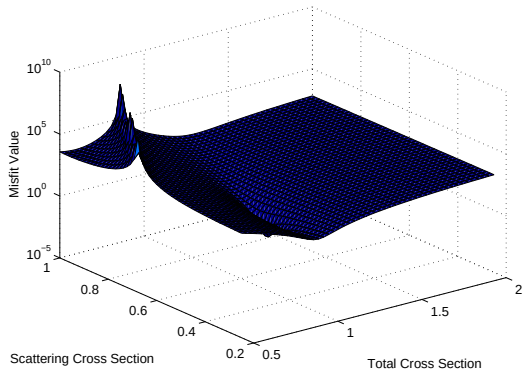

Fig. VI-43.: Misfit Surface Plot with 50% Scattering.

In Fig. VI-44, the misfit surface that results from the 90% scattering case is presented. Again some non-physical parameters combinations have been plotted and these should be ignored. The valley of the misfit where the minimum is located has now rotated so that is runs along a line that approximately corresponds to when the scattering cross section is equal to the total cross section. Again it can be seen that misfit surface is rather flat except as the the misfit valley is approached.

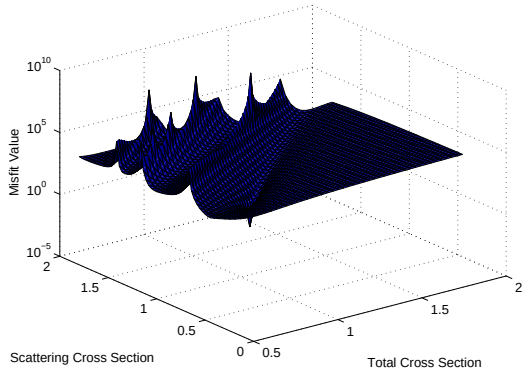

Fig. VI-44.: Misfit Surface Plot with 90% Scattering.

In Fig. VI-45, the misfit surface that results from the 99% scattering case is

presented. Again some non-physical parameters combinations have been plotted and these should be ignored. The valley of the misfit where the minimum is located runs along a line that approximately corresponds to when the scattering cross section is equal to the total cross section.

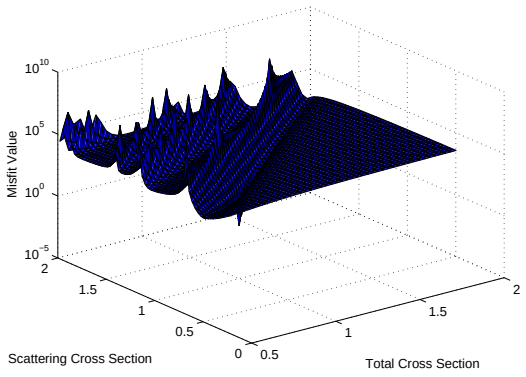

Fig. VI-45.: Misfit Surface Plot with 99% Scattering.

2. Example 12 - 8-Parameter Homogeneous Domain

In example 12, a domain with true total and scattering cross section distributions that are homogeneous is reconstructed as four distinct material regions or an 8-parameter problem. This simple problem serves as an introduction to the process of reconstructing both the scattering and total cross sections simultaneously. This inverse transport problem was conducted for three different scattering cross sections of 0.10, 0.50 and 0.90 cm^{-1}. In all cases the total cross section was maintained at a constant 1.00 cm^{-1}. An initial guess of 1.50 cm^{-1} was proposed for the values of all of the scattering and total cross sections in each of the studies in this example. A list of the parameters that define the geometry, discretization scheme, reconstructed cross sections and source positions for the problem can be seen in Table VI-XIV.

Table VI-XIV.: Example 12 Input Parameters.

Angular Quadrature (Sn)	8
Domain Size (cm)	4x4
Number of Material Regions	1
Material Mesh	4x4
Flux Mesh	16x16
Number of Searched Parameters	8
Actual Total Cross Section (cm^{-1})	1.00
Actual Scattering Cross Section (cm^{-1})	0.10, 0.50, 0.90
Homogeneous Initial Guess for Total Cross Sections (cm^{-1})	1.50
Homogeneous Initial Guess for Scattering Cross Sections (cm^{-1})	1.50
Illuminating Source Intensity ($\frac{n}{(cm^2-Sr)}$)	100
Illuminating Sources	all sides

Figs. VI-46 and VI-47 display the reconstructions and errors for the total and scattering cross sections for the problem with 10% scattering. The reconstruction was successful and the maximum error was determined to be on the order of 10^{-5} and 10^{-6} for the total and scattering cross sections, respectively. The reconstruction was completed in one hundred and twenty-six iterations in fifty-three hours.

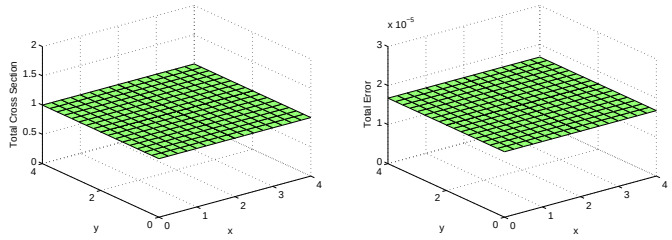

(a) Reconstruction. (b) Error.

Fig. VI-46.: Total Cross Section Reconstruction for the 8-Parameter Homogeneous Domain with 10% Scattering

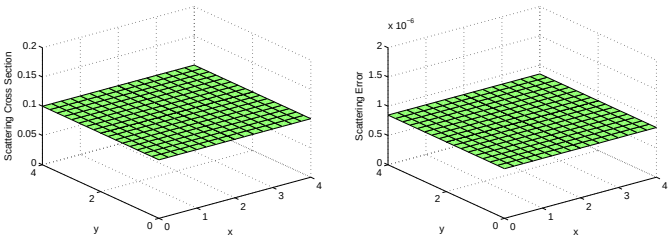

(a) Reconstruction. (b) Error.

Fig. VI-47.: Scattering Cross Section Reconstruction for the 8-Parameter Homogeneous Domain with 10% Scattering

Figs. VI-48 and VI-49 display the reconstructions and errors for the total and scattering cross sections for the problem with 50% scattering. The reconstruction was successful and the maximum error was determined to be on the order of 10^{-5} for the total and scattering cross sections. The reconstruction was completed in one hundred and twenty-six iterations in fifty-two hours.

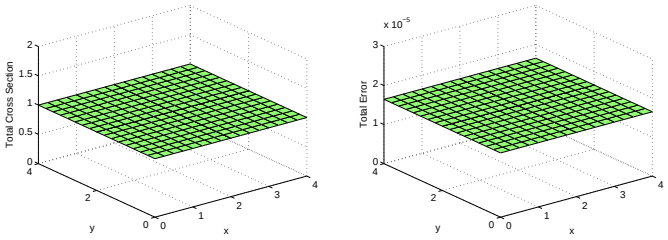

(a) Reconstruction. (b) Error.

Fig. VI-48.: Total Cross Section Reconstruction for the 8-Parameter Homogeneous Domain with 50% Scattering

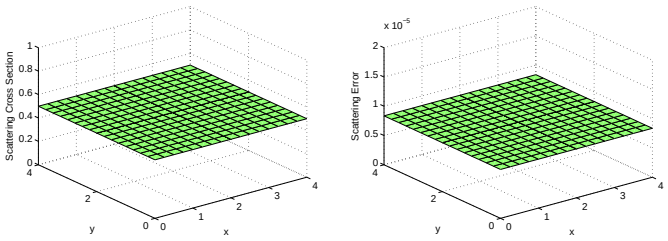

(a) Reconstruction. (b) Error.

Fig. VI-49.: Scattering Cross Section Reconstruction for the 8-Parameter Homogeneous Domain with 50% Scattering

Figs. VI-50 and VI-51 display the reconstructions and errors for the total and scattering cross sections for the problem with 90% scattering. The reconstruction was successful and the maximum error was determined to be on the order of 10^{-5} for both the total and scattering cross sections. The reconstruction was completed in eighty-six iterations in thirty-six hours.

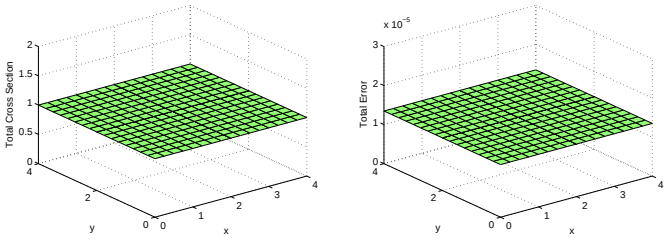

(a) Reconstruction. (b) Error.

Fig. VI-50.: Total Cross Section Reconstruction for the 8-Parameter Homogeneous Domain with 90% Scattering

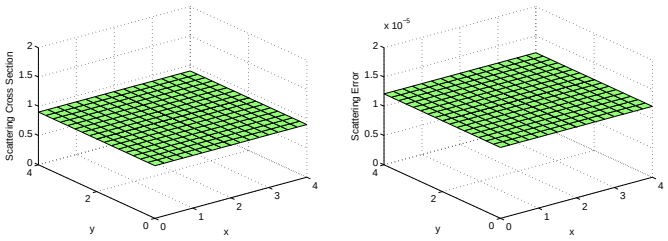

(a) Reconstruction. (b) Error.

Fig. VI-51.: Scattering Cross Section Reconstruction for the 8-Parameter Homogeneous Domain with 90% Scattering

Because of the extremely long solve times of fifty-three, fifty-two and thirty-six hours for this simple homogeneous problem, the transport function was optimized so that computational time could be reduced. This optimization process consisted of calculating only once and storing the large matrices that do not change with each iteration of the the transport operator. Significant performance improvements were noticed after this optimization was conducted and this explains why solution time are significantly reduced in the following problems.

3. Example 13 - Four-Strip Domain with No Signal Noise, Only Noise, and Both Noise and Bias

In example 13, a four strip domain is considered with no signal noise, with only signal noise and with both signal noise and signal bias. This four strip domain is grouped into eight distinct regions where both the total and scattering cross sections are reconstructed. This simulation was conducted with eight experiments each covering half of a side and the scattering percentage was maintained at 90% of the total cross section for all regions in all of the studies conducted in this section. Homoeneous initial parameter distributions of 1.2 and 1.1 cm^{-1} were used as the starting points for the reconstructions of the total and scattering cross sections, respectively. A list of the parameters that define the geometry, discretization scheme, reconstructed cross sections, source positions and applied signal noise and bias for the problem can be seen in Table VI-XV.

Table VI-XV.: Example 13 Input Parameters.

Angular Quadrature (Sn)	8
Domain Sizes (cm)	4x4
Number of Material Regions	4
Material Mesh	4x4
Flux Mesh	8x8
Number of Searched Parameters	16
Actual Total Cross Section of Material 1 (cm^{-1})	0.90
Actual Total Cross Section of Material 2 (cm^{-1})	1.00
Actual Total Cross Section of Material 3 (cm^{-1})	1.10
Actual Total Cross Section of Material 4 (cm^{-1})	0.90
Actual Scattering Ratio for All Materials (c)	0.90
Homogeneous Initial Guess for Total Cross Sections (cm^{-1})	1.20
Homogeneous Initial Guess for Scattering Cross Sections (cm^{-1})	1.10
Illuminating Source Intensity ($\frac{n}{(cm^2-Sr)}$)	100
Illuminating Sources	8-exp, 1/2-side each
Multiplicative Signal Noise (%)	0.01, 0.1, 1.0
Positive Signal Bias (%)	1.00, 5.00
Negative Signal Bias (%)	1.00, 5.00

Figs. VI-52 and VI-53 display the reconstructions and errors for the total and scattering cross sections for the baseline case where no signal noise or bias has been applied to the measured fluxes. The reconstruction was successful and the generated image possessed error on the order of 10^{-5} for both the scattering and total cross

sections. This reconstruction was completed in 54 iterations lasing just under three hours.

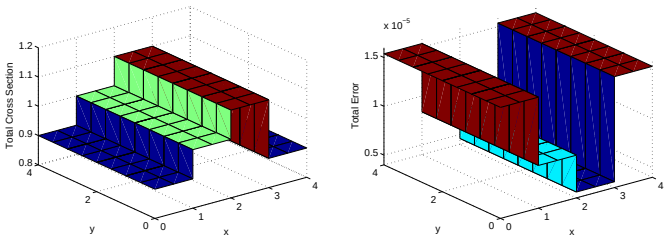

(a) Reconstruction. (b) Error.

Fig. VI-52.: Total Cross Section Reconstruction Results for Four-Strip Domain without Signal Noise

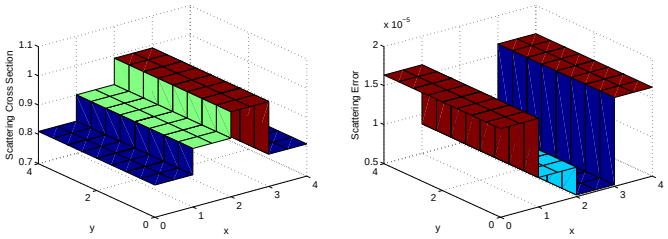

(a) Reconstruction. (b) Error.

Fig. VI-53.: Scattering Cross Section Reconstruction Results for Four-Strip Domain without Signal Noise

Figs. VI-54 and VI-55 display the reconstructions and errors for the total and scattering cross sections for the case where 0.01% signal noise has been applied to the measured fluxes. As expected, more error is introduced into the reconstruction due to this signal noise and the resulting error in the total cross section has quadupled and resulting error in the scattering cross section has tripled as compared with the baseline case. This reconstruction was completed in fifty-one iterations lasting three hours.

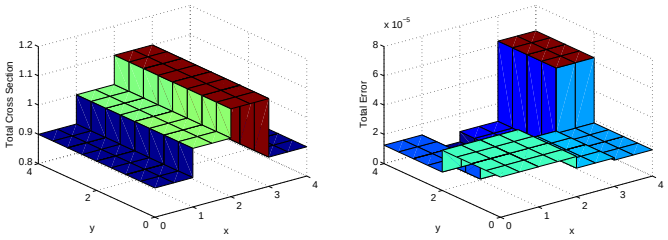

(a) Reconstruction. (b) Error.

Fig. VI-54.: Total Cross Section Reconstruction Results for Four-Strip Domain with 0.01% Signal Noise

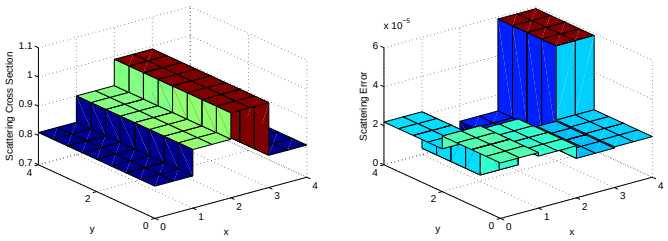

(a) Reconstruction. (b) Error.

Fig. VI-55.: Scattering Cross Section Reconstruction Results for Four-Strip Domain with 0.01% Signal Noise

Figs. VI-56 and VI-57 display the reconstructions and errors for the total and scattering cross sections for the case where 0.10% signal noise has been applied to the measured fluxes. Again, the quality of the reconstructions has further diminished with the addition of more signal noise. The error seen in both the scattering and total cross sections is now on the order of 10^{-4}. This reconstruction was completed in 51 iterations lasting two hours and fourty-five minutes.

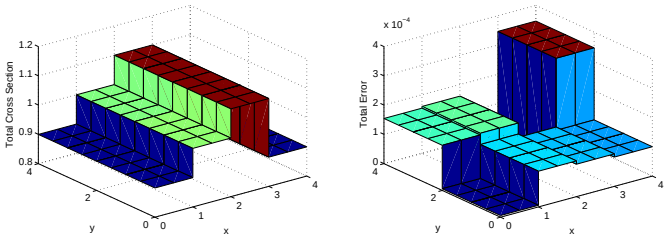

(a) Reconstruction. (b) Error.

Fig. VI-56.: Total Cross Section Reconstruction Results for Four-Strip Domain with 0.10% Signal Noise

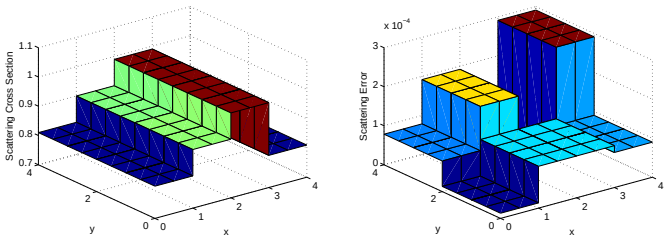

(a) Reconstruction. (b) Error.

Fig. VI-57.: Scattering Cross Section Reconstruction Results for Four-Strip Domain with 0.10% Signal Noise

Figs. VI-58 and VI-59 display the reconstructions and errors for the total and scattering cross sections for the case where 1.00% signal noise has been applied to the measured fluxes. The error in the reconstruction has increased by another order of magnitude due to the addition more signal noise and is now on the order of 10^{-3}. This reconstruction was completed in 49 iterations lasting just under three hours.

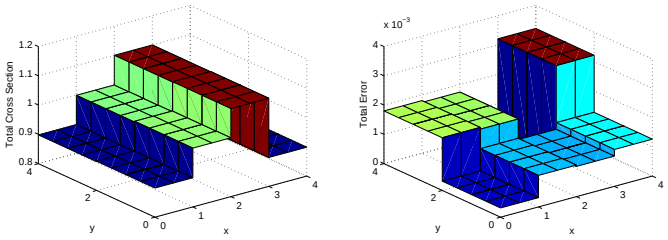

(a) Reconstruction. (b) Error.

Fig. VI-58.: Total Cross Section Reconstruction Results for Four-Strip Domain with 1.00% Signal Noise

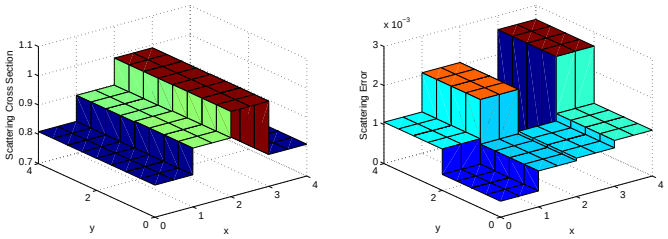

(a) Reconstruction. (b) Error.

Fig. VI-59.: Scattering Cross Section Reconstruction Results for Four-Strip Domain with 1.00% Signal Noise

Figs. VI-60 and VI-61 display the reconstructions and errors for the total and scattering cross sections for the case where 0.10% noise and 1.00% positive signal bias has been applied to the measured fluxes. The error was further increased by the addition of signal bias and is on the order of 10^{-3}. The positive signal bias had the effect of shifting the predicted value of the middle two strips by about 1.00% and decreasing the predicted value of the outer two strips by about 1.00%. The shape of the error produced from this case with positive bias resembles the shape of the error for the baseline case for both the scattering and total cross sections. The major differences between the errors seen in this case and the baseline case are that the

baseline case has no noise so the predicted values of the cross sections are uniform within each region of the domain. Also because of the bias, the error has been scaled and is much larger in magnitude for the case with bias. This reconstruction was completed in 49 iterations lasting just under three hours.

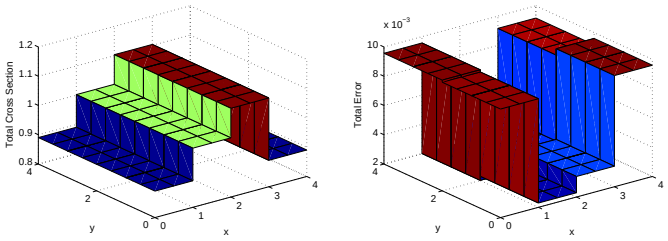

(a) Reconstruction. (b) Error.

Fig. VI-60.: Total Cross Section Reconstruction Results for Four-Strip Domain with 0.10% Signal Noise and 1.00% Positive Signal Bias

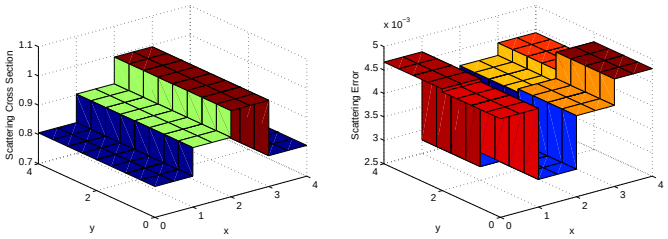

(a) Reconstruction. (b) Error.

Fig. VI-61.: Scattering Cross Section Reconstruction Results for Four-Strip Domain with 0.10% Signal Noise and 1.00% Positive Signal Bias

Figs. VI-62 and VI-63 display the reconstructions and errors for the total and scattering cross sections for the case where 0.10% noise and 5.00% positive signal bias has been applied to the measured fluxes. The error was further increased by the addition of signal bias and is on the order of 10^{-2}. The positive signal bias had the effect of shifting the predicted value of the middle two strips by about 5.00% and

decreasing the predicted value of the outer two strips by about 5.00%. Again, the shape of the error produced from this case is similar to the error seen in the baseline and 1.00% positive bias case where the majority of the reconstruction error occurs in the outer strips of the domain. This reconstruction did not converge in five hundred iterations because the Lagrangian was still changing more 10^{-6} between consecutive iterations. These 500 iterations lasted twenty-seven hours.

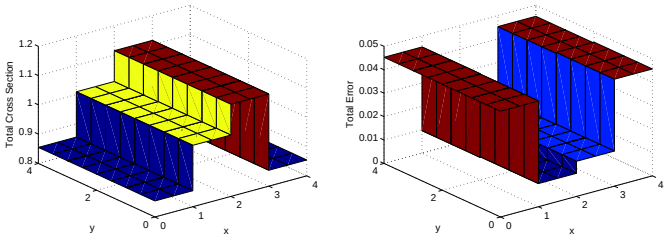

(a) Reconstruction. (b) Error.

Fig. VI-62.: Total Cross Section Reconstruction Results for Four-Strip Domain with 0.10% Signal Noise and 5.00% Positive Signal Bias

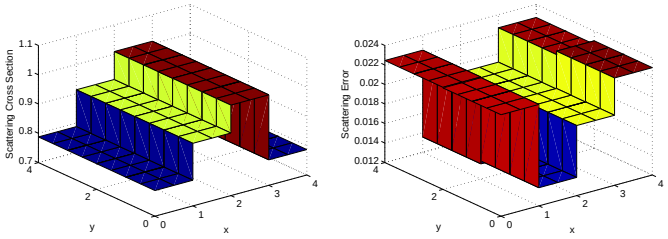

(a) Reconstruction. (b) Error.

Fig. VI-63.: Scattering Cross Section Reconstruction Results for Four-Strip Domain with 0.10% Signal Noise and 5.00% Positive Signal Bias

Figs. VI-64 and VI-65 display the reconstructions and errors for the total and scattering cross sections for the case where 0.10% noise and 1.00% negative signal bias has been applied to the measured fluxes. The error is on the order of 10^{-2} for

the total cross sections and 10^{-3} for the scattering cross sections. The negative signal bias had the opposite effect of the positive bias and decreased the predicted value of the middle two strips by about 5.00% and increased the predicted value of the outer two strips by about 5.00%. The shape of the error produced from this case is similar to the error seen in the baseline case where the majority of the reconstruction error occurs in the outer strips of the domain. This reconstruction was completed in 42 iterations lasting about two hours.

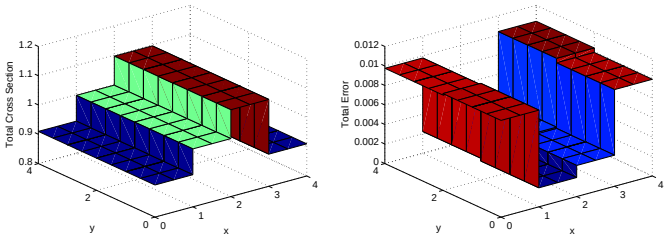

(a) Reconstruction. (b) Error.

Fig. VI-64.: Total Cross Section Reconstruction Results for Four-Strip Domain with 0.10% Signal Noise and 1.00% Negative Signal Bias

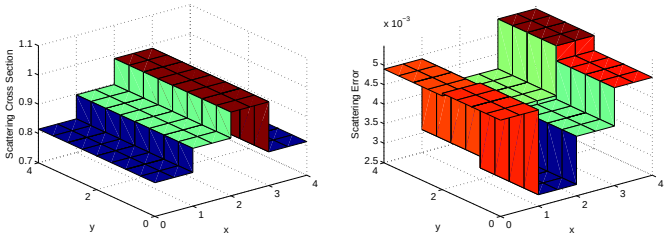

(a) Reconstruction. (b) Error.

Fig. VI-65.: Scattering Cross Section Reconstruction Results for Four-Strip Domain with 0.10% Signal Noise and 1.00% Negative Signal Bias

Figs. VI-66 and VI-67 display the reconstructions and errors for the total and scattering cross sections for the case where 0.10% noise and 5.00% negative signal bias

has been applied to the measured fluxes. The error is on the order of 10^{-2} for the total and scattering cross sections. Again, the reconstruction of the domain underpredicted the values of the middle two strips by about 5.00% and overpredicted the values of the outer two strips by about 5.00%. The shape of the error produced from this case is similar to the error seen in the baseline and the other bias cases where the majority of the reconstruction error occurs in the outer strips of the domain. This reconstruction was completed in 220 iterations lasting about ten hours and fourty-five minutes.

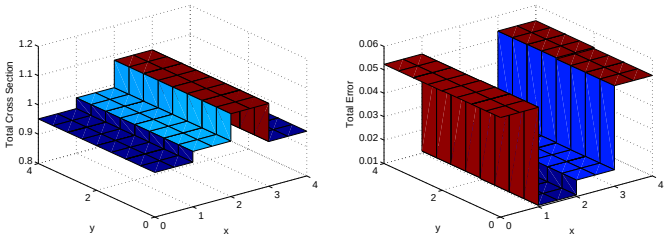

(a) Reconstruction. (b) Error.

Fig. VI-66.: Total Cross Section Reconstruction Results for Four-Strip Domain with 0.10% Signal Noise and 5.00% Negative Signal Bias

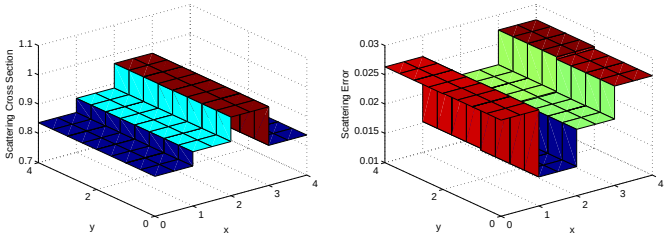

(a) Reconstruction. (b) Error.

Fig. VI-67.: Scattering Cross Section Reconstruction Results for Four-Strip Domain with 0.10% Signal Noise and 5.00% Negative Signal Bias

4. Example 14 - Central Inclusion Optical Thickness Study Reconstructing both Scattering and Total Cross Sections

In example 14, central inclusion problems of increasing size are examined to determine the optical thickness limit for problems with scattering. In these problems, only the total and scattering cross sections of the central inclusion region are reconstructed. This was done because of the increased complexity of the problem due to the addition of scattering. These problems generally required significantly longer computational times than the pure absorber central inclusion problems even after the code optimization had been conducted. The initial values of the misfit and Lagrangian decrease by orders of magnitude as the optical thickness of the problem was increased. This is to be expected because the central region contributes less and less to the solution as is buried deeper and deeper within the domain. To account for this, the convergence tolerance used in the optimization routine was modified to be unique to each problem so that Newton's method would have to reduce the misfit and Lagrangian by at least three orders of magnitude.

Table VI-XVI.: Example 14 Input Parameters.

Angular Quadrature (Sn)	8
Domain Sizes (cm)	8x8, 12x12, 16x16, 20x20
Number of Material Regions	2
Material Mesh	4x4, 6x6, 8x8, 10x10
Flux Mesh	16x16, 24x24, 32x32, 40x40
Number of Searched Parameters	2
Actual Total Cross Section of Surroundings (cm^{-1})	0.90
Actual Total Cross Section of Absorber (cm^{-1})	1.30
Actual Scattering Cross Section of Surroundings (cm^{-1})	0.45
Actual Scattering Cross Section of Absorber (cm^{-1})	0.65
Initial Guess for Inclusion Total Cross Section (cm^{-1})	1.50
Initial Guess for Inclusion Scattering Cross Section (cm^{-1})	0.85
Illuminating Source Intensity ($\frac{n}{(cm^2-Sr)}$)	100
Illuminating Sources	8-exp, 1/2-side each

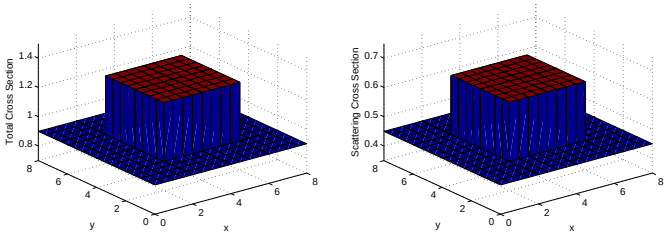

(a) Total Reconstruction. (b) Scattering Reconstruction.

Fig. VI-68.: 4x4 Central Absorber Domain Reconstructing both Scattering and Total Cross Sections

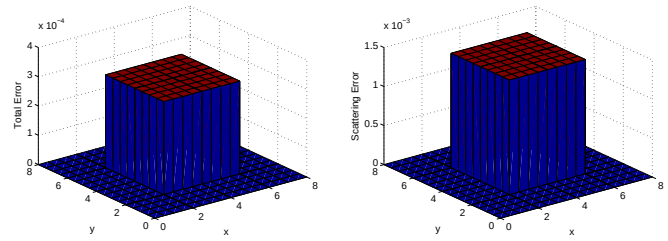

(a) Total Error. (b) Scattering Error.

Fig. VI-69.: 4x4 Central Absorber Domain Reconstructing both Scattering and Total Cross Sections

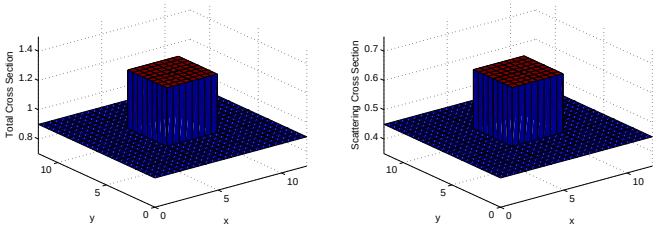

(a) Total Reconstruction. (b) Scattering Reconstruction.

Fig. VI-70.: 6x6 Central Absorber Domain Reconstructing both Scattering and Total Cross Sections

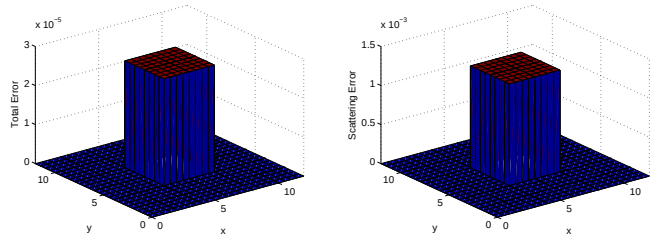

(a) Total Error. (b) Scattering Error.

Fig. VI-71.: 6x6 Central Absorber Domain Reconstructing both Scattering and Total Cross Sections

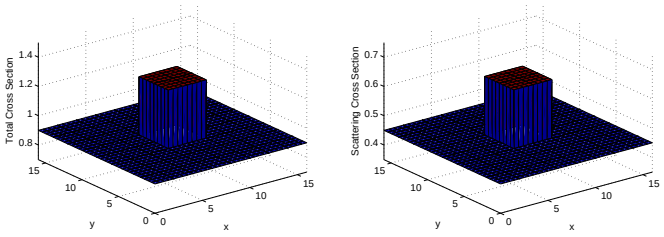

(a) Total Reconstruction. (b) Scattering Reconstruction.

Fig. VI-72.: 8x8 Central Absorber Domain Reconstructing both Scattering and Total Cross Sections

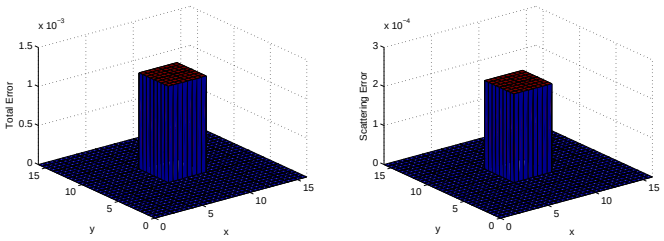

(a) Total Error. (b) Scattering Error.

Fig. VI-73.: 8x8 Central Absorber Domain Reconstructing both Scattering and Total Cross Sections

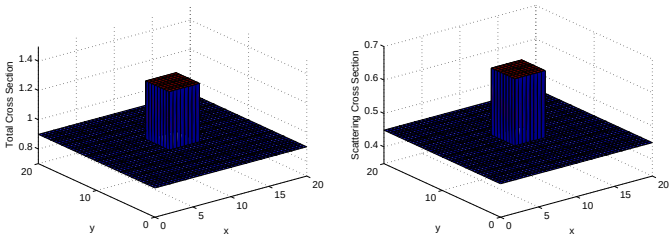

(a) Total Reconstruction. (b) Scattering Reconstruction.

Fig. VI-74.: 10x10 Central Absorber Domain Reconstructing both Scattering and Total Cross Sections

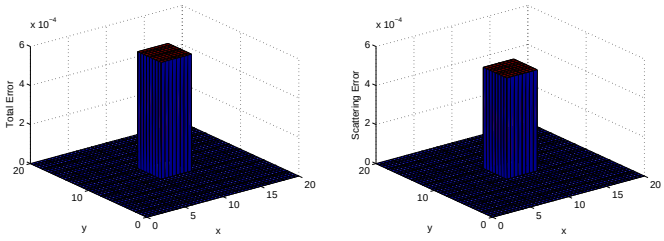

(a) Total Error. (b) Scattering Error.

Fig. VI-75.: 10x10 Central Absorber Domain Reconstructing both Scattering and Total Cross Sections

5. Example 15 - Homogeneous Domain Initial Guess Study Reconstructing both Scattering and Total Cross Sections

In example 15, the sensitivity of Newton's method when reconstructing both the total and scattering cross sections is test on a homogeneous domain. Three different initial guesses are proposed as the starting point for the optimization process starting from the values above and below the actual parameters. The same heuristic procedure was implemented as in the pure absorber initial guess problem where if the optimization process began to stagnate and the line search was only permitting Newton's method

to take very small steps, the step size was overwritten and a larger step was taken. This process was almost never required when the actual parameters were approached from above starting from a higher initial guess. This process was frequently required when the actual parameters were approached from below starting from a lower initial guess. A description of the input parameters for the problem for all of the studies conducted in this example as well as the initial parameter distributions used to start the optimization process are described in table VI-XVII. Again, since the reconstructed domain was homogeneous, the initial guess was generated with random numbers to make it heterogeneous and more challenging for Newton's method.

Table VI-XVII.: Example 15 Input Parameters.

Angular Quadrature (Sn)	8
Domain Sizes (cm)	4x4
Number of Material Regions	1
Material Mesh	4x4
Flux Mesh	16x16
Number of Searched Parameters	4
Actual Total Cross Section (cm^{-1})	1.0
Actual Scattering Cross Section (cm^{-1})	0.5
Initial Guesses Approaching from Above (%)	1000 ± 200, 5000 ± 1000, 10000 ± 2500
Initial Guesses Approaching from Below (%)	90 ± 2, 80 ± 5, 50 ± 10
Illuminating Source Intensity ($\frac{n}{(cm^2-Sr)}$)	100
Illuminating Sources	8-exp, 1/2-side each

Figs. VI-76, VI-77, VI-78, VI-79, VI-80 and VI-81 display the initial guess,

reconstruction and error results for the scattering and total cross sections of the homogeneous domain starting from an initial guess that is lower than the actual scattering and total cross sections. Figs. VI-76 and VI-77 represent the optimization results when an initial guess of $90\% \pm 2\%$ of the true scattering and total cross sections was used. Figs. VI-78 and VI-79 represent the optimization results when an initial guess of $80\% \pm 5\%$ of the true scattering and total cross sections was used. Figs. VI-80 and VI-81 represent the optimization results when an initial guess of $50\% \pm 10\%$ of the true scattering and total cross sections was used. Newton's method was able to reconstruct the homogeneous domain from the $90\% \pm 2\%$ and $80\% \pm 5\%$ initial parameters distributions, but it was unable to reconstruct the domain from the $50\% \pm 10\%$ initial guess. It both of the successful reconstructions, the step length was required to be reset many times before the solution was achieved. This again reinforced the trend that Newton's method found it easier to appoach the solution from a higher initial guess than a lower one. In addition, the complexity of the scattering problem was emphasized as the proposed initial guesses had to be much closer to the true parameter distribution for the problem with scattering as compared with the pure absorber problems seen in example 7.

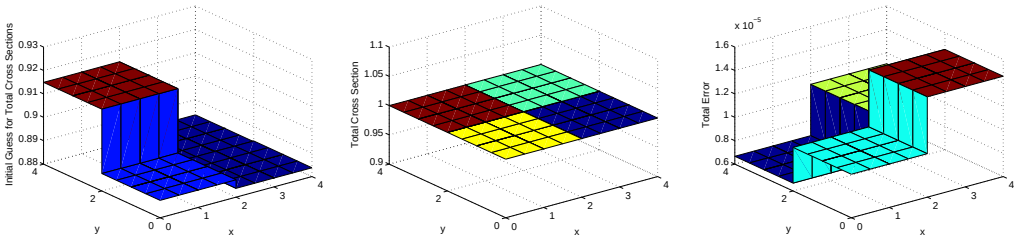

(a) Initial Guess. (b) Reconstruction. (c) Error.

Fig. VI-76.: Initial Guess, Reconstruction and Error Results for Total Cross Section with $90 \pm 2\%$ Initial Guess

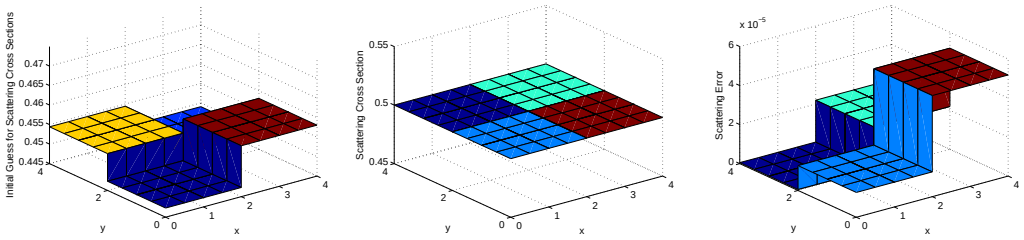

(a) Initial Guess. (b) Reconstruction. (c) Error.

Fig. VI-77.: Initial Guess, Reconstruction and Error Results for Scattering Cross Section with $90 \pm 2\%$ Initial Guess

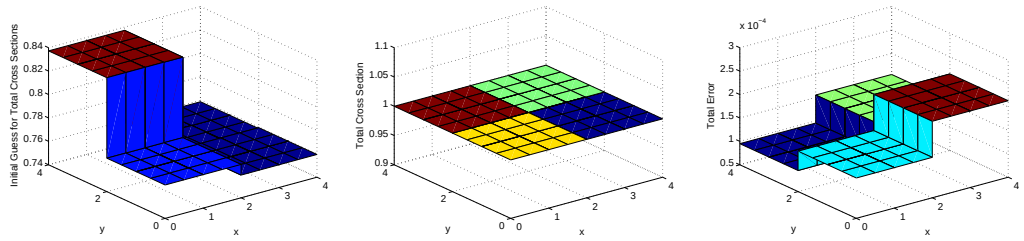

(a) Initial Guess. (b) Reconstruction. (c) Error.

Fig. VI-78.: Initial Guess, Reconstruction and Error Results for Total Cross Section with $80 \pm 5\%$ Initial Guess

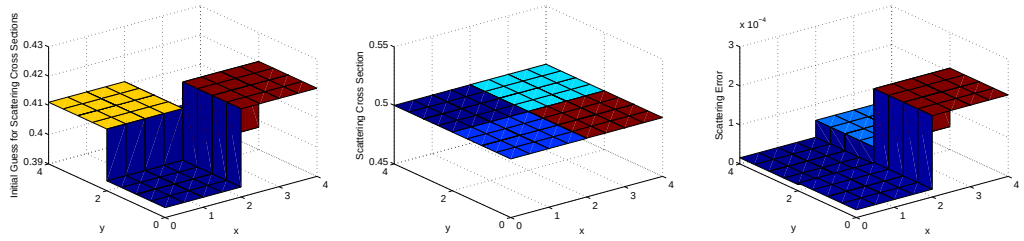

(a) Initial Guess. (b) Reconstruction. (c) Error.

Fig. VI-79.: Initial Guess, Reconstruction and Error Results for Scattering Cross Section with $80 \pm 5\%$ Initial Guess

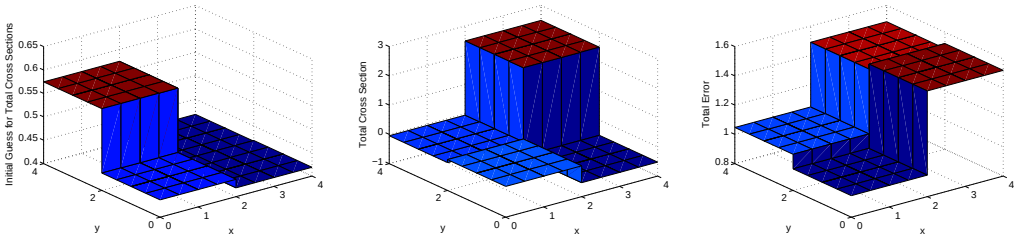

(a) Initial Guess. (b) Reconstruction. (c) Error.

Fig. VI-80.: Initial Guess, Reconstruction and Error Results for Total Cross Section with $50 \pm 10\%$ Initial Guess

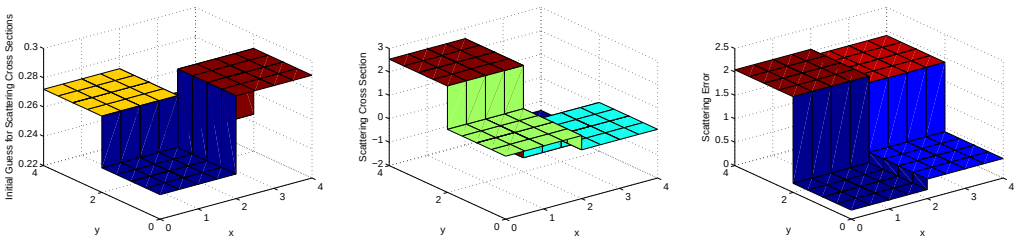

(a) Initial Guess. (b) Reconstruction. (c) Error.

Fig. VI-81.: Initial Guess, Reconstruction and Error Results for Scattering Cross Section with $50 \pm 10\%$ Initial Guess

Figs. VI-82, VI-83, VI-84, VI-85, VI-86 and VI-87 display the initial guess, reconstruction and error results for the scattering and total cross sections of the homogeneous domain starting from an initial guess that is higher than the actual scattering and total cross sections. Figs. VI-82 and VI-83 represent the optimization results when an initial guess of $1000\% \pm 200\%$ of the true scattering and total cross sections was used. Figs. VI-84 and VI-85 represent the optimization results when an initial guess of $5000\% \pm 1000\%$ of the true scattering and total cross sections was used. Figs. VI-86 and VI-87 represent the optimization results when an initial guess of $10000\% \pm 2500\%$ of the true scattering and total cross sections was used. Newton's

method was able to reconstruct the homogeneous domain from the $1000\% \pm 200\%$ and $5000\% \pm 1000\%$ initial parameters distributions, but it was unable to reconstruct the domain from the $10000\% \pm 2500\%$ initial guess. In all of these cases where the initial guess was greater than the true values of the parameters, the lines search method never stagnated and the step length was never reset. This again reinforced the trend that Newton's method found it easier to appoach the solution from a higher initial guess than a lower one. The complexity of the scattering problem was emphasized as $10000\% \pm 2500\%$ initial guess was unsuccessful when both the scattering and total cross sections were reconstructed as compared with the pure absorber problem seen in example 7.

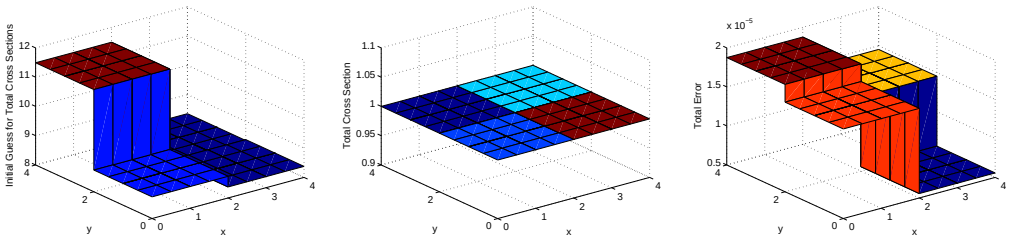

(a) Initial Guess. (b) Reconstruction. (c) Error.

Fig. VI-82.: Initial Guess, Reconstruction and Error Results for Total Cross Section with $1000 \pm 200\%$ Initial Guess

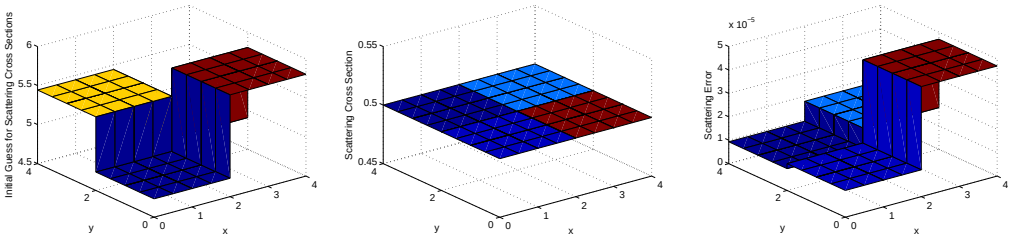

(a) Initial Guess. (b) Reconstruction. (c) Error.

Fig. VI-83.: Initial Guess, Reconstruction and Error Results for Scattering Cross Section with $1000 \pm 200\%$ Initial Guess

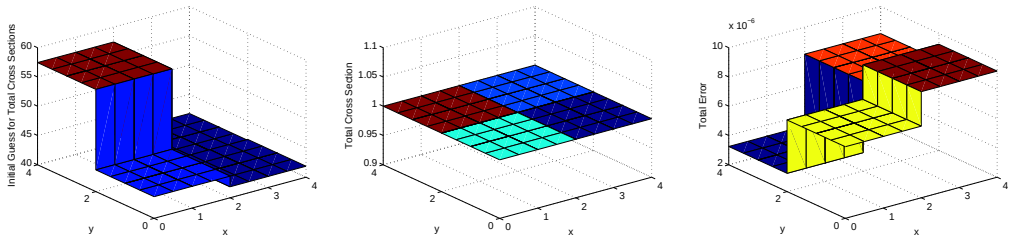

(a) Initial Guess. (b) Reconstruction. (c) Error.

Fig. VI-84.: Initial Guess, Reconstruction and Error Results for Total Cross Section with $5000 \pm 1000\%$ Initial Guess

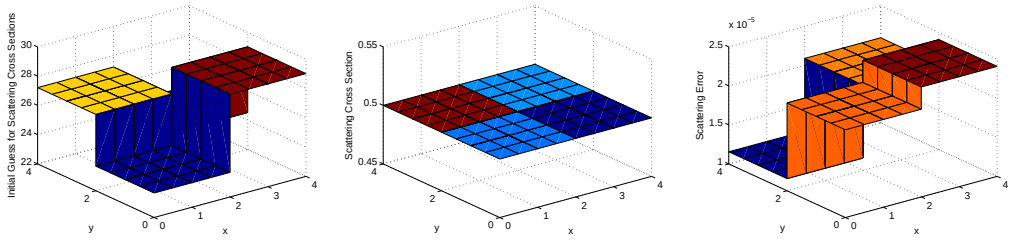

(a) Initial Guess. (b) Reconstruction. (c) Error.

Fig. VI-85.: Initial Guess, Reconstruction and Error Results for Scattering Cross Section with $5000 \pm 1000\%$ Initial Guess

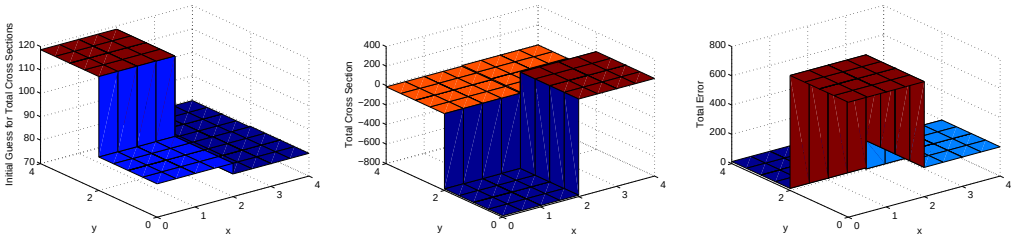

(a) Initial Guess. (b) Reconstruction. (c) Error.

Fig. VI-86.: Initial Guess, Reconstruction and Error Results for Total Cross Section with $10000 \pm 2500\%$ Initial Guess

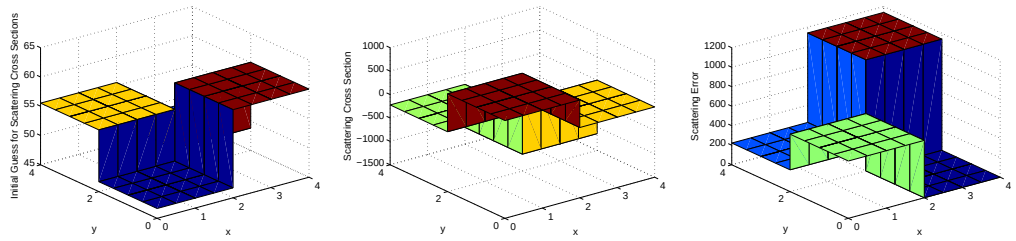

(a) Initial Guess. (b) Reconstruction. (c) Error.

Fig. VI-87.: Initial Guess, Reconstruction and Error Results for Scattering Cross Section with $10000 \pm 2500\%$ Initial Guess

6. Example 16 - Four Region Domain with Illuminating Sources on 1, 2, 3 or 4 Sides Reconstructing both Scattering and Total Cross Sections

In example 16, the effects of imposing sources on different numbers of sides in a single experiment is examined on a four region domain with scattering. The scattering cross sections for the domain were maintained at 50% of the total cross section for all of the studies conducted in this section. The same material region layout and side numbering scheme was used in this example as can be seen in Fig. VI-10 of example 4. A list of the parameters that define the geometry, discretization scheme, reconstructed cross

sections and source positions for the problem can be seen in Table VI-XVIII.

Table VI-XVIII.: Example 16 Input Parameters.

Angular Quadrature (Sn)	8
Domain Size (cm)	8x8
Number of Material Regions	4
Material Mesh	4x4
Flux Mesh	16x16
Number of Searched Parameters	8
Actual Total Cross Section of Material 1 (cm^{-1})	0.70
Actual Total Cross Section of Material 2 (cm^{-1})	0.90
Actual Total Cross Section of Material 3 (cm^{-1})	1.10
Actual Total Cross Section of Material 4 (cm^{-1})	1.30
Actual Scattering Ratio for All Materials (c)	0.50
Homogeneous Initial Guess for Cross Section (cm^{-1})	1.5
Illuminating Source Intensity ($\frac{n}{(cm^2-Sr)}$)	100
Illuminating Sources	1, 2, 3, 4 sides

Figs. VI-88 and VI-89 display the results of the reconstruction as sources are applied to only one side of the model. In this case, the reconstruction is unsuccessful just as it was not in the pure absorber problem in example 4. The single experiment with a single beam does not proved sufficient information about the domain to generate an image. Most likely the beam is sufficiently attenuated and scattered with in the domain that measurable fluxes do not provide a good representation of the material properties of the domain and the reconstruction fails. This failure is evidenced by the large errors in the scattering and total cross sections which are on the order of

10^{-1}. The Newton iterations were terminated after five hundred iterations and forty hours.

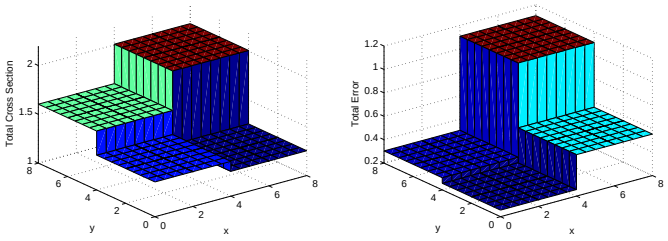

(a) Reconstruction. (b) Error.

Fig. VI-88.: Total Reconstruction and Error for Four-Region Domain with Sources on 1 Side

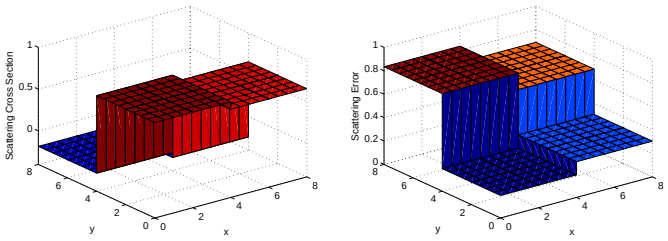

(a) Reconstruction. (b) Error.

Fig. VI-89.: Scattering Reconstruction and Error for Four-Region Domain with Sources on 1 Side

Figs. VI-90, VI-91, VI-92, VI-93, VI-94 and VI-95 display the reconstruction and error results for the other three models with sources on two, three or fours sides of the model. All of these cases were successful and the the general trend of a reduction in the reconstruction error and an improvement in image quality as more sources are used can be seen in these results. The successful reconstructions were conducted in 124, 260 and 240 iteration for the simulations with beams on two, three and four sides, respectively. These reconstructions required ten and half, twenty-six

and twenty-three hours for the studies with illuminating sources on two, three and four sides to complete, respectively.

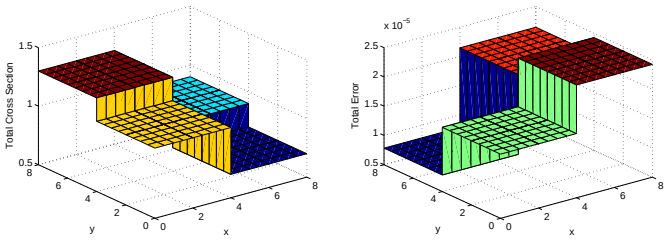

(a) Reconstruction. (b) Error.

Fig. VI-90.: Total Reconstruction and Error for Four-Region Domain with Sources on 2 Sides

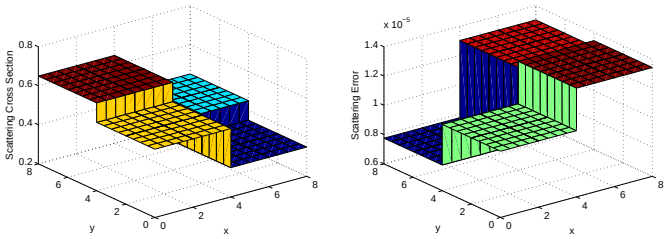

(a) Reconstruction. (b) Error.

Fig. VI-91.: Scattering Reconstruction and Error for Four-Region Domain with Sources on 2 Sides

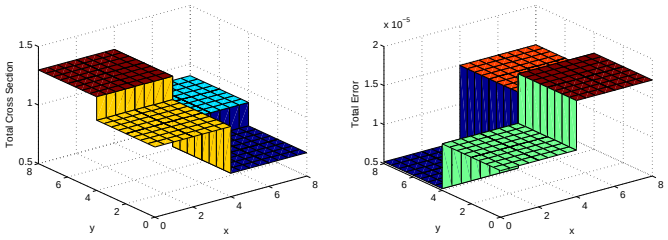

(a) Reconstruction. (b) Error.

Fig. VI-92.: Total Reconstruction and Error for Four-Region Domain with Sources on 3 Sides

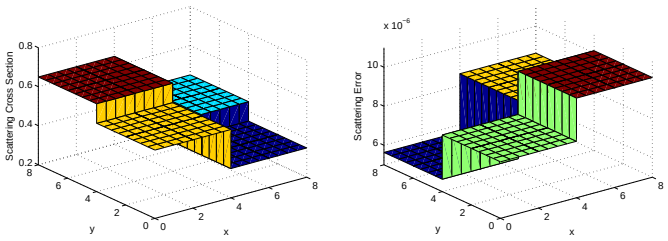

(a) Reconstruction. (b) Error.

Fig. VI-93.: Scattering Reconstruction and Error for Four-Region Domain with Sources on 3 Sides

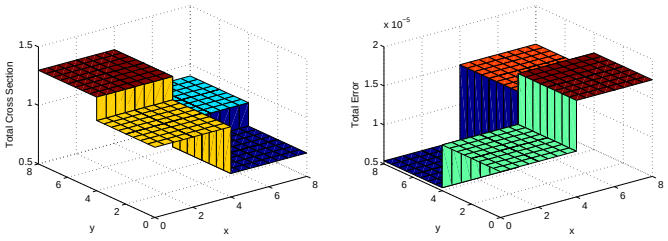

(a) Reconstruction. (b) Error.

Fig. VI-94.: Total Reconstruction and Error for Four-Region Domain with Sources on 4 Sides

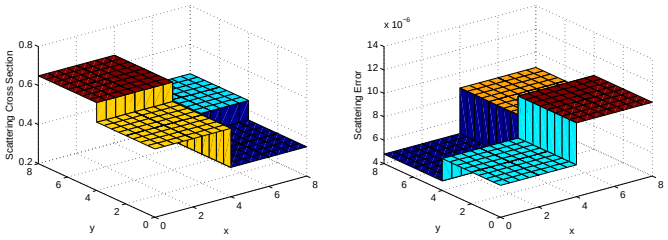

(a) Reconstruction. (b) Error.

Fig. VI-95.: Scattering Reconstruction and Error for Four-Region Domain with Sources on 4 Sides

7. Example 17 - Four Region Domain Reconstructing both Scattering and Total Cross Sections Using Measurements from 1, 2, 3 and 4 Sides

In example 17 the effects of using the measurements from different combinations of sides of the model in the reconstruction process are explored. All of the models seen in this example are simulated with eight experiments each covering half of a side and both the total and scattering cross sections are reconstructed simultaneously. All of the scattering cross sections in the models simulated in example 17 are maintained at 90% of the total cross section values. The same material region layout and side numbering scheme was used in this example as can be seen in Fig. VI-10 of example 4. Homogeneous initial guesses of 1.5 cm^{-1} and 1.3 cm^{-1} were used as starting points for Newton's method for the total and scattering cross sections. A list of the parameters that define the geometry, discretization scheme, reconstructed cross sections and source positions for the problem can be seen in Table VI-XIX.

Table VI-XIX.: Example 17 Input Parameters.

Angular Quadrature (Sn)	8
Domain Sizes (cm)	8x8
Number of Material Regions	4
Material Mesh	4x4
Flux Mesh	16x16
Number of Searched Parameters	4
Actual Total Cross Section of Material 1 (cm^{-1})	0.70
Actual Total Cross Section of Material 2 (cm^{-1})	0.90
Actual Total Cross Section of Material 3 (cm^{-1})	1.10
Actual Total Cross Section of Material 4 (cm^{-1})	1.30
Actual Scattering Ratio for All Materials (c)	0.90
Homogeneous Initial Guess for Total Cross Sections (cm^{-1})	1.5
Homogeneous Initial Guess for Scattering Cross Sections (cm^{-1})	1.3
Illuminating Source Intensity ($\frac{n}{(cm^2-Sr)}$)	100
Illuminating Sources	8-exp, 1/2-side each
Measurements	1, 2, 3 or 4 Sides

Figs. VI-96 and VI-97 display the reconstruction and error results as the total and scattering cross sections of the domain are reconstructed only with the measurements from one side. In this case, Newton's method was unable to reconstruct the cross sections of the domain in the provided two hundred iterations. This was most likely due to the fact that insufficient information was collected from only measuring on one side of the model to correctly identify the material property distribution

of the domain. This failed reconstruction is evident by the large errors seen in the reconstruction that are on the order of 10^0. The two hundred iterations that were conducted for this problem lasted for about nine hours.

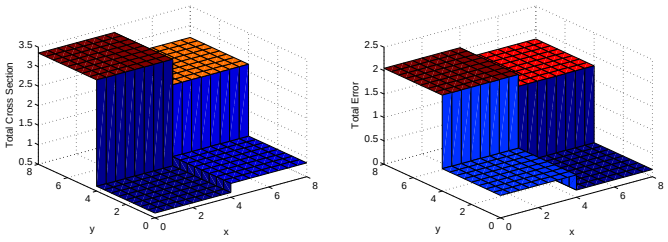

(a) Reconstruction. (b) Error.

Fig. VI-96.: Total Reconstruction and Error Results for the Four Region Domain with Measurements on 1 Side

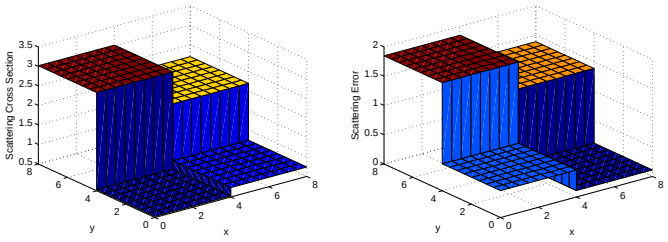

(a) Reconstruction. (b) Error.

Fig. VI-97.: Scattering Reconstruction and Error Results for the Four Region Domain with Measurements on 1 Side

Figs. VI-98, VI-99, VI-100, VI-101, VI-102 and VI-103 are the reconstruction and error results for the scattering and total cross sections for the domain where measurements gathered from two, three or four sides of the model were used in the reconstruction. All of these simulations were successful. The trend of improved image quality and reduction in reconstruction error as more measurements are use to generate the image is again noted in this example. Forty-four, forty-nine and

forty-nine iterations were required for the reconstruction for the models run with measurement collected from two, three and four sides, respectively. These simulations lasted twenty-four, twenty-nine and twenty-four hours to run, respectively.

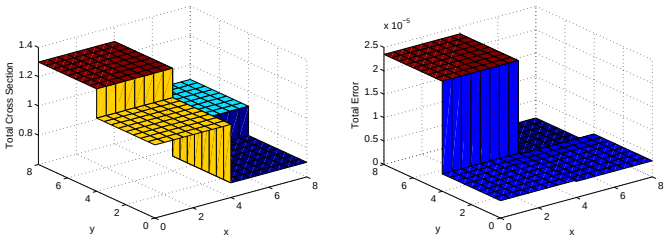

(a) Reconstruction. (b) Error.

Fig. VI-98.: Total Reconstruction and Error Results for the Four Region Domain with Measurements on 2 Sides

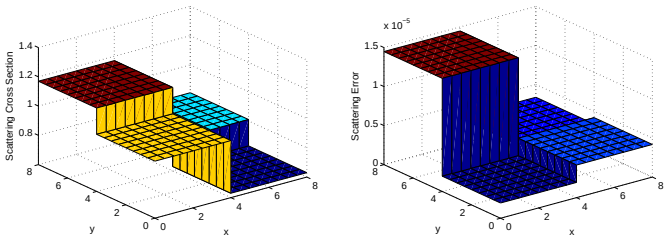

(a) Reconstruction. (b) Error.

Fig. VI-99.: Scattering Reconstruction and Error Results for the Four Region Domain with Measurements on 2 Sides

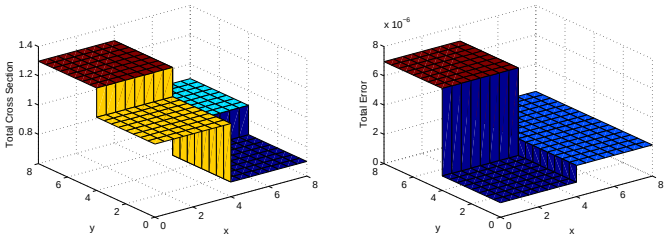

(a) Reconstruction. (b) Error.

Fig. VI-100.: Total Reconstruction and Error Results for the Four Region Domain with Measurements on 3 Sides

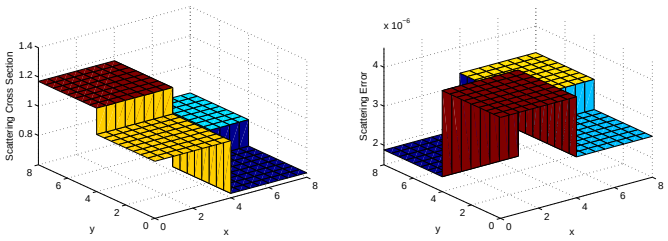

(a) Reconstruction. (b) Error.

Fig. VI-101.: Scattering Reconstruction and Error Results for the Four Region Domain with Measurements on 3 Sides

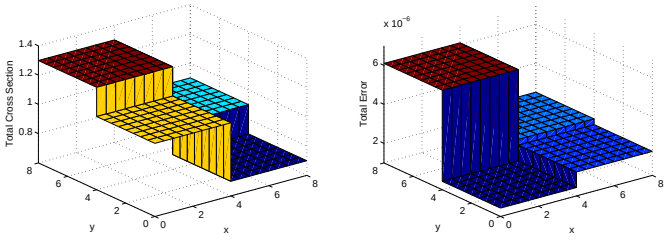

(a) Reconstruction. (b) Error.

Fig. VI-102.: Total Reconstruction and Error Results for the Four Region Domain with Measurements on 4 Sides

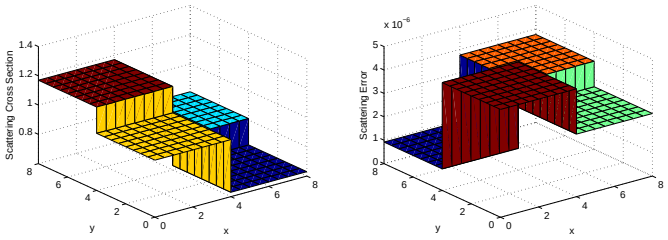

(a) Reconstruction. (b) Error.

Fig. VI-103.: Scattering Reconstruction and Error Results for the Four Region Domain with Measurements on 4 Sides

8. Summary of Findings from Scattering Problems

In this section the challenges of introducing scattering into many problems was examined. It was noticed the scattering process increases the complexity of the inverse transport problem because the measurable radiation is now clouded with uncertainty about the origin of the particle. In the pure absorber problems, the image of the domain is generated based simply on the difference between the original intensity of the incident beams and the measured radiation a the measurement point. In other words, the amount of radiation that is removed from the beam or absorbed by the domain is used to create the image. However, when scattering is introduced, now radiation can be measured at the detectors after is had interacted within the domain. This complicated the reconstruction process because now the origin of the measured radiation is uncertain and can only be categorized by a probability. This again is more complicated than the pure absorber problems where radiation only traverses the domain in straight lines. Only isotropic scattering was studied in this Thesis as well, so the inverse transport problem is yet still more complicated in actuality.

In addition to the added difficulty noticed in all of the scattering problems, some other unique findings were uncovered in each of the specific scattering problems. In

example 11, the misfit surface of a two-parameter problem was plotted as to understand its shape as the scattering and total cross sections were varied. This evidenced the additional difficulty in determining the scattering cross section and that the surface was often rather flat unless the proposed values was very near the actual solution. This meant that the gradient of the misfit provided little information about the location of the minimum and the wall of the misfit valley were also noticed to be convex. Both of these observations again reinforce the complexity of the inverse transport problem. In example 12, a simple homogeneous domain was examined to get a feel for the capability of Newton's method to reconstruct both the scattering and total cross sections. The method had little trouble reconstructing these parameters, but the computational time required for problems with scattering was noted and algorithm was optimized for better performance. In example 13, the four strip domain was revisited with signal noise and bias. The same trends were noticed in the scattering reconstruction as in the pure absorber problems. Increasing the noise in the measured fluxes caused greater error in the reconstructed image. Signal bias had the effect of shifting the cross section of the domain in either the positive or negative direction due to the uniform increase or decrease seen in the measured fluxes.

In example 15, the initial guess studies were revisited and the complexity of the scattering problems became apparent as many of the initial guess that were successful for the pure absorber problems were not for the scattering cases. The same challenges were noticed as Newton's method approached the solution from a lower initial guess and higher initial guess proved to be more reliable. In example 16, the problem where sources were applied to different combinations of sides of the domain was studied for a scattering problem. Again, when the beam was imposed on only one side of the model, insufficient information could be collected to fully characterize the material properties of the domain. The reconstruction was successful when beams were imposed on

more sides of the model and as more beams were imposed, image quality improved. Finally, in example 17 a four region domain with scattering was reconstructed with measurements from various numbers of sides of the domain. The added complexity of scattering was noted as the reconstruction was unsuccessful when measurements were collected from only one side of the model, because this case was successful for the pure absorber case. The trend of improved image quality as measurements were recorded from more sides of the model was again evident.

CHAPTER VII

CONCLUSIONS AND OUTLOOK

Using transport theory and Newton's method to create images of various domains has potential to be a useful algorithm to analyze cargo container scans. First, this algorithm generally requires less iterations and computational time than any derivative free technique. Second, this method is also easy to implement as long as the first and second derivatives of the Lagrangian function can be computed. Third, it is also flexible enough to accommodate differing illuminating sources, numbers of experiments, initial guesses and measurement locations. Fourth, this technique showed a successful ability to reconstruct domains where signal noise and bias was applied to the angular fluxes. And last, the inverse transport method proved capable to reconstruct a wide range of problems ranging from pure absorbers to highly scattering mediums.

Many limitations of applying Newton's method to the transport equation were also discovered. First, a maximum of ten mean free paths thick for pure absorbers and two mean free paths for scattering problems were determined to be the maximum optical thicknesses where the measurable signal from the illuminating sources is still strong enough to permit reconstruction. Second, the dependence of the success of the reconstruction and the required computational time was determined to be highly dependent on the initial guess for the parameters. And third, this method allows for Newton's method to propose negative cross section values and scattering cross sections that are larger there corresponding total cross section. An additional backtracking technique was employed as an attempt to prevent this problem, but these scenarios are have no physical meaning and further constraints could be applied to prevent this.

Looking forward, there are a few ways to improve how Newton's method is

applied to the transport equation. First, a more robust line search than the Armijo or Wolfe backtrack technique could be employed to ensure that Newton's method does not overshoot the true solution. Second, the Lagrangian could be modified to include further constraints including an upper and lower bound on the cross sections and a check that ensures that the total cross section is always greater than or equal to the scattering cross section. Third, a method for treating the uncollided flux could be considered in unison with this method to better characterize the uncollided radiation. Fourth, a preconditioner could be implemented to provide Newton's method with an improved initial guess for the distribution of the cross sections within the domain. Fifth, this method could be made compatible with adaptive meshing strategies so that finer meshes could be generated in areas of interest and coarser meshes could be used for less interesting areas. Sixth, anisotropic scattering could be added to the forward solver to expand the range of problems that can be considered with the method. Seventh, the method could be extended to three dimensions to tackle more realistic problems. And last, this method could be parallelized so that the problem could be solved more efficiently on multiple processors.

REFERENCES

[1] J. Baker McNeill, "100 percent cargo container scanning: A global disaster," Research report, Kathryn and Shelby Cullom Davis Institute for International Studies, 2008.

[2] Jorina Fontelera, "Homeland Security to Miss Cargo Scanning Deadline," ThomasNet News, March 4, 2009.

[3] Dennis Slaughter, Mark Accatino, Adam Bernstein,, James Candy, Arden Dougan, James Hall, Alex Loshak, Doug Manatt, Alan Meyer, Bert Pohl, Stanley Prussin, Rosemary Walling, and David Weirup. Detection of Special Nuclear Material in Cargo Containers Using Neutron Interrogation. Rep. no. UCRL-ID-155315. Livermore: University of California, Lawrence Livermore National Laboratory, 2003. Print.

[4] United States. Government Accountability Office. Natural Resources and Environment. *Combating Nuclear Smuggling: DHS's Cost-benefit Analysis to Support the Purchase of New Radiation Detection Portal Monitors Was Not Based on Available Performance Data and Did Not Fully Evaluate All the Monitors' Costs and Benefits.* By Gene Aloise. Washington, DC: Government Accountability Office, 2006. Print.

[5] J. A. Nelder and R. Mead, "A simplex method for function minimization," *The Computer Journal*, vol. 7, pp. 308–313, 1965.

[6] Jorge Nocedal and Stephen J. Wright, *Numerical Optimization* New York: Springer, 2006, Print.

[7] Vittorio Scipolo, "Scattered neutron tomography based on a neutron transport problem," Master's thesis, Texas A&M University, College Station, Texas, August 2004.

[8] Matthew Ryan Sternat, "Application of a constrained optimization technique to the imaging of heterogeneous objects using diffusion theory," Master's thesis, Texas A&M University, College Station, Texas, December 2009.

[9] Zeyun Wu, "Advances in inverse transport methods and applications to neutron tomography," Ph.D. dissertation, Texas A&M University, College Station, Texas, December 2010.

[10] Alexander D. Klose, and Andreas H. Hielscher. "Iterative Reconstruction Scheme for Optical Tomography Based on the Equation of Radiative Transfer." Medical Physics 26.8 (1999): 1698-707. Print.

[11] Alexander D. Klose, and Andreas H. Hielscher. "Quasi-Newton Methods in Optical Tomographic Image Reconstruction." Inverse Problems 19.2 (2003): 387-409. Print.

[12] A. Klose, V. Ntziachristos, and A. Hielscher. "The Inverse Source Problem Based on the Radiative Transfer Equation in Optical Molecular Imaging." Journal of Computational Physics 202.1 (2005): 323-45. Print.

[13] Gassan S. Abdoulaev, Kui Ren, and Andreas H. Hielscher, "'Optical Tomography as a PDE-constrained Optimization Problem,"' emphInverse Problems, vol. 21.5 (2005): pp. 1507-530. Print.

[14] Gassan S. Abdoulaev, and Andreas H. Hielscher. "Three-dimensional Optical Tomography with the Equation of Radiative Transfer." Journal of Electronic

Imaging 12.4 (2003): 594-601. Print.

[15] Andreas H. Hielscher, and Sebastian Bartel. "Use of Penalty Terms in Gradient-based Iterative Reconstruction Schemes for Optical Tomography." Journal of Biomedical Optics 6.2 (2001): 183-92. Print.

[16] Wolfgang Bangerth. "A Framework for the Adaptive Finite Element Solution of Large-Scale Inverse Problems." SIAM Journal on Scientific Computing 30.6 (2008): 2965-989. Print.

[17] Wolfgang Bangerth, and Amit Joshi. "Adaptive Finite Element Methods for the Solution of Inverse Problems in Optical Tomography." Inverse Problems 24.3 (2008): 034011. Print.

[18] Ranadhir Roy, and Eva M. Sevick-Muraca. "Active Constrained Truncated Newton Method for Simple-bound Optical Tomography." Journal of the Optical Society of America A 17.9 (2000): 1627-641. Print.

[19] Esam M A. Hussein, and John T C. Bowles. "Expanding the Domain of Contraction Mapping in the Inverse Problem of Imaging with Incoherently Scattered Radiation." Inverse Problems vol. 23.3 (2007): pp. 1289-309. Print.

[20] E. Haber, and U. M. Ascher. "Preconditioned All-at-once Methods for Large, Sparse Parameter Estimation Problems." Inverse Problems 17 (2001): 1847-864. Print.

[21] Weston M. Stacey, *Nuclear Reactor Physics*, New York: John Wiley & Sons, 2001, Print.

APPENDIX A

TITLE OF APPENDIX

VITA

Nathaniel Raymond Fredette was born in 1986 to Mark A. Fredette and Denise M. Fredette in Houston, TX. He graduated from Strake Jesuit College Preparatory in 2004, received his Bachelor of Science in mechanical engineering from Marquette University in 2009 and his Master of Science in nuclear engineering from Texas A&M University in 2011. He is a member of the American Nuclear Society and the National Scholars Honor Society. His primary interests are nuclear reactor design and simulation specifically related to naval applications. He plans to start a career with Knolls Atomic Power Laboratory designing power reactors.

Department of Nuclear Engineering
Texas A&M University
3133 TAMU
College Station, TX 77843-3133
nate.fredette@gmail.com